DEPARTMENT OF
MATERIALS SCIENCE

PEDRO MIGUEL VILELA PEREIRA VALENTIM REBOLA

BSc in Micro and Nanotechnology Engineering

OPTIMIZATION OF A SCATTERING METALLIC NANOPARTICLES ARRAY TO BE IMPLEMENTED IN ULTRATHIN CIGS BIFACIAL SOLAR CELLS

MASTER OF SCIENCE IN MICRO AND NANOTECHNOLOGY ENGINEERING
NOVA University Lisbon
September, 2023

NOVA SCHOOL OF
SCIENCE & TECHNOLOGY

DEPARTMENT OF
MATERIALS SCIENCE

OPTIMIZATION OF A SCATTERING METALLIC NANOPARTICLES ARRAY TO BE IMPLEMENTED IN ULTRATHIN CIGS BIFACIAL SOLAR CELLS

PEDRO MIGUEL VILELA PEREIRA VALENTIM REBOLA

BSc in Micro and Nanotechnology Engineering

Adviser: Doctor Jennifer Passos Teixeira
Staff Researcher, Iberian Nanotechnology Laboratory

Co-advisers: Doctor Hugo Manuel Brito Águas
Associate Professor, NOVA University Lisbon

Examination Committee:

Chair: Name of the committee chairperson,
Full Professor, FCT-NOVA

Rapporteurs: Name of a rapporteur,
Associate Professor, Another University
Name of another rapporteur,
Assistant Professor, Another University

Adviser: Name of the adviser present in defense,
Associate Professor, University

Members: Yet another member of the committee,
Full Professor, Another University
Yet another member of the committee,
Assistant Professor, Another University

MASTER OF SCIENCE IN MICRO AND NANOTECHNOLOGY ENGINEERING

NOVA University Lisbon
September, 2023

Optimization of a Scattering Metallic Nanoparticles Array to be Implemented in Ultrathin CIGS Bifacial Solar Cells

Para os meus pais, Paulo
e Margarida

ACKNOWLEDGMENTS

Chegou ao fim esta etapa da minha vida. Depois de 5 anos de muito trabalho e dedicação, muitas saídas com os amigos e muitas dificuldades ultrapassadas, o sentimento de tudo estar a chegar ao fim é realmente intimidante. Nada nos prepara para esta triste/feliz realidade de que eventualmente todos temos de nos fazer à vida. Estes últimos 5 anos foram fantásticos e tenho de agradecer à Faculdade de Ciências e Tecnologias da Universidade Nova de Lisboa por ter tornado isto tudo possível, fornecendo um ambiente incrível, não só para estudar e aprender, mas também para criar conexões que irão durar para a vida toda. Agradeço também a todos os professores que contribuíram para a minha aprendizagem e desenvolvimento, pelo esforço e empenho em fornecer-nos as ferramentas necessárias para sairmos da faculdade com um leque de conhecimento enorme e completo. Por fim, tenho de agradecer a Nano. Uma das melhores escolhas que fiz foi ingressar neste excelentíssimo curso que me trouxe as melhores pessoas que alguma vez conheci e memórias que irão ficar para a vida.

Agradeço imenso à Jennifer Teixeira e ao Pedro Salomé por me terem dado a oportunidade de fazer a tese no INL, no grupo NOA. Todo o apoio e comunicação que recebi ao longo de todo o percurso da Tese foram imprescindíveis para que nunca perdesse o rumo ao trabalho. Agradeço imenso a todas as pessoas do NOA. É realmente um grupo único, com uma dinâmica própria, que me integrou logo desde início e me forneceu as ferramentas necessárias para eu aprender e ganhar autonomia. Obrigado Jennifer, por me teres guiado e motivado durante este percurso, pelo tempo todo a rever a minha Tese, e por toda a paciência e esforço. Obrigado André, por me teres acompanhado nos primeiros meses de trabalho e me teres ensinado tudo o que conseguiste sobre os processos de sala limpa. A tua boa-disposição é contagiante, e fico mesmo grato por todo o tempo que tiraste para me ajudar. Agradeço-te António, por me teres ensinado tudo o que sei sobre simulações óticas, por me ajudares a debater muitos dos resultados, e por me teres ajudado na construção e revisão da Tese. Não me posso esquecer do meu companheiro de sala limpa e grande amigo, Enzo, que me ajudou e apoiou bastante. Muito obrigado! Tornaste as minhas horas de trabalho muito mais agradáveis. Muito obrigado também ao Pedro, que estava sempre disposto a fazer uma pausa comigo para debater resultados. Obrigado pelo apoio e pela boa disposição, debater resultados contigo foi realmente muito divertido. Agradeço a todos os membros do NOA, que sempre me abriram os braços. Admito que não foram meses fáceis, principalmente por estar longe de todos os meus amigos e família, mas esta experiência fez-me crescer bastante e ganhar conhecimentos valiosos para o mundo do trabalho.

Agradeço agora aos meus eternos amigos, por todo o apoio que me deram ao longo de todo o meu percurso de faculdade. Obrigado Pereira, Tomás, Rosa, Francisco, Rodrigo, Henrique, Imaginário, Carolina e Mariana, do fundo do coração, por sempre me fazerem sentir em casa. Obrigado Guilherme, Lisboa, Faneca, Maria, Manuel, Toscano e Mariana, por terem tornado estes 5 anos dos melhores da minha vida, e por estarem sempre lá para mim. Obrigado a todos por todas as memórias que fizemos, todos os sucessos e fracassos por que passámos, e por todas as noitadas. Com vocês eu cresci a aprendi bastante.

Obrigado pai, mãe, Paulo, avó Deolinda, avô João, e avô Rebola, por todo o apoio e motivação, e por terem tornado isto tudo possível. Sempre foram e sempre vão ser a minha casa. Adoro-vos. Obrigado Tati, César e Tomás, Chica e Pepe, por todo o apoio, alegria e felicidade, e todos os jantares de conversa, boa música e boa vinhaça. Irão sempre ser a minha segunda casa, no Norte.

Por fim, obrigado Margarida, pelo quase esforço de teres vindo comigo para Braga. Obrigado por estares sempre ao meu lado e me apoiares, por me animares quando preciso, pela paciência que tens para mim, por todas as horas de anime que vimos juntos e por todos os passeios que fizemos para espairecer. Obrigado por me ajudares a crescer e a ser uma melhor pessoa todos os dias. Entendes-me como ninguém, e estou-te eternamente grato, por tudo.

“There’s always a siren
Singing you to shipwreck.”
(Thom Yorke)

ABSTRACT

The global energy demand has been increasing, so the development of renewable energy sources is imperative, more specifically, the photovoltaic. One of these technologies is Cu(In,Ga)Se_2 (CIGS), and due to the use of scarce materials, the reduction of the absorber layer to the sub-micrometre scale (ultrathin) has been studied. However, this reduction leads to incomplete light absorption and recombination losses at the interfaces, highlighting the need for light management strategies. Ultrathin bifacial solar cells allow light absorption from both surfaces, providing an additional energy-yield gain, and by integrating light-dispersive metallic nanoparticles (NPs) at the rear interface, this improvement can be even more significant. Finite-difference time-domain optical simulations were performed to study the viability of a plasmonic periodic architecture in an ultrathin CIGS bifacial solar cell. For this purpose, a periodic square array of NPs on an indium tin oxide (ITO) rear contact was optimized, considering two different metallic NPs, Au and Ag, encapsulated with different dielectric materials, SiO_2, Al_2O_3, HfO_2, and TiO_2. From the studied architectures, a NPs' radius of 80 nm and an interdistance of 150 nm, encapsulated with 10 nm of TiO_2, resulted in the best performance for Au and Ag NPs, with a short-circuit current density increase of 6.19 and 6.92 %, respectively. In order to obtain a plasmonic NPs-based architecture with the desired properties, two different approaches were studied. Thermal dewetting of Au thin films was performed for different process conditions, obtaining random arrays of NPs. A study of how the annealing was affecting ITO substrate's properties was conducted, followed by a process optimization consisting in changing the annealing atmosphere and decreasing ITO's roughness. On the other hand, a lithographic process based on nanoimprint lithography was also developed and optimized to obtain a periodic square array of NPs, by varying the parameters at different process stages.

Keywords: nanoparticles; plasmonic; light management; thermal dewetting; nanoimprint lithography; FDTD; ultrathin; CIGS; bifacial solar cells.

RESUMO

O aumento da demanda de energia evidencia a necessidade de desenvolvimento de fontes de energia sustentáveis, nomeadamente, a fotovoltaica. Uma destas tecnologias é $Cu(In,Ga)Se_2$ (CIGS), que utiliza materiais escassos, pelo que a redução da sua espessura para a escala sub-micrométrica (ultrafino) tem vindo a ocorrer. No entanto, esta redução leva à absorção incompleta da luz e perdas por recombinação nas interfaces, evidenciando a necessidade de estratégias de manipulação de luz. Células solares bifaciais ultrafinas permitem a entrada de luz por ambos os lados, proporcionando um aumento de rendimento energético, que pode ser mais significativo com a integração de nanopartículas (NPs) metálicas na interface traseira, que dispersam a luz incidente. Realizaram-se simulações óticas através do método de diferenças finitas no domínio do tempo para estudar a viabilidade da integração de uma arquitetura periódica plasmónica numa célula solar CIGS bifacial ultrafina. Uma arquitetura periódica de NPs em óxido de índio dopado com estanho (ITO) foi otimizada, considerando NPs de Au e Ag, encapsuladas com SiO_2, Al_2O_3, HfO_2 e TiO_2. A disposição periódica com NPs de raio= 80 nm e espaçamento= 150 nm, encapsuladas com 10 nm de TiO_2, apresentou um melhor desempenho para NPs de Au e Ag, levando a aumentos de densidade de corrente de curto-circuito de 6.19 e 6.92 %, respetivamente. Foram estudados dois métodos de fabricação para a obtenção de uma prova de conceito para uma arquitetura baseada em NPs. *Thermal dewetting* de filmes finos de Au em ITO foi efetuado para diferentes condições de processo, obtendo-se NPs aleatórias. Efetuou-se um estudo da variação das propriedades do ITO com o tratamento térmico, e otimizou-se o processo considerando diferentes atmosferas e através da redução da rugosidade do ITO. Um processo litográfico baseado em litografia por nanoimpressão foi também desenvolvido e otimizado, variando as condições dos diferentes passos do processo.

Palavas chave: nanopartículas; plasmónica; manipulação de luz; termal dewetting; litografia por nanoimpressão; FDTD; ultrafino; CIGS; células solares bifaciais.

CONTENTS

LIST OF FIGURES

LIST OF TABLES

ACRONYMS

AFM	Atomic Force Microscopy
AR	Anti-Reflective
ASL	Anti-Sticking Layer
AZO	Al-doped ZnO
BFSC	Bifacial Solar Cell
BIPV	Building-Integrated Photovoltaic
CA	Contact Angle
CIGS	$Cu(In,Ga)Se_2$
c-Si	Monocrystalline Si
FDTD	Finite-Difference Time-Domain
FI	Front Illumination
FOM	Figure of Merit
HMDS	Hexamethyldisilazane
IPA	Isopropyl Alcohol
IPS	Intermediate Polymer Stamp
IR	Infrared
ITO	Indium Tin Oxide
i-ZnO	Intrinsic ZnO
LSP	Localized Surface Plasmon
ND	Nanodisc
NIL	Nanoimprint Lithography
NIR	Near Infrared
NP	Nanoparticle
PCE	Light to Power Conversion Efficiency
PML	Perfectly Matched Layer
PV	Photovoltaic
PVD	Physical Vapour Deposition
RI	Rear Illumination
RMS	Root Mean Squared
RTP	Rapid Thermal Process
SEM	Scanning Electron Microscopy
SLG	Soda-Lime Glass
SQ	Shockley-Queisser
TCO	Transparent Conducting Oxide

TFSF	Total-Field Scattering-Field
TMAH	Tetramethylammonium Hydroxide
UV	Ultraviolet
Vis	Visible
XRD	X-Ray Diffraction

SYMBOLS

Symbol	**Name**	**SI Unit**
a	Nanoparticle’s Interdistance	m
ABS	Total Light Absorbance	%
c	Speed of Light in Vaccum	$m.s^{-1}$
d	Periodic Holes’ Diameter	m
d_{Au}	Au Thin Film Thickness	m
d_{pass}	Passivation Layer Thickness	m
$\|E\|^2$	Electric Field Intensity	$V^2.m^{-2}$
h	Planck’s constant	m2.kg.s-1
$I_{AM1.5}$	AM1.5 Solar Irradiance Spectrum	$W.m^{-2}$
J_{SC}	Short-Circuit Current Density	$A.m^{-2}$
n	Refractive Index	-
p	Periodic Holes’ Pitch	m
P_{ABS}	Power Absorbed per Unit of Volume	$W.m^{-3}$
q	Elementary Charge	C
Q_{abs}	Normalized Mie Absorption Efficiency	-
Q_{scat}	Normalized Mie Scattering Efficiency	-
r	Nanoparticle’s Radius	m
R_S	Sheet Resistance	$\Omega.sqr^{-1}$
SC	Surface Coverage	%
SFE	Surface Free Energy	$J.m^{-2}$
t	Annealing Dwelling Time	s
T	Annealing Temperature	K
ΔJ_{SC}	Difference in Short-Circuit Current Density from a Reference	$A.m^{-2}$
$\Delta J_{SC,Front}$	Difference in Short-Circuit Current Density from a Reference for Front Illumination	$A.m^{-2}$
$\Delta J_{SC,Overall}$	Difference in Short-Circuit Current Density from a Reference Considering Front and Rear Illuminations	$A.m^{-2}$
$\Delta J_{SC,Rear}$	Difference in Short-Circuit Current Density from a Reference for Rear Illumination	$A.m^{-2}$
ε''	Imaginary Part of the Dielectric Permittivity	$F.m^{-1}$
λ	Wavelength	m
π	Ratio of a Circle’s Circumference to its Diameter	-
ω	Angular Frequency	$rad.s^{-1}$

MOTIVATION AND OBJECTIVES

In this world where technology is always evolving, the energy demand is constantly increasing, and it's expected to continue to grow in the upcoming years.[1] For a long time, fossil fuels, such as coal, petroleum, and natural gas, have been used as the main energy sources to meet the growing energy demand, but the associated negative environmental effects cannot be ignored.[2–4] Furthermore, there is currently a global tendency to replace these conventional energy sources with renewable ones, providing environmental protection, an environment free of pollution, and long term energy security and economic benefits.[2–4] However, to meet this growing demand, there needs to be a massive technological advancement in renewable energy sources, but also better energy management and new strategies to produce and distribute energy more efficiently.[5]

Solar energy is one of the most promising contenders, consisting of a practically infinite renewable energy source. Nowadays, there are several photovoltaic (PV) technologies available in the market, with the leading one being made from silicon wafers, but this technology is reaching its development limits, sprouting an interest in the research, development, and improvement of potentially better alternatives.[5] Thin film solar cells appear as a promising alternative, with less use of raw materials- reducing their cost and the environmental impact- and the possibility to be produced in flexible substrates, enabling roll-to-roll production and the use in building integrated PV (BIPV).[6,7] Amongst the thin film technologies, $Cu(In,Ga)Se_2$ (CIGS) stands out, with a record light to power conversion efficiency (PCE) of 23.35 % [8], thanks to its direct bandgap that allows a high absorption coefficient, and its tuneable bandgap.[9,10] However, the scarcity of the materials used in CIGS raises sustainability and economical concerns. To solve these issues, a reduction in the CIGS thickness to the sub-micrometre scale is a promising approach, that has been getting more attention recently.[5] However, the ultrathin CIGS technology has a record PCE well below their thin film counterparts, at 15.2 % [11], mostly due to incomplete light absorption and interface recombination losses.[5] These optical losses are usually solved by implementing light management strategies, which have been shown to improve the overall solar cell's performance.[5] Nevertheless, the implementation of these strategies can prove to be challenging, especially at the rear contact, because of the harsh deposition conditions of CIGS.[5,6] In addition, most high efficiency light management strategies require high resolution nanofabrication procedures, which can significantly increase the production costs and decrease the throughput. Furthermore, the development of nanofabrication processes that ensure scalability while maintaining reproducibility and resolution can possibly propel the ultrathin CIGS technology into the PV market. The implementation of a bifacial solar cell (BFSC) approach in ultrathin CIGS solar cells can also improve their PCE, by allowing the absorption of direct and diffuse sunlight from both front and rear surfaces, providing an additional energy-yield gain.[12–15] However, the replacement of the back contact for a transparent conducting oxide (TCO) is challenging, with most TCOs reacting with the CIGS absorber creating a resistive layer, or degrading with relatively high-temperature process conditions. Furthermore, the development of effective passivation strategies and the optimization of CIGS fabrication methods is very important for the ultrathin CIGS BFSC approach to be viable and reach the market.

The focus of this Thesis is to design a transparent plasmonic substrate to be implemented in ultrathin CIGS BFSCs, as a light management strategy. These substrates consist of Au nanoparticles (NPs) on indium tin oxide (ITO) that can scatter incoming light, increasing the optical path length inside the absorber layer. Finite-difference time-domain (FDTD) optical simulations were performed using the Lumerical software, to optimize the architecture and materials of the NPs array, and to study and discuss the optical phenomena that enhances the performance of a CIGS BFSC. From an experimental point of view, two proof of concept approaches were tested: a random array of plasmonic NPs obtained through the thermal dewetting of a thin film; a periodic square array of plasmonic NPs obtained through a nanofabrication process based on nanoimprint lithography (NIL).

1

INTRODUCTION

1.1 – Thin Film CIGS Solar Cells

Nowadays, the leading PV technology made from silicon wafers is reaching its development limits, technologically and economically, sprouting an interest in the research, development, and improvement of potential alternatives.[5] One of which is the CIGS technology, that has been getting attention in recent years.[16] Thin film CIGS solar cells have remarkable characteristics, such as: direct bandgap which allows for a high absorption coefficient, up to 10^5 cm^{-1} [9]; a tuneable bandgap (1.01-1.67 eV)[10] that allows to implement a bandgap grading, or to be implemented in a tandem solar cell [17]; great thermodynamic stability [5]; potentially cheaper than Si technology, because of its high absorption coefficient that allows for a thinner absorber layer[5,9,18], and consequently lighter solar cells; they can be grown on flexible and rigid substrates, diversifying the applications [9,16,19–21]; has an energy payback time of less than a year.[5,16] Thin film CIGS solar cells have a PCE record of 23.35 % [8], which is still lower than the efficiency of the monocrystalline Si (c-Si) champion cell, 26.6 %.[22] This difference comes mostly from the cell structure complexity gap that exists between both technologies, more specifically, the lack of light management and interface passivation strategies from the CIGS technology. With the increase in efficiency - from implementing light management and interface passivation strategies, and improvement of production techniques - and the reduction in production costs by decreasing the thickness of the absorber layer, CIGS technology could potentially dominate over Si. [5,10,23]

A schematic representation of a conventional thin film CIGS solar cell is presented in *Figure 1.1*. The substrate is usually soda-lime glass, SLG, however, it can also be a flexible substrate such as polyamide film or stainless steel.[16,20] On top of the substrate, the rear contact is deposited, and it is usually a thin layer of Mo, since it has good electrical conductivity, provides good adhesion, and when the CIGS layer is deposited on top, a thin interface layer of $MoSe_2$ is formed, resulting in a quasi ohmic contact.[5,24] Then, there is the CIGS absorber layer, that is a p-type direct bandgap semiconductor, that forms a heterojunction with the CdS n-type buffer layer. The deposition of the CIGS is very versatile, with the possibility of being deposited with vacuum and non-vacuum techniques.[9,16,19] In addition, the bandgap can be adjusted by varying the composition ratio of Ga and In, and usually the CIGS layer is graded, which allows a better band alignment with the CdS layer and creates a field effect at the rear contact that repels electrons, maximizing absorption and minimizing recombination at the Mo/CIGS interface.[5,10,18,25] Following the heterojunction, there is a window bilayer composed of an intrinsic ZnO (i-ZnO) layer and an aluminium doped ZnO (AZO) layer. The AZO layer acts as the top contact and is also a TCO, allowing the light to pass through to the layers below. The i-ZnO layer is highly resistive and prevents shunt contacts between the CdS and the AZO layers.[26,27] Usually, an anti-reflective (AR) MgF_2 layer is also deposited on top, followed by the metal contacts. The PCE of thin film CIGS solar cells is still far from reaching the single junction solar cell efficiency upper limit of around 33% [28], established by the Shockley-Queisser (SQ) limit, which means that there is still significant room for improvement.

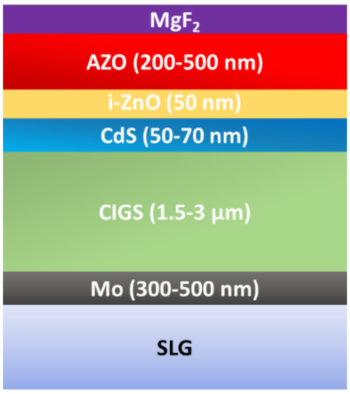

Figure 1.1- Schematic representation of a conventional thin film CIGS solar cell, with the typical thickness for each layer. Not to scale.

1.2 – Ultrathin CIGS Solar Cells and Demand for Light Management

The reduction of the production cost of thin film CIGS solar cells can be achieved through the reduction of the raw materials used, especially of In and Ga, which are scarce and expensive materials.[5,7,29,30] Ultrathin CIGS solar cells have an absorber thickness in the range of 200-500 nm, which effectively reduces the volume of these materials used, in comparison to the 1500-3000 nm used in the thin film approach.[5,9,31] However, this reduction also increases optical losses and rear interface recombination, hindering the solar cell's performance.[5] The main cause for the optical losses in ultrathin CIGS is incomplete light absorption - as the absorber layer becomes thinner, the incident light cannot be absorbed in a single pass, leading to a decrease in the short-circuit current density, J_{SC}.[5] This decrease in absorption is predominant in the NIR and IR, because as the absorber gets thinner, the longer wavelengths, λ, cannot be efficiently absorbed.[5,6,32,33] Nonetheless, thin film and ultrathin CIGS solar cells both suffer from the same problems that cause significant optical losses - shading from the metal contact grids, and reflection and parasitic absorption from the buffer and window layers.[5,34]

The current ultrathin CIGS champion solar cell, with an absorber thickness of 490 nm, has a PCE of 15.2 % [11], which is still far from the 23.35 % for the thin film counterpart, with an absorber thickness of 2500 nm.[8] This significant gap reinforces the need to tackle the incomplete light absorption problem of the ultrathin CIGS solar cells, by implementing light management strategies and optimizing the cell's structure.[5,30,33,35–39]

1.3 – Bifacial CIGS Solar Cells

Novel solar power concepts have been developed for large scale PV installations, and one of the most promising ones is BIPV [12,40], where PVs are integrated into buildings' features, such as facades or rooftops.[13] BIPV in urban environments eliminate the need for additional installation sites, while also meeting the large-scale PV demands, reducing electrical transmission losses, the need for more energy storage capacity, and installation costs.[12,40] BFSCs are an important innovative approach being researched in this field, consisting of an absorber layer sandwiched between two TCOs, allowing the absorption of direct and diffuse sunlight from both front and rear surfaces, and consequently providing an additional energy-yield gain.[12–15] Furthermore, absorbing light from both sides makes the BFSCs a promising technology to be integrated in vertical architectural elements that are alternatively illuminated from the front and back during the day, or in a place where the back side of the module can take advantage of the surrounding albedo.[13,15]

CIGS is one of the most promising materials to be used in BFSCs, but the replacement of the Mo rear contact with a TCO has been challenging. For CIGS BFSCs, the front contact can remain the n-type TCO, AZO, however, for the rear contact, in theory, a p-type TCO should be used. P-type TCOs usually have a low electrical conductivity, so the solution is to use a highly conductive n-type TCO, like ITO.[13–15,41] The CIGS layer is usually deposited by multi-step thermal co-evaporation processes, where the substrate reaches temperatures higher than 500 ºC, which can significantly degrade the TCO's properties, and it promotes the diffusion of Ga into the TCO, leading to the formation of a highly resistive Ga_2O_3 layer that limits the J_{SC} value of the cell.[13,14] In addition, the TCO blocks the diffusion of Na from the SLG to the CIGS, which hinders the electrical performance of CIGS BFSC.[41,42] Nonetheless, thin film CIGS BFSCs with efficiencies of 19.77 % and 10.89 %, for front illumination (FI) and rear illumination (RI), respectively, have been developed.[43]

1.4 – Rear Light Management Strategies

At the rear side of the ultrathin CIGS solar cell, light management strategies are used to increase the optical path length inside the absorber, by promoting light scattering and/or reflection. Usually, Mo is used for the rear contact in CIGS solar cells [5,8,44,45], because of its advantageous properties such as high mechanical stability, high melting point, and low elemental diffusion to the CIGS absorber layer, which allows it to withstand the harsh conditions of CIGS deposition.[5,46,47] However, the Mo rear contact has low reflectivity, causing significant parasitic absorption, especially in ultrathin CIGS solar cells, highlighting the need for light management strategies or the use of different rear contact materials.[5,32,48] The most common approach to solve these problems is to replace the Mo rear contact by a more reflective metal, such as Au or Ag, but at the typical process temperatures needed to grow the CIGS layer, they diffuse into it, affecting the solar cell's performance.[5,6,49] An alternative approach is to use a TCO as the rear contact, however, during CIGS deposition a thin highly resistive Ga_2O_3 layer is formed because of the low thermal stability of the TCOs.[30,50] By adding Ag during the CIGS deposition, the process temperature can be decreased, preventing the resistive layer from forming and allowing the use of a TCO as the rear contact.[30,51] Furthermore, TCOs can be used as the rear contact with a highly reflective metal underneath [5,50,52,53], significantly improving the optical path length, or in BFSC, with light entering from both sides.[12–15] Nonetheless, the incomplete absorption of the NIR and IR light is still an issue that needs to be tackled, and it can be solved with the implementation of scattering structures that resonate in that spectral range.[5,33] One of these strategies is to use dielectric nanostructures, which are thermally and chemically stable, have practically no parasitic absorption, and resonate for a specific λ range.[5,6,54] When these resonant architectures are fabricated as periodic arrays, with precise geometrical parameters to obtain the desired resonance, a PCE enhancement can be obtained.[5] However, for an efficient scattering effect, dielectric structures with large features are needed, which can hinder the solar cell's electrical performance.[5,55] Another possible strategy is the implementation of metallic NPs at the Mo/CIGS interface, that increase the optical path length by scattering incoming light [5,56,57], as seen in Figure A.1.1. Through plasmonic resonance, metallic NPs have a more intense light scattering effect than the dielectric nanostructures, meaning that smaller NPs are needed to reach the same scattering effect, reducing the negative effects of texturization.[5,6] In addition, metallic NPs are more beneficial to module production, and can be tailored to resonate for the desired λ range.[5,6,33,58–60] On the other hand, they introduce parasitic absorption, have low thermal stability, and can diffuse into the absorber layer, so a good encapsulation is required.[5,6,33,61–63]

In this work, high-performance substrates will be developed to be implemented in an ultrathin CIGS BFSC, consisting of a metallic NPs array on an ITO coated SLG substrate, with the geometrical dimensions determined through FDTD numerical model optical simulations.

1.5 – Plasmonic Effect of Metallic NPs

Metallic NPs have been studied as a rear light management strategy because of their plasmonic properties that allow them to scatter incoming light, increasing the optical path length inside the absorber. The metallic NPs resonate for a specific λ range, a phenomenon called localized surface plasmon (LSP).[5,56,57,64–66] As the NP is irradiated with light, the external electrical field interacts with it and the conduction electrons are pushed to the opposite side, creating a dipole. The internal electric field of the NP will then attract the created dipole back to its original state, and this cycle repeats, creating oscillatory movements.[5,56,57] LSP allows the amplification of an incident electromagnetic field, with its maximum value for the LSP resonant frequencies of a NP, promoting a high scattering cross section and some parasitic absorption.[5,56,67,68] The LSP resonant frequencies will depend on the characteristics of the NPs, such as size (diameter), shape, composition, dielectric medium and NP-NP interactions.[5,56,57] The two main mechanisms originated from LSP that can enhance the solar cell's performance are near field and far field scattering. The near field consists of an evanescent electromagnetic field in the vicinity of the NP's surface that can enhance CIGS absorption if the NP is close to the absorber. The far field is related to electromagnetic waves that are generated at a distance larger the NP's size.[5,58]

Thermally driven solid-state diffusional dewetting, referred to as just thermal dewetting, is one of the fabrication processes to obtain NPs. It is a scalable, and relatively simple process that allows the formation of randomly distributed NPs on an irregular surface through self-assembly.[69–71] It consists in the thermal annealing of a thin metallic film, promoting the nucleation and growth of holes within the film that eventually cross each other and create the NPs.[69,70] NPs' arrays with the desired properties can be obtained with a good control of the process parameters, such as: annealing temperature (T) and dwelling time (t); initial Au thin film thickness (d_{Au}); thin film and substrate materials system; nature and number of defects in the film; and roughness of the substrate.[70,72,73]

In this Thesis, the scattering properties of metallic NPs arrays will be studied to be integrated in an ultrathin CIGS BFSC. In order to have the desired plasmonic effect, with the resonance peaks at the NIR and IR regions of the solar spectrum, a fine control of the NPs' geometrical properties is needed. Two proof of concept approaches were studied: a random array of Au NPs obtained through thermal dewetting of a Au thin film; and a periodic square array of Au NPs obtained through a nanofabrication process based on NIL.

1.6 – Optical Simulations- FDTD Solutions Package from Lumerical

Optical modelling and simulations constitute an important part of the PV research field, in the design, analysis and optimization processes.[74] Those predict how a specific concept or design performs in a solar cell and enable a much faster and efficient optimization of devices, when compared to iterative experimental methods.[74] This is specifically relevant for this Thesis, in which an optimization of geometrical parameters and materials for the encapsulated metallic NPs array integration in ultrathin CIGS solar cells was made. Through simulations, the optical phenomena caused by this light management strategy can be optimized to meet the set requirements.

There are various methods to simulate light interactions with a solar cell and implemented light management structures, but only a few can accurately simulate complex geometries with a size smaller or at the same scale as the incident λ. FDTD numerical model appears as a reliable and rigorous method that can simulate broadband and transient light interactions with λ and sub-λ features, within a solar cell, e.g., plasmonic metallic NPs and nano-texturized surfaces. FDTD solves Maxwell's equations, retrieving direct time and space solutions by determining the electromagnetic field components of light, for complex geometries.[5,30] To accurately describe the light interaction with matter, FDTD often needs a very dense spatial sub- λ discretization, which can increase the complexity of the simulations and the computational resources needed, so there always needs to be a compromise.[5]

FDTD optical simulations have been used to test and optimize light management strategies before being implemented in solar cells. One of these strategies is the implementation of resonant metallic NPs on solar cells, either as an antireflection approach on top, or as a scattering strategy on the absorber/rear contact interface.[5] Usually, the FDTD optical simulations are used to optimize the NPs array, by doing parameter sweeps for their radius (r), shape, interdistance (a), and/or surface coverage (SC), in order to improve the solar cell's overall PCE. For CIGS solar cells specifically, this approach has been getting more attention recently, with promising results.[33,61,64,75–77] For example, in the study by Royanian et al. [75], Au NPs on top of the window layer of a thin film CIGS solar cell were simulated using FDTD, varying their r and a, with the optimized architecture reaching a PCE of 19%, in conjunction with a graded absorber layer. Hasheminassab et al. [64], made a similar study, but Ag NPs were used, and their shape was also studied, reaching a PCE of 18.3 % for the optimized architecture with cylindrical NPs. In the study by Zarerasouli et al. [76], FDTD optical simulations were made to improve the absorption and PCE of an ultrathin CIGS solar cell with an absorber thickness of 120 nm, by optimizing the NPs array implemented on top of the rear contact, reaching a PCE of 11.34 % for cubic Ag NPs. The optimization of metallic NPs arrays using FDTD simulations, has also been done for other types of solar cells, such as perovskite [78,79], P3HT:PCBM [80,81], InP [82], and GaAs nanowire [83] solar cells.

For the FDTD analysis, the two main parameters that are usually estimated are the total light absorption (ABS(λ)) for a specific layer or feature, and the J_{SC}. The power absorbed per unit of volume (P_{ABS}) for a given layer can be determined using the electrical field intensity distribution in the corresponding material [84]:

$$P_{ABS} = \frac{1}{2}\omega\varepsilon''|E(\lambda)|^2 \qquad (1)$$

where ω is the angular frequency of the light, ε'' is the imaginary part of the dielectric permittivity, and $|E|^2$ is the intensity of the electrical field. The ABS can then be calculated by integrating the normalized P_{ABS} over a specific volume:

$$ABS(\lambda) = \int \frac{P_{ABS}}{P_{AM1.5G}} dV \qquad (2)$$

The J_{SC} is determined using the following expression [84]:

$$J_{SC} = \frac{q}{hc}\int \lambda ABS(\lambda) I_{AM1.5}(\lambda) d\lambda \qquad (3)$$

in which q is the elementary charge, h is Planck's constant, c is the speed of light in vacuum, and $I_{AM1.5}$ is the solar irradiance spectrum. It is important to notice that for the calculation of the J_{SC} it is assumed that the internal quantum efficiency of the simulated solar stack is equal to 1, which means that every photon that is absorbed by the absorber layer generates an electron-hole pair, and all these charges are collected. Thus, only the optical performance of the device is studied.

The resonance of plasmonic metallic NPs is studied by determining the normalized Mie absorption (Q_{abs}) and scattering (Q_{scat}) efficiency curves, for the considered λ range. These curves heavily depend on the NP's characteristics such as r, shape, and a.[56] Q_{abs} and Q_{scat} are calculated by normalizing the corresponding power to the light source intensity and to the cross-section of the NP:

$$Q_{abs/scat} = \frac{P_{abs/scat}}{I_{AM1.5} \times \pi r^2} \qquad (4)$$

P_{abs} and P_{scat} are calculated using *Equation (1)*.

FDTD optical simulations will be used to perform parameter sweeps for the NPs' r and a, varying the NPs and passivation materials, in order to determine the best architecture and materials for the NPs array for an ultrathin CIGS BFSC. This numerical method will also be used to study the plasmonic NPs resonance for different architectures, and parasitic absorptions that may be causing J_{SC} losses.

2

MATERIALS AND METHODS

2.1 – Optical Simulations- FDTD

2.1.1 – Parameters' Sweep

In order to find the best materials and geometrical parameters for the NPs square array and passivation layer, that maximize the J_{SC} in ultrathin CIGS BFSCs, optical simulations were made with the FDTD solutions package from the Lumerical software, varying the NPs' r, a, and material, and the passivation layer thickness (d_{pass}) and material, for FI and RI. This method solves Maxwell's equations for the simulated architecture, allowing the determination of frequency-dependent electromagnetic fields.[39,85]

The simulation setup is presented in *Figure 2.1*, where it can be observed that the passivated NP is implemented in an ultrathin CIGS solar cell, with the following configuration: SLG (1.6 mm); SiO_2 barrier layer to prevent Na diffusion (25 nm); ITO rear contact (350 nm); metallic spherical NP and passivation layer; CIGS (500 nm); CdS (50 nm); i-ZnO (50 nm); AZO (200 nm). The complex refractive index values for these materials were taken from: SLG[86]; SiO_2 from in-house spectroscopic ellipsometry measurements; ITO[87]; CIGS[88]; CdS, i-ZnO and AZO[18]. The simulation region was defined considering a single NP from the periodic array, with anti-symmetric and symmetric boundary conditions for the X and Y directions, respectively. These boundary conditions enable the simulation of a unit cell while also considering the interaction with electromagnetic fields of other NPs from the periodic array, reducing simulations' time and memory requirements. In the Z directions, a Perfectly Matched Layer (PML) was used, which makes all the light that reaches these boundaries to be absorbed, without any reflection at the interface. Furthermore, the dimensions of the simulation region are determined in X and Y directions by the NP's r and a, and in the Z directions, the upper limit was arbitrarily defined at 500 nm after the AZO layer to have enough space for the light source and the reflectance monitor, and the bottom limit was defined at 400 nm of SLG thickness. For the light source, a broadband plane wave with a λ range of 300-1100 nm and normal incidence was used, simulating the solar spectrum. Since the NPs arrays are to be implemented in bifacial solar cells, the simulations were made for FI and RI, always perpendicular to the interfaces. For RI, to not exceed time and memory limits, only part of the SLG substrate was simulated, being later compensated by considering its absorption, and the reflection at the air/SLG interface before reaching the bottom limit of the simulation region. Also, in the Z directions, the upper limit was defined at 100 nm after the AZO layer, and the bottom limit was defined at 350 nm of the SLG thickness, with the light source at 200 nm of the SLG thickness pointing upwards. With the implementation of NPs in a solar cell, their topography might also be present on the upper layers, which can cause scattering and reflection phenomena on those layers. However, the objective of this Thesis is only to study how plasmonic NPs affect the solar cell's efficiency, so instead of translating the NPs' topography to the upper layers of the solar cell, a CIGS volume compensation approach was followed.

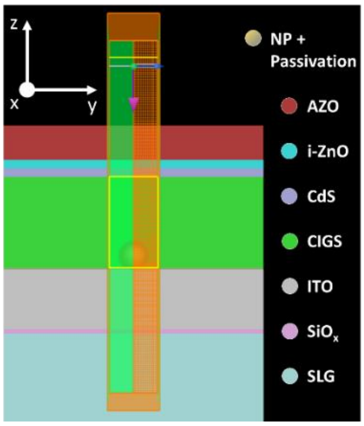

Figure 2.1- FDTD optical simulations setup for the ultrathin CIGS BFSC with passivated NPs implemented.

Initially, parameter sweeps for the NPs' *r* and *a* were made for different combinations of metallic NPs and dielectric passivation materials, for FI and RI, and considering three different d_{pass} values, summarized in *Figure 2.2*. The materials used for the NP were Au and Ag, and for the passivation layer SiO_2, Al_2O_3, HfO_2 and TiO_2, which are usually used for rear contact passivation.[89–94] The complex refractive index values for these materials were taken from elsewhere: Au and Ag [95]; TiO_2 [96]; HfO_2, Al_2O_3 and SiO_2 from in-house spectroscopic ellipsometry measurements. The studied parameters were the NP's *r* (35-80 nm, 5 nm step), the NPs' *a* (25-250 nm, 25 nm step), and the d_{pass} (10, 15, and 20 nm). For all these simulations, a mesh accuracy of 5 was used, corresponding to 22 mesh points per λ value, with override mesh regions with a square size of 1 nm on both CIGS interfaces, and with a square size of 4 nm around the surface of the NP. An ultrathin CIGS solar cell without NPs was also simulated to serve as a reference, without the passivation layer.

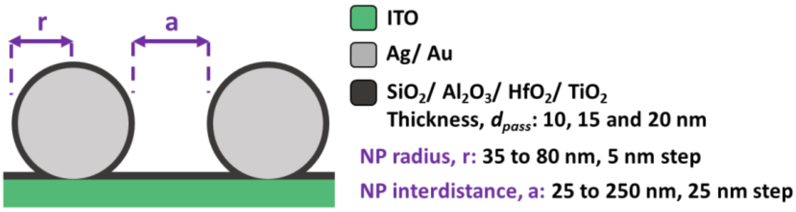

Figure 2.2- Schematic of the materials and geometrical parameters that were studied during FDTD simulations.

2.1.2 – Figure of Merit for Front and Rear Illuminations

After determining the best geometrical parameters and materials for both FI and RI, a compromise between both had to be made to determine the optimal architecture for a BFSC. Normally, the light that reaches the backside of a module is mainly diffused light reflected by the ground and the surroundings, meaning that the spectral albedo of the ground is an important factor. Additionally, there are other factors that affect how much light reaches the backside of the module, such as the elevation and inclination of the module, the presence of other modules nearby and the module location.[97,98] This means that the appropriate model to encompass both illuminations varies with the intended application, but since this is not the focus of this work, a more general approach is ideal. Therefore, a model by Julien et al. [97] will be used, that considers that approximately 15% of the total power of the AM1.5G spectrum reaches the backside of the module, for grass surroundings. This model was developed based on common backside gains for bifacial modules.[98,99] The overall J_{SC} value for each combination of parameters and materials is calculated through:

$$\Delta J_{SC,Overall} = \Delta J_{SC,Front} + 0.15 * \Delta J_{SC,Rear} \qquad (5)$$

Where $\Delta J_{SC,Front}$ is the increase in J_{SC} in relation to the respective non-passivated reference (ΔJ_{SC}) for FI, and $\Delta J_{SC,Rear}$ is the ΔJ_{SC} for RI. This calculated $\Delta J_{SC,Overall}$ will be the figure of merit (FoM) for BFSCs. For the best-found parameters, considering both illuminations, absorbance curves were obtained for the absorber, dielectric and the NP materials, allowing the analysis of parasitic absorptions. For this absorption analysis, the override mesh region square size on the surface of the NP was reduced to 2 nm, increasing accuracy.

2.1.3 – Study of the NPs' Resonance for Different Parameters

The Q_{abs} and Q_{scat} spectra were obtained for arrays of Au NPs with different geometrical parameters, corresponding to five different points of a ΔJ_{SC} map for the best combination of dielectric material and thickness. The setup used for these simulations is presented in *Figure A.1.2*, and it is based on a Mie Scattering 3D set present on the Lumerical application gallery.[100] It consists of nine passivated NPs with a defined r, a, and d_{pass}, in a CIGS medium with a refractive index (n) of 2.966, which is the average n for this material. Nine NPs are used to consider the effect of nearby NPs from the array on the resonance peaks, but it also means that in *Equation 4*, the net power is normalized to the cross-section of nine NPs instead of one. The simulation region was defined around the central NP, as a cube with a side length of 2000 nm, allowing the monitors and the light source to fit inside. There is a plane of symmetry in the Y and Z directions, so, to reduce the simulation time and memory requirements, the boundary conditions were set as symmetric and anti-symmetric at the minimum X and Z, respectively. Scattering and total absorption monitors were set up around the nine NPs, with a total-field scattered-field (TFSF) source with a λ range of 300-1100 nm in between them. This type of source allows to study the scattering of NPs, separating the computation region into a total field region and a scattering field region.[100] A mesh accuracy of 5 was used, with an override mesh region on the NP's surface (1.5 nm). To determine if the resonance simulations were accurately performed, a validation of the general setup was made by comparing the normalized Mie absorption and scattering efficiency curves of a single NP with the curves obtained from the Mie theory. The simulation setup is similar to the one described before, but it only considers one Au NP that is not passivated. The surrounding medium has a n of 1.

2.2 – Random Array of NPs

2.2.1 – Thermally Driven Solid-State Diffusional Dewetting

A thermal dewetting of Au thin films approach on ITO was studied, in order to determine its feasibility to produce Au NPs close to the FDTD target dimensions. The substrate used was a commercially available ITO coated SLG [101]: 1.1 μm SLG; a 25 nm anti-diffusion SiO_2 layer; a 350 nm ITO layer with a sheet resistance (R_s) between 3 and 5 Ω/sqr. The commercial ITO was cleaned with a standard procedure that consists of 15-, 10- and 5- min ultrasonic bath with acetone, isopropyl alcohol (IPA) and water, respectively. Then, the Au thin films with different thicknesses were sputtered onto the substrates at room temperature (100 W DC sputtering on a Kenosistec UHV PVD system) and thermal dewetting was performed at atmospheric pressure in a Termolab Chamber Furnace Type MLM Oven. The obtained NPs depend on different process parameters, and the ones that are being studied here are the initial film thickness, d_{Au}, annealing temperature, T, and dwelling time, t. The annealing temperatures studied were 350 and 500 ºC, and the dwelling times were 2, 4 and 6 h. For the 500 ºC annealing, the initial film thicknesses studied were 2.5, 5, 7.5, 10, and 12.5 nm, for each dwelling time. For the 350 ºC annealing, the initial film thicknesses studied were 2.5, 3, 4, 5, and 7.5 nm, for each dwelling time. The maximum temperature used for the annealing was 500 ºC because the glass transition temperature of the commercial ITO is 564 ºC.[101] For all these conditions, a reference sample with bare ITO was also annealed.

2.2.2 – Thermal Dewetting Optimization

Etching tests were done on the ITO's surface to decrease its roughness and improve the dewetting process. Two different plasmas were tested: 112 s of C_4F_8 plasma (2000 W 13.53 MHz plasma with 50 sccm C_4F_8 flow, 30 sccm H_2 flow, at 0 ºC, 5 mTorr in SPTS APS system) and 112 s of Cl_2 plasma (1300 W 13.56 MHz plasma with 45 sccm Cl_2 flow and 15 sccm CF_4 flow, at 40 ºC, 5 mTorr in SPTS ICP system). Furthermore, to test the effects of surface etching on the final NPs, thermal dewetting was made at 350 ºC for 2 h for d_{Au}= 6 nm on an ITO substrate, for the C_4F_8 plasma etching. Before the Au deposition, residual Teflon from the C_4F_8 etching was removed with a plasma of O_2 and Ar (500 W 2.45 GHz plasma with 600 sccm O_2 and 50 sccm Ar flow, performed on the PVA Tepla Gigabatch 360M system) for 8 min.

In order for ITO to be a good rear contact for bifacial solar cells, it has to have good electrical and optical properties. To better understand how the thermal annealing was affecting the optical, structural, and electrical properties of ITO, thermal annealing was done for 2 h at 250, 350, and 500 ºC. Another parameter that was tested was the annealing atmosphere. Thus, thermal annealing was done at 500 ºC for 2 h in a custom-made rapid thermal process (RTP) oven, at 500 ºC 1 bar, for 2 h, in a N_2 atmosphere, for bare ITO, ITO etched with C_4F_8 plasma, ITO with a d_{Au}= 4 nm, and C_4F_8 plasma etched ITO with d_{Au}= 4 nm.

2.3 – Periodic Array of NPs

To obtain a periodic square array of Au NPs with the desired geometrical parameters determined through FDTD optical simulations, a process based on NIL was developed and optimized. The objective of this approach was to obtain a proof of concept, with a periodic square array of Au NPs.

2.3.1 – Nanoimprint Lithography

For the NIL process, a pattern is transferred from a master stamp to the sample, using an intermediate polymer stamp (IPS). The master stamp consists of a square array of periodic holes with a defined diameter, *d*, pitch, *p*, and depth. Two master stamps were used, one with *d*= 400 nm and *p*=2000 nm, and another with *d*=100 nm and *p*= 600 nm, and both these stamps have a hole's depth of 150 nm. Both these stamps were previously made in-house, and their fabrication procedure is in *Annex A.3*.

The schematic of the process flow for the pattern transfer is presented in *Figure 2.3*. First, the master stamp was cleaned with a plasma of O_2 and Ar (500 W 2.45 GHz plasma with 600 sccm O_2 and 50 sccm Ar flow, performed on the PVA Tepla Gigabatch 360M system) for 8 min, and a thin anti-sticking layer (ASL) was deposited. This ASL is a Teflon-like C_4F_8 polymer (2000 W 13.56 MHz plasma with 200 sccm C_4F_8 flow at 20 °C, 25 mTorr in SPTS Pegasus). The thickness of this layer was 50 nm for the larger pattern stamp and 10 nm for the smaller pattern stamp. The master stamp's pattern was then transferred to the IPS, which is a mouldable UV-curable polymer, with 15 bar of constant pressure at 22 ºC for 60 s, followed by 240 s of UV exposure at the same conditions to cure the polymer. This first pattern transfer will be henceforth referred to as NIL-IPS. The now patterned IPS was then coated with a layer of C_4F_8 in the same conditions as described before and with the same thickness as it was deposited on the master stamp. The last step was to transfer the pattern on the IPS onto the patterning resist (TU7-310), by first heating both the sample and the IPS to 65 ºC for 10 s, followed by 100 s at 15 bar of constant pressure and at the same temperature, and 180 s with UV exposure at the same conditions to cure the resist. This second pattern transfer will be henceforth referred to as STU-NIL.

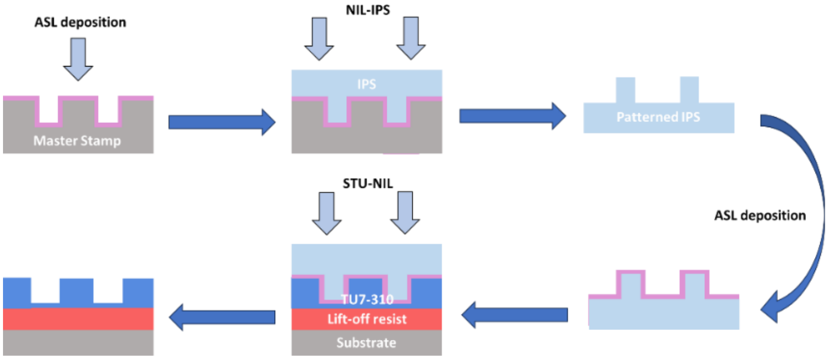

Figure 2.3- Schematic of the process flow for the pattern transfer from the master stamp to the sample.

2.3.2 – Process Flow for the Fabrication of Periodic Arrays of NPs

The schematic of the process flow for the fabrication of the periodic square array of NPs is presented in *Figure 2.4*. First, the Si substrate was cleaned with the standard acetone, IPA and deionised water procedure. Then, the substrate was dehydrated in vacuum with hexamethyldisilazane (HMDS) at 150 ºC for 300 s in the Vapour Prime YES-310TA oven, followed by the deposition by spin-coating of the lift-off resist and the patterning resist, in a Suss MicroTec Gamma Photoresist Cluster system. Initially, for the lift-off resist, it was deposited 500 nm of LOR 5B at 1500 rpm for 45 s, baked at 200 ºC for 180 s. However, with the optimization of the process it was changed to LOR 1A, and it was deposited a 170 nm layer at 1500 rpm for 45 s, baked at 200 ºC for 180 s. For the patterning resist, 300 nm of TU7- 310 were deposited at 3000 rpm for 30 s, baked at 90 ºC for 120 s, which is an appropriate resist for simultaneous thermal and UV (STU) NIL, with a larger thickness than the depth of the master stamp. The thickness of the LOR resists was chosen to allow for the lift-off step, even with the deposition of the Au, but also the decrease in said thickness was made to allow a more vertical Au deposition. The thickness of the TU7-310 was chosen in consideration of the step of the already fabricated NIL master stamps. The next step was to pattern the TU7-310, with the process explained in the previous section, STU-NIL, and to remove the residual layer that always stays after a NIL process. To remove this layer, a plasma of O_2 was used, in a process that will henceforward be called O_2 strip (2500 W 13.56 MHz plasma with 115 sccm O_2 flow, at 20 ºC and 85 mTorr performed in a SPTS Pegasus). During this process, the sample is secured to a Si wafer with a thin layer of thermal wax between them to help dissipate the heat that is generated during the process. The O_2 strip process needs to remove all the residual resist, but it is important to not remove LOR, otherwise the development process after will lose reproducibility. Thus, throughout the optimization process different times of O_2 strip were tested: 20, 23, 25, 27, and 29 s. The next step was to develop the LOR underneath the TU7, and different developer and development times were tested throughout the optimization process. For the LOR 5B, the developer used was AZ400K, with a 1:4 dilution ratio, at 22 ºC for 7 s without rotation, performed in a Suss MicroTec Gamma Photoresist Cluster system. For the LOR 1A, the developer used was tetramethylammonium hydroxide (TMAH), and two concentrations were tested: 2.2% and 1.5% V/V. For TMAH 2.2% the development times tested were 10, 20, 25, and 30 s, and for TMAH 1.5 % the development times tested were 50, 60, 70, and 85 s. Reproducibility tests were also made for the chosen times. The TMAH solutions were made from a 20 % V/V TMAH bottle, and all the developments were manually and individually made. Following the development with TMAH, the samples were immediately immersed in IPA to stop the development process, and dried after with a N_2 flow. It is important to notice that the control of the development process is a vital step in the whole process, because if the development is not enough, the Au will be deposited on top of the LOR and during lift-off it will come off, and if there is too much development the support for the TU7 will not be enough and the whole structure will fall. The next step was to deposit Au nanodiscs (NDs) in the holes created by the development, and two physical vapor deposition (PVD) methods were tested: thermal evaporation of Au pellets on a resistive boat (105 A thermal evaporation at 10^{-5} mbar, performed in a Korvus Hex system with the thermal evaporation source module, using pure Au pellets of 3.175×3.175 mm); sputtering of an Au target (100 W DC sputtering performed on a Kenosistec UHV PVD system). Initially, the evaporation method was used to deposit 100 nm of Au, but it was later changed to the sputtering method, in which different nominal thicknesses of Au were tested throughout the optimization process:10, 15, 20, 25, 40, 50, 60, 70, 75, 80, 90, and 100 nm. Note that the deposition by sputtering is not very directional and the Au target is not directly above the sample, and since the Au is being deposited on cavities a few evident problems arise - the deposition is not completely uniform throughout the sample and the sputtered Au may have some problems getting inside the holes. Also, there might be variations in the quantity of Au deposited on each hole, which will lead to variations in the NPs' size. The evaporation system has a more vertical deposition, but the stage is not centred with the resistive boat, meaning that the deposited Au will not be uniform, even inside the holes, but the thickness of the deposited Au will be closer to the pretended one. Following the Au deposition there is the lift-off to remove the LOR, and it was done with mr-REM 500 resist remover in an ultrasonic bath, at 60 ºC for 30 min. The samples were immersed in IPA right after to remove any traces of the mr-REM 500 and dried with a N_2 flow. Finally, the samples underwent thermal dewetting at 800 ºC for 2 h at atmospheric pressure in a Termolab Chamber Furnace Type MLM Oven.

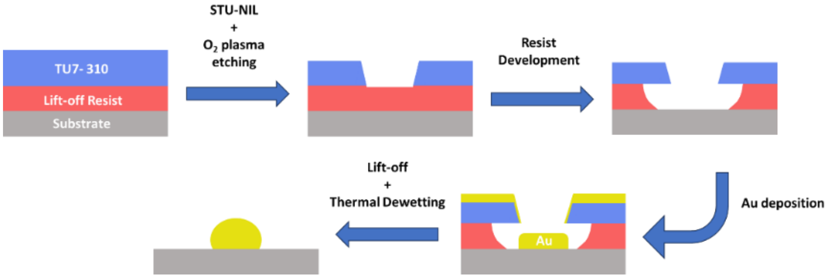

Figure 2.4- Schematic of the process flow for the fabrication of the periodic square array of NPs.

2.4 – Sample Characterization

Accurate characterization methods are vital to process and compare results, and to choose the next steps to take. For the thermal dewetting, all the samples, following any process, were characterized with scanning electron microscopy, SEM, using a NovaNano SEM, and UV-Vis spectroscopy, using a PerkinElmer LAMBDA 950 UV-VIS-NIR Spectrophotometer. The SEM images of the NPs obtained after thermal dewetting were analysed using the ImageJ software, to determine average NPs' r and a, circularity, and SC. The R_S was measured following the thermal annealings, for the reference samples and later for the optimization tests, using a Sheet Resistance Prober by AITCO, that uses the 4-point probe method. Using the sessile drop method in a static regime, and with the Laplace-Young method to calculate the contact angle, the surface free energy (SFE) was calculated using the Owen-Wendt-Rabel-Kaeble method that requires a polar and a dispersive liquid- water and diiodomethane, respectively.[102,103] CA measurements were made right after the annealing, for the reference samples and for the roughness optimization samples. To test if there was formation of other crystalline phases during ITO's annealing, a structural analysis was conducted through X-Ray Diffraction (XRD) during the optimization process in a XRD system by PANalytical. The root mean square (RMS) roughness of the optimization substrates was analysed using Atomic Force Microscopy (AFM) in an AFM Dimension Icon Atomic Force Scanning Probe Microscope by Bruker, with a scanning frequency of 0.3 Hz, and with a SSS-NCH tip [104] in tapping mode.

For the periodic array of NPs, most of the characterization was done in SEM, since the most important part of the optimization of this lithographic process was to visualize how the different process parameters were affecting the different stages of the process. To analyse the SEM images, ImageJ software was used.

3

RESULTS AND DISCUSSION

3.1 – Optical Simulations- FDTD

3.1.1 – Parameters' Sweep

Two different metals were tested for the NPs, Au and Ag, which are the most used plasmonic NPs, because of their high free electron density [105] and LSP resonance effect in the visible region, but also because they can be obtained through simple preparation methods, and can be synthesised over a wide range of sizes and shapes.[106] Ag NPs are more affordable and have a stronger LSP resonance than Au NPs [107], however Au NPs have a higher stability against oxidation, which is crucial for solar cells.[75] Generally, Ag nanostructures have a higher performance than their Au counterparts, as it was demonstrated by FDTD simulations[76], which is explained by their strong scattering and low parasitic absorption.[62] In this section, both Au and Ag NPs will be studied, but the focus of the discussion will be on Au NPs, given that only Au NPs were experimentally produced in this Thesis, since Au does not oxidize, opposite to Ag, making the diffusion of the Au thin film during thermal dewetting easier.

For each simulation, considering the different combination of parameters and materials, for FI and RI, an absorbance spectrum was obtained, and for each parameter sweep, with defined materials and dielectric thickness, a map of ΔJ_{SC} as a function of the NPs' r and a was obtained. The ΔJ_{SC} maps for Au NPs passivated with 10, 15, and 20 nm of SiO_2, for FI, are presented in *Figure 3.1*- a) to c), respectively, while for RI are presented in *Figure 3.1*- d) to f), respectively. These ΔJ_{SC} maps are an example of the general trend that most of the studied material combinations follow. The simulated J_{SC} of a reference ultrathin CIGS BFSC is 26.56 and 24.35 mA/cm^2 for FI and RI, respectively. The ΔJ_{SC} maps for the remaining studied material combinations, for both illuminations, are presented in *Annex A.1*. For FI, for d_{pass}= 10 nm, large NPs with a r range of 75-80 nm and an a range of 125-200 nm originate a higher ΔJ_{SC}, but with the increase in d_{pass}, a new trend that favours NPs closer to each other and with a r range of 60 to 80 nm starts to appear. Considering the optimum NPs' r and a for d_{pass} = 10 nm, there is a blueshift of the resonance peaks with the increase in the d_{pass} value, because the passivation material, with a n lower than CIGS', will cause a decrease of the dielectric medium's average n around the NP.[56] This means that the resonance is moving away from the optimal λ range and losing intensity, causing a decrease in the ΔJ_{SC}.[57] To compensate this loss, a higher density of NPs is needed, in which they are so close together that they interact with each other and their resonance peaks redshift [56,57], improving the absorption in the NIR and IR. This effect is potentiated by the fact that the NPs' encapsulation is connected, without the high n CIGS material between them. For RI, independently of the d_{pass} value, NPs that are distant from each other are favoured, suggesting that the NPs act mostly as a reflector. Furthermore, to have more light passing through and being absorbed by the CIGS, there needs to be a larger a. For both illuminations, the ΔJ_{SC} maps corresponding to a d_{pass}= 10 nm, generally have a larger maximum J_{SC}, when comparing with the maps for the thicker d_{pass} values, which is probably caused by the blueshift of the resonance peaks with the increasing encapsulation thickness.[56] Also, when comparing the ΔJ_{SC} maps of Au and Ag NPs, for the same encapsulation material and d_{pass}, the Ag NPs architectures have a larger maximum ΔJ_{SC}, which is expected, since the LSP effect is stronger and the parasitic absorption lower.[107]

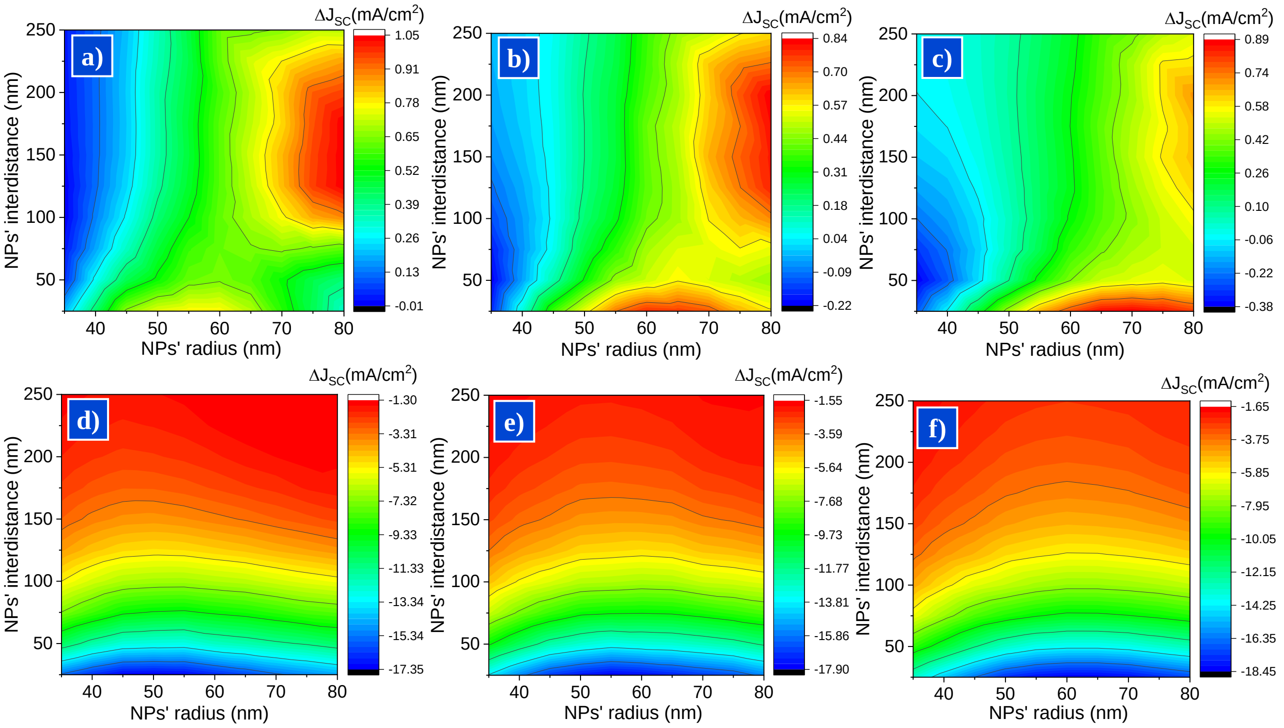

Figure 3.1- Simulated ΔJ_{SC} colour maps for Au NPs passivated with SiO_2 integrated in an ultrathin CIGS BFSC: for d_{pass} = a) 10, b) 15, and c) 20 nm, for FI; for d_{pass}= d) 10, e) 15, and f) 20 nm, for RI. Note that the scale is different for each map.

There are two combinations of materials that, for FI, show a different trend- Au NPs and Ag NPs passivated with TiO_2. *Figure 3.2*- a) to c) are FI ΔJ_{SC} maps for Au NPs passivated with 10, 15, and 20 nm of TiO_2, respectively. These maps are representative of the FI maps for Ag NPs passivated with TiO_2. It can be observed that the optimal NPs' geometrical parameters are r= 80 nm and a= 125 nm, independently of the d_{pass} value, which is a unique trend amongst the different studied material combinations. In addition, when comparing *Figure 3.1*- a) with *Figure 3.2*- a), the maximum ΔJ_{SC} zone starts at lower NPs' r for the TiO_2 encapsulation, due to its higher n in comparison to SiO_2, meaning that there will be a redshift in the resonance peaks[56,57] and the same plasmonic effect is achieved with smaller NPs.

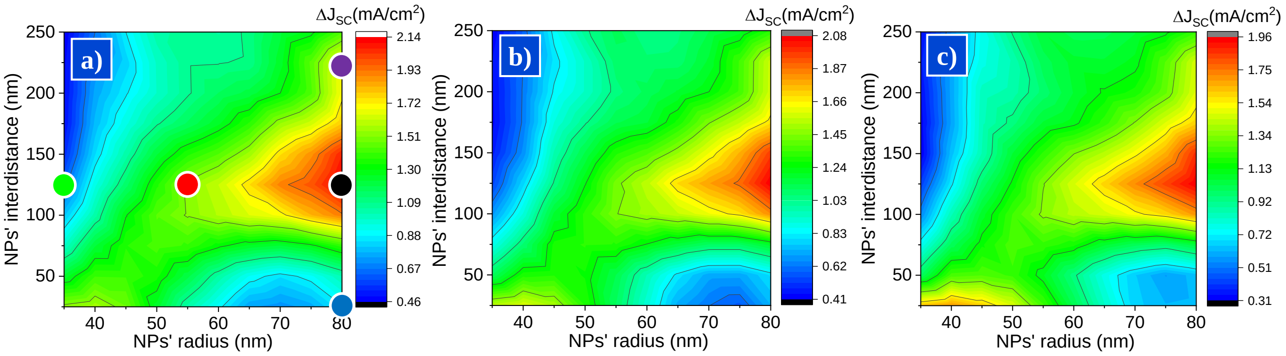

Figure 3.2- Simulated ΔJ_{SC} colour maps for Au NPs passivated with TiO_2 integrated in an ultrathin CIGS BFSC: for d_{pass}= a) 10, b) 15, and c) 20 nm, for FI. Note that the scale is different for each map.

The best geometrical parameters and the corresponding J_{SC} for all the studied combinations are displayed in *Table A.1.10*. Generally, for the same materials combination, the smaller d_{pass} corresponds to the highest J_{SC}, for both FI and RI. For FI, larger NPs with an intermediate a originate the highest J_{SC}, as a denser NPs array provides a more complete light interaction, however, at a certain point, their resonance peaks start to be affected by interactions between NPs, redshifting and losing intensity.[56,57] For RI, NPs that are far from each other originate the highest J_{SC}, because when NPs are not scattering light they are mostly reflecting it, obstructing light transmission to CIGS. It can be observed that for both illuminations, the material combinations that originate the highest J_{SC} are Au and Ag NPs passivated with TiO_2, which is the best encapsulation material due to its higher n, closer to CIGS', that allows for a more uniform surrounding dielectric medium, and consequently, a more intense resonance. These combinations of materials are also the only ones that allow for an increase in the J_{SC}, for RI. For FI, the best combinations are Au and Ag NPs both with r= 80 nm and a= 125 nm passivated with 10 nm of TiO_2, with a J_{SC} of 28.70 mA/cm^2 and 28.92 mA/cm^2, respectively. For RI, the best combinations are Au NPs with r= 55 nm and a= 250 nm passivated with 15 nm of TiO_2, and Ag NPs with r= 60 nm and a= 250 nm passivated with 20 nm of TiO_2, with a J_{SC} of 24.37 mA/cm^2 and 24.81 mA/cm^2, respectively.

3.1.2 – Compromise Between Front and Rear Illuminations

To determine the best geometrical parameters and materials, a compromise between FI and RI had to be made. Using the model from *Section 2.1.2*, in which it is considered that only 15% of the AM1.5G spectrum reaches the backside of a bifacial module, the best overall geometrical parameters, for the studied material combinations, are presented in *Table 3.1*, with the corresponding $\Delta J_{SC,Overall}$. The results for all the d_{pass} values are presented in *Table A.1.11*. From *Table 3.1*, it can be concluded that the highest ΔJ_{SC} value for each combination results from large NPs with r= 80 nm, an a that ranges from 150 to 200 nm, and d_{pass}= 10 nm. These results follow the ones for FI, with a slight increase in the NPs' a to also encompass the RI, since the FoM used puts much more weight on the FI than on the RI. The best combinations of materials and parameters are Au NPs with r= 80 nm and a= 150 nm, passivated with 10 nm of TiO_2, with a $\Delta J_{SC,Overall}$= 1.87 mA/cm^2, and Ag NPs with the same geometrical parameters and passivation, with a $\Delta J_{SC,Overall}$= 2.24 mA/cm^2. Furthermore, the optimal SC for both Ag and Au NPs will be 20.92 %. A NPs array with these geometrical parameters will be sought after in the following experimental sections.

Table 3.1- Best overall geometric parameters for all the studied material combinations, with the corresponding $\Delta J_{SC,Overall}$.

	Combination (NP/Passivation)	Best d_{pass} (nm)	Best r (nm)	Best a (nm)	$\Delta J_{SC,Overall}$ (mA/cm^2)
FI+RI	Au/SiO_2	10	80	175	0.78
	Au/Al_2O_3	10	80	175	0.96
	Au/HfO_2	10	80	175	1.03
	Au/TiO_2	10	80	150	1.87
	Ag/SiO_2	10	75	200	0.82
	Ag/Al_2O_3	10	80	175	1.22
	Ag/HfO_2	10	80	175	1.37
	Ag/TiO_2	10	80	150	2.24

To better understand the optical phenomena happening for these optimal combinations, high accuracy simulations were performed, in which the simulated absorbance by CIGS and parasitic absorbance by the NPs and the dielectric material were determined, for Au/Ag NPs with r= 80 nm and a= 150 nm, encapsulated with 10 nm of TiO_2. *Figure 3.3*- a) and b) correspond to the absorbance spectra for the architecture with Au NPs, for FI and RI, respectively, and *Figure 3.3*- c) and d) for the Ag NPs, for FI and RI, respectively, all compared to the corresponding non-passivated ultrathin CIGS BFSC reference. It can be observed from *Figure 3.3*- a), that the Au NPs, for FI, enable a significant CIGS absorbance increase for λ values higher than 600 nm, and consequently an increase in the J_{SC}, but they are also absorbing light in the NIR and IR regions of the spectrum, which is not ideal and is limiting the ΔJ_{SC}. From *Figure 3.3*- b), it can be concluded that, for RI, the Au NPs are mainly absorbing and reflecting light in the UV- Vis region of the spectrum, which is causing a significant decrease in the CIGS' absorbance and the overall J_{SC}. In the NIR and IR regions of the spectrum the same is happening, but the NP's resonance is in the same region, which leads to an increase in the CIGS' absorbance, in comparison with the reference. By contrast, the Ag NPs' absorbance spectra, from *Figure 3.3*- c) and d), show that they are absorbing much less light, leading to a higher J_{SC}. For RI, even though Ag NPs have a much lower absorption in the UV-Vis region of the spectrum, they are still reflecting light, which is why the CIGS absorbance spectrum is still below the reference. Overall, the performance of the Ag NPs is superior to the Au NPs, which was expected since Ag NPs have a stronger LSP effect and less parasitic absorption.[62,107]

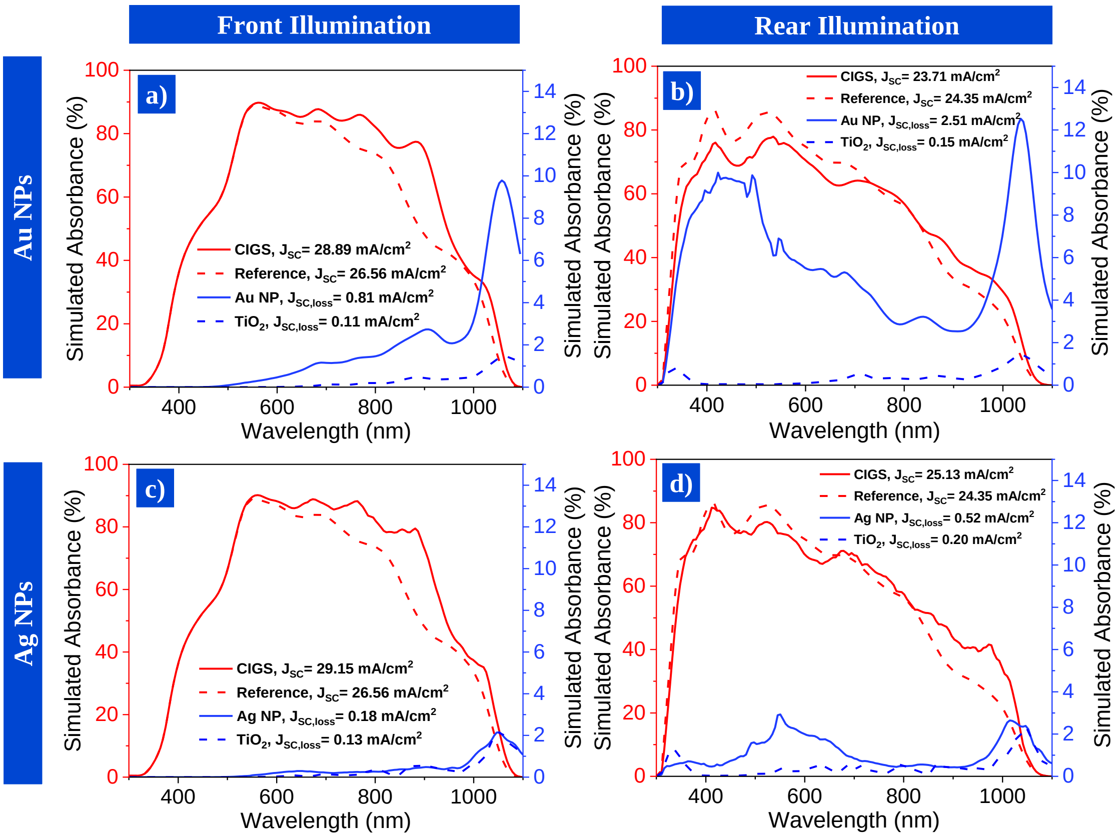

Figure 3.3- Simulated absorbance spectra for the CIGS absorber, NP and passivation layer, for the optimal overall geometric parameters- r= 80 nm and a= 150 nm- for: Au NPs passivated with 10 nm of TiO$_2$, for a) FI and b) RI; Ag NPs passivated with 10 nm of TiO$_2$, for c) FI and d) RI.

3.1.3 – Study of the NPs' Resonance for Different Parameters

To better understand how the geometrical properties of the NPs are affecting their resonance and, consequently, the generated J_{SC}, 5 points of the ΔJ_{SC} map for Au NPs passivated with 10 nm of TiO$_2$ from *Figure 3.2*- a) were chosen to study the normalized Mie absorbance and scattering efficiency of the corresponding NPs, in a CIGS medium. The validation of the simulation model is presented in *Figure A.1.12*. In these simulations, the ITO substrate was not implemented, however, since the *n* of ITO is smaller than CIGS', a small blueshift of the resonance peaks may happen in real-life implementation.[56,57]

The Mie resonance of the NPs depends on a few factors, such as the NPs' size, shape, composition, spatial distribution, and dielectric medium[5,56,57], but for this specific study, the only parameters that will be addressed are the NPs' *r* and *a*. In terms of the NPs' size, as a general approach, there are two main regimes: NPs much smaller than light's λ (smaller than 100 nm), and NPs with size comparable or larger than light's λ (larger than 100 nm).[57] In the small size regime, the electrical field distribution inside the NP is considered uniform, and the electron cloud polarization is coherent in each point of the metallic NP, meaning that the behaviour of the oscillations can be described by a simple dipole.[56,57,108,109] In the large size regime, the electrical field distribution inside the NP is no longer considered uniform, and the electron cloud polarization is no longer coherent for each point of the metallic NP, meaning multipolar plasmon oscillation start to appear.[56,57,108–110] In addition, the ratio between scattered and absorbed photons strongly depends on NP's size.[56,108,109,111] For NPs smaller than the λ of incident light, scattering and absorption effects scale with the 6th and the 3rd power of the NP's size, respectively.[56,108,111] As a result: absorption dominates over scattering for NPs with size much smaller than the light's λ; both effects become comparable at around 50 nm of NPs' size; and scattering begins to dominate for NPs larger than 70-100 nm.[56,108,111–113] The minimum size of the studied NPs is 70 nm, which means that for this analysis, for all 5 combinations of geometrical parameters, it is expected that the NPs present multipolar plasmon oscillations and that the scattering effect is what prevails. The

Mie scattering and absorption efficiency spectra for the 5 different configurations are displayed in *Figure 3.4*- a) and b), respectively. From *Figure 3.4*- a) and b), it can be observed that, for all the NPs arrays, both scattering and absorption curves show more than one peak, and the scattering efficiency is always higher than the absorbing efficiency, confirming the earlier hypothesis. It can be concluded, by observing *Figure 3.4*- a), that for a constant *a*= 125 nm, the increase in the NPs' *r*- from 35, to 55, to 80 nm- causes the scattering spectrum to redshift and broaden, mainly because of the extrinsic size effects that are originated by multipolar plasmon oscillations, which is in accordance with literature.[56,108,110,111,114,115] This effect is causing the most intense scattering peak for NPs with *r*= 80 nm and *a*= 125 nm to shift to a λ higher than 1100 nm, which is why it cannot be seen in *Figure 3.4*- a). From *Figure 3.4*- b) it can be observed that with the increase in the NPs' *r*, while maintaining the *a*, the absorption efficiency peaks become less intense and suffer a redshift and broadening, which is expected, since this increase in size is making the scattering effect dominate.[56,108,111–113,115] The highest J_{SC} corresponds to a NP array with *r*= 80 nm and *a*= 125 nm, which is not the combination of geometrical parameters that has the highest scattering effect, as it can be seen in *Figure 3.4*- a). This can also be explained by the shift in the optical effect that dominates. Even though the NPs with *r*= 35 and 55 nm appear to have higher scattering efficiency, their absorbance efficiency is also significantly larger, which means that they have more parasitic absorbance that is converted to heat [56,116–119], which makes the solar cell's J_{SC} decrease.

LSP of different NPs can influence each other, depending on NPs' *a*, shape and relative light polarization, generating hybrid plasmon modes.[56,120,121] In other words, if NPs from an array are close enough to each other, the electromagnetic field applied on a single NP will be the sum of the electromagnetic fields from the incident light and the surrounding NPs, which modifies the NP's resonance.[57,122–124] In general, the interaction between NPs' plasmon resonances causes a redshift in the resonance band and broadens the peaks.[56,57,121–124] By observing *Figure 3.4*- a), it can also be concluded that for a constant NPs' *r* of 80 nm, the decrease in NPs' *a*- from 225, to 125, to 25 nm- there is a clear redshift and broadening in the main resonant λ peak, at around 900 nm, which is in accordance with literature.[56,57] From *Figure 3.4*- b), it can be observed that the absorption efficiency curves for these three cases are very similar, indicating that the scattering effect is dominating, as expected for this size of NPs. Furthermore, the difference in the generated J_{SC} must come from the differences in the resonance effects. The near scattering field decays very quickly with distance, meaning that, if the NPs are close enough, the generated electrical field on a NP by nearby NPs will present significant amplitude variations throughout the NP volume. This causes the surface plasmon excitation to be uneven, meaning that the movement of the electrons will not be uniform, leading to charge accumulation inside the NP and extra damping of the oscillations.[57] By observing *Figure 3.4*- a), it can be clearly seen that the NPs with *r*= 80 nm and *a*= 25 nm have a smaller scattering effect, which may be caused by the fact the NPs are so close to each other that this damping effect takes place. On the other hand, NPs with *r*= 80 nm and *a*= 225 nm have a higher scattering effect than the NPs with the highest ΔJ_{SC}. As it was mentioned before, the longer λ values are the hardest part of the AM1.5G spectrum to be absorbed by the CIGS layer, because of their lower energy, even with a bandgap gradient, leading to their reflection or parasitic heat generation.[5,125–127] Therefore, NPs that have their resonance for λ above the NIR are desirable, and lead to an increase in the solar cell's J_{SC}. In addition, a blueshift is expected with the introduction of the ITO substrate, that has a smaller *n* than CIGS', so the resonance peaks for the NPs with *r*= 80 nm and *a*= 225 nm would shift even further away from the optimal λ range, and the resonance peaks for the NPs with *r*= 80 nm and *a*= 125 nm would move closer to the optimal λ range. Also, NPs with *r*= 80 nm and *a*= 125 nm, even with a smaller scattering effect, may provide a more complete light interaction than NPs with *r*= 80 nm and *a*= 225 nm, since the NPs' array is denser.

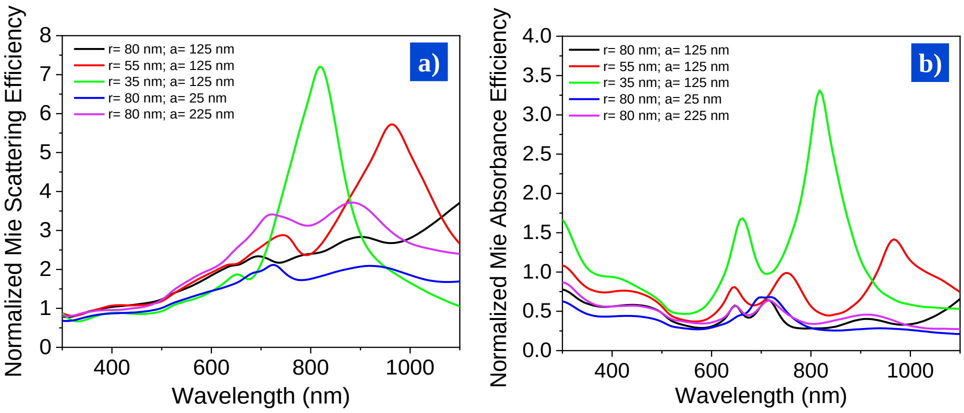

Figure 3.4- Simulated Mie a) scattering and b) absorption efficiency spectra for Au NPs passivated with 10 nm of TiO_2 with different geometrical parameters: r=80 nm, a= 125 nm (black); r=55 nm, a= 125 nm (red); r=35 nm, a= 125 nm (green); r=80 nm, a= 25 nm (blue); r=80 nm, a= 225 nm (purple).

3.2 – Random Array of NPs

3.2.1 – Thermal Dewetting Calibration

Thermal dewetting of Au thin films on ITO was studied and optimized to address its feasibility in the fabrication of Au NPs with the geometrical parameters determined through FDTD, r= 80 nm and a= 150 nm, as a proof of concept, to be implemented as a scattering light management strategy on an ultrathin CIGS BFSC. The process parameters studied were d_{Au}, T, and t.

SEM images of the obtained Au NPs on ITO after thermal dewetting at 500 ºC, for 2 h, for d_{Au}= 2.5, 5, 7.5, 10, and 12.5 nm are presented in *Figure 3.5*- a) to e), respectively, and after thermal dewetting at 350 ºC, for 2 h, for d_{Au}= 2.5, 3, 4, 5, and 7.5 nm are presented in *Figure 3.5*- f) to j), respectively. The SEM images for t= 4 and 6 h, are presented in *Figure A.2.1* and *Figure A.2.2*, for 500 and 350 ºC, respectively. As a general trend, it can be observed that with an increase in the d_{Au}, there is an increase in the NPs size, which is expected.[5,71] From *Figure 3.5*- a) to c) and f) to i), it can be observed that well-defined singular NPs were formed, however, from *Figure 3.5*- d), e) and j), it can be observed that for 500 ºC, for d_{Au}= 10 and 12.5 nm, and for 350 ºC, for d_{Au}= 7.5 nm, the energy provided is not enough to make the Au thin films completely dewett, independently of the t. This is more apparent for t= 4 and 6 h, seen in *Figure A.2.1* and *Figure A.2.2*. The roughness of the substrate is an important parameter that greatly influences dewetting[70,72,73,128,129], and although the roughness of the ITO used is just ~6 nm, when compared with the thickness of the Au films deposited, it is relatively high. In the beginning of the thermal dewetting, the formation of holes is similar to what happens for flat surfaces, although it is accelerated by its higher instability caused by high roughness.[128] After a certain time, the surface of the Au thin films begins to not replicate the roughness of the substrate, and the film becomes uneven in thickness, with a higher thickness in pit regions and a lower thickness in protruded regions.[128] Additionally, the holes in the film begin to shrink and their density increases. Increasing t, causes a phenomenon named flattening, that is driven by the topographical features of the substrate, and consists in the retraction of the Au film from pits, leaving behind very small NPs.[128] After a long t, the film becomes flat and nanoporous, and the roughness of the substrate below cannot be noticed.[128] This phenomenon was also demonstrated in the work by Giermann and Thompson [130]. Flattening of the film can clearly be seen in *Figure 3.5*- d) and e) for d_{Au}= 10 and 12.5 nm, T= 500 ºC, and in *Figure 3.5*- j) for d_{Au}= 7.5 nm film, T= 350 ºC, which indicates that it also depends on the T, not just the d_{Au}. Even with this phenomenon happening, NPs can still form in flatter spots of the substrate, as seen in *Figure 3.5*- e). For lower d_{Au} values, flattening does not happen, which is attributed to the fact that these lower thicknesses do not reach the percolation limit for the substrate roughness.[128] Furthermore, it can be inferred that for substrates with a relatively high roughness, thermal dewetting of Au thin films only forms individual NPs if the film is below the percolation limit for that substrate, and there is enough thermal energy. It is important to notice that, for the thermal annealing at 500 ºC, for d_{Au}= 7.5 nm, there is a slight flattening in certain spots of the sample, which is more noticeable for the 4 h annealing, seen in *Figure A.2.1*- h). However, for most of the sample area, NPs were formed, so it was considered that for this sample, the percolation limit was not exceeded.

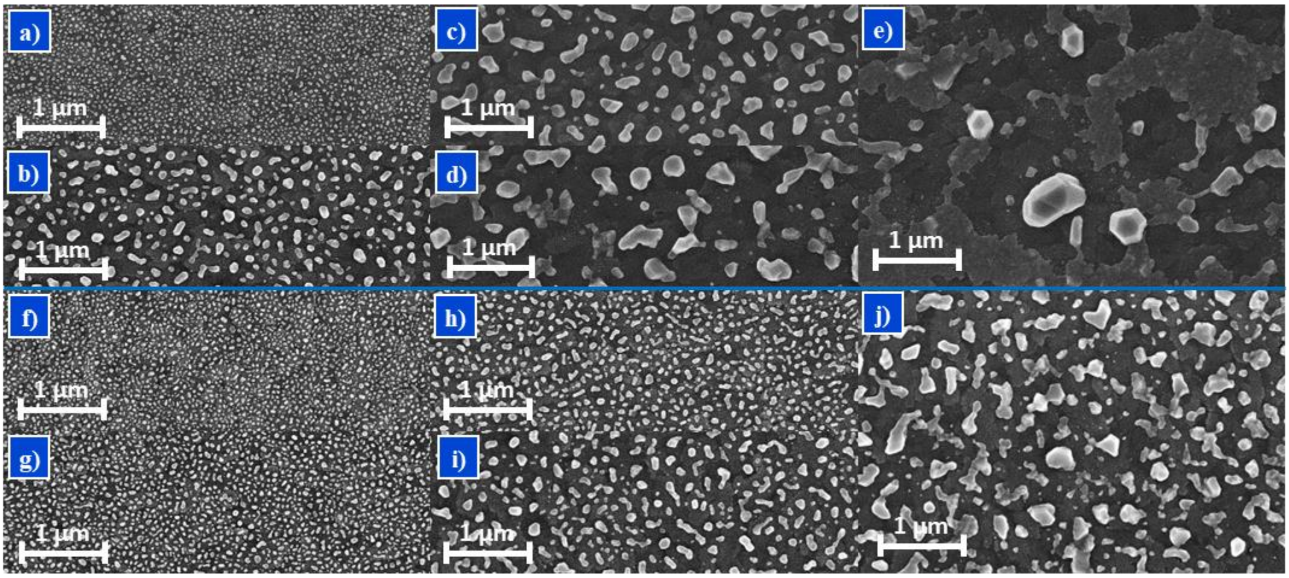

Figure 3.5- SEM images of the obtained Au NPs on ITO after thermal dewetting at 500 ºC, for 2 h, for d_{Au}= a) 2.5, b) 5, c) 7.5, d) 10, and e) 12.5 nm, and at 350 ºC for 2 h, for d_{Au}= a) 2.5, b) 3, c) 4, d) 5, and e) 7.5 nm.

In order to assess the visual appearance of the as-deposited Au thin films, SEM images were taken of bare ITO, and ITO with d_{Au}= 5 and 10 nm, presented in *Figure A.2.3*- a) to c) respectively. It was observed that the 5 nm thick Au film translates the roughness of the ITO below, but it is not continuous, meaning that it is below the percolation limit, and with enough energy it will dewett into singular NPs, as seen previously. However, the 10 nm thick Au film is not fully recreating the roughness of the ITO below, it has some Au agglomerates, and it is a continuous film, meaning that it is above the percolation limit, and it will flatten during thermal dewetting, as demonstrated. Therefore, it is confirmed that flattening happens for Au thin films above the percolation limit, and it can be determined that, for the formation of NPs, the maximum d_{Au} for T=500 and 350 ºC is around 10 and 7.5 nm, respectively. For Au thin films above the percolation limit, the as-deposited thin film appears homogenous, however, this is probably not true, which is caused by a shadowing effect of "inclined" grains during deposition, leading to film thickness variations in the vicinity, that can be aggravated by variations in roughness and in grain orientation.[128]

The NPs obtained from the thermal dewetting processes were analysed using the ImageJ software, and the following parameters were determined: NPs' r, circularity, a, and SC. For this analysis, NPs smaller than 20 nm were not considered, because they blend with the image's noise, making their measurement very imprecise. In addition, samples where the Au film was flattening were not analysed, since they did not present a random array of NPs. For each combination of conditions, two SEM images were analysed to obtain more statistically accurate results. *Table 3.2* shows the results from the analysis of the SEM images of the NPs obtained from the 2-hour thermal annealing processes, for 350 and 500 ºC, for the different studied d_{Au} values. The full analysis, for the remaining annealing times, is presented in *Table A.2.4*. From *Table 3.2*, there are a few general trends that can be observed. For both T values, an increase in the d_{Au} leads to a higher average NPs' r and a, resulting in a smaller SC, which is in accordance with literature.[70,71] In addition, the standard deviation for the NPs' r and circularity parameters also increases with the increase in the d_{Au}. The higher variation of NPs' r may be caused by a few factors: with the retraction of the Au film from the pits, small NPs are left behind [128], which contributes to this higher value that aggravates as the average NPs' r increases [128]; the roughness of the ITO makes the deposited Au film unstable and not homogenous in thickness, which can lead to areas with more Au than others, resulting in NPs with different size, and this effect becomes more notorious for thicker films [128], as seen when comparing *Figure 3.5*- h) and i), for example. The higher variation in the circularity of the NPs, with the increase in d_{Au}, can be explained by the higher variation in the NPs' r- larger NPs need more energy to become round, so smaller NPs will generally be more circular, for the same T. Thus, it can be concluded that, for the same t and d_{Au}, an increase in T leads to rounder NPs.[71] The roughness of the substrate may also be preventing the NPs from becoming more circular. For both T values, when comparing the obtained NPs for t= 2, 4 and 6 h, for the same d_{Au}, in *Table A.2.4*, it can be concluded that there is not a significant difference between them, meaning that a 2-hour annealing is enough for the NPs to stabilize. From the FDTD numerical simulations, it was concluded that the optimum NPs array's geometrical properties were r= 80 nm, a= 150 nm, SC= 20.92 %. From *Table 3.2*, the NPs obtained that were closer to meet these parameters came from the dewetting at 500 ºC for 2 h, for d_{Au}= 7.5 nm, and their parameters are r= 66 nm, a= 110 nm, SC= 23.4 %, with a circularity of 0.77. From the FDTD optical simulations, assuming that the Au NPs would be perfectly round and with a constant a, encapsulated in 10 nm of TiO_2 and implemented in an ultrathin CIGS BFSC, the expected approximate $\Delta J_{SC,Overall}$ value is 1.02 mA/cm^2, which is still far from the value for the optimum geometrical parameters- 1.87 mA/cm^2- but would still present an increase in the solar cell's performance. In order to meet the desired parameters, an increase in the d_{Au} is needed to increase the NPs' r and a, but that will surpass the percolation limit and the film will just flatten. Furthermore, a decrease in ITO's roughness is needed so that the flattening threshold shifts to thicker films.

Table 3.2- Results from the analysis of the SEM images of the NPs obtained after thermal dewetting at 350 and 500 ºC, for 2 h, for the different d_{Au} values studied. ImageJ software was used to analyse the NPs.

T (ºC)	d_{Au} (nm)	r (nm)		Circularity		a (nm)	SC (%)
		Average	Std. Dev.	Average	Std. Dev.	Average	Average
350	2.5	18	5	0.55	0.13	26	27.0
	3	21	6	0.69	0.14	32	26.0
	4	29	11	0.67	0.15	45	25.4
	5	44	20	0.68	0.16	67	25.6
500	2.5	17	4	0.72	0.13	27	25.1
	5	41	19	0.72	0.18	65	24.6
	7.5	66	39	0.77	0.20	110	23.4

To study how the annealing conditions were affecting ITO's electrical and chemical properties, the R_S was measured and the SFE was calculated for each reference sample, that corresponds to an annealing temperature and time. The R_S measurements are displayed in *Table 3.3*, and the reference corresponds to an ITO substrate that was not annealed. It can be concluded, from *Table 3.3*, that the annealing at 500 ºC significantly degrades ITO's electrical properties, but the annealing at 350 ºC for 2 h only shows a slight increase in the R_S, hinting that there might be a lower temperature that does not degrade ITO. However, a decrease in T leads to less round NPs and to a decrease in the maximum d_{Au} before flattening starts to happen. This means that the obtained NPs will have a smaller maximum size, and since the objective is to obtain spherical NPs with r= 80 nm, and the maximum average r obtained was 66 nm, it is not ideal to reduce the T. Furthermore, a solution is needed to prevent ITO's R_S from rising with the annealing. For the 350 ºC annealing, the R_S increases with the t, however, for the 500 ºC annealing, this increase was much less significant. This phenomenon is explained in the work by Kim et al. [131], where it was demonstrated that ITO's resistivity increases faster in the beginning of the annealing and then stabilizes after a certain time, and for a higher T, the initial increase in resistivity is much more abrupt. This means that, for the 2 h annealing, ITO's R_S is already near the stabilizing zone for the 500 ºC annealing, which is not true for the 350 ºC annealing, as seen in *Table 3.3*. It is also important to mention that for most samples annealed at 500 ºC, the ITO seemed to change colour, from an almost transparent light green to a translucid light brown, which is also an indication that some phenomenon is happening that changes ITO's properties. SFE measurements are displayed in *Table A.2.5*, and it was concluded that the annealing does not affect ITO's surface chemical properties.

Table 3.3- Sheet resistance for bare ITO samples, annealed at 350 and 500 ºC, for 2, 4, and 6 h, using the 4-point probe method.

	Sheet Resistance (Ω/sqr)			
Annealing Temperature (°C)/ Time (h)	2	4	6	Reference
350	6.3	17.7	22.1	3.9
500	18.4	20.9	19.4	

3.2.2 – Study of ITO's Electrical Degradation

To study the increase in ITO's R_S following the thermal annealing, three thermal annealing processes were performed for ITO samples, for T= 250, 350 and 500 ºC, t= 2 h. The R_S was then measured, and the results are present in *Table 3.4*. A transition point can be observed at around 250 ºC, at which the R_S starts to increase. In the work by Kim et al. [131], it was concluded that below 200 ºC, ITO's R_S was not affected, between 200 and 250 ºC it started to slowly go up, and after 250 ºC the degradation sharply increases, which corroborates the obtained results.

Table 3.4- Sheet resistance for bare ITO samples, annealed at 250, 350 and 500 ºC, for 2 h, using the 4-point probe method.

T (°C)	Sheet Resistance (Ω/sq)	
	Average	Std. deviation
Reference	3.87	0.02
250	3.98	0.03
350	7.5	0.4
500	20.1	1.0

The increase in ITO's R_S with the thermal annealing may be caused by a change in its crystalline phase [132], or by O_2 diffusion from the atmosphere during the process.[131,133,134] A structural analysis was done on the annealed samples with XRD analysis, to check if there was formation of different crystalline phases during annealing, and the results are presented in *Figure 3.6*- a). It can be concluded that the increase in ITO's R_S is not due to the formation of other crystalline phases, since all the peaks are the same for all the T values, corresponding to the typical peaks seen for ITO.[135] A UV-Vis analysis was performed for the three samples to check if there were changes in their optical properties. The transmittance spectra for the ITO samples annealed at 250, 350 and 500 ºC are presented in *Figure 3.6*- b). It can be observed that an increase in T results in an increase in the transmittance spectra, especially in the IR zone, but also in a redshift. This behaviour can be seen in a few studies, where the O_2 pressure during deposition was varied [131,134,136,137], and in the same study by Kim et al.[131], where it was concluded that the O_2 diffuses from the air during annealing, and that its concentration was higher for thermally degraded ITO films and increases with t, which indicates that it is the cause for the increase in R_S. The O_2 content in ITO's crystalline network greatly influences the density of free carries, which corresponds to the concentration of O_2 vacancies. With the diffusion of O_2 into the network, the concentration of O_2 vacancies decreases, resulting in the decrease of density of free carriers and the absorption coefficient.[138] As a consequence, the transmittance will increase, especially in the IR region where the carriers absorb more predominantly [133], which can be seen in *Figure 3.6*- b), but the R_S will also increase. Kim et al.[131] concluded that the increase in ITO's resistivity is due to two main phenomena, that are caused by O_2 diffusion. Till 200 ºC, the carrier concentration gradually decreases, and between 200 ºC and 250 ºC it decays abruptly, while mobility stays approximately constant. Above 250 ºC, there is a steep drop in the carriers' mobility, but it stabilizes at 275 ºC, as well as the carrier concentration. The decrease in carrier concentration is due to the diffusion of O atoms into interstitials and vacancies, and the decrease in carrier mobility is due to O_2 chemisorption into grain boundaries. This behaviour explains all the tendencies seen before, presented in *Table 3.4*, including the transitioning point at around 250 ºC. To prevent the degradation of ITO's electrical properties, the maximum thermal annealing T should be 250 ºC, however, this decrease in T would shift the flattening threshold to lower d_{Au} values, leading to smaller NPs, farther away from the desired size.

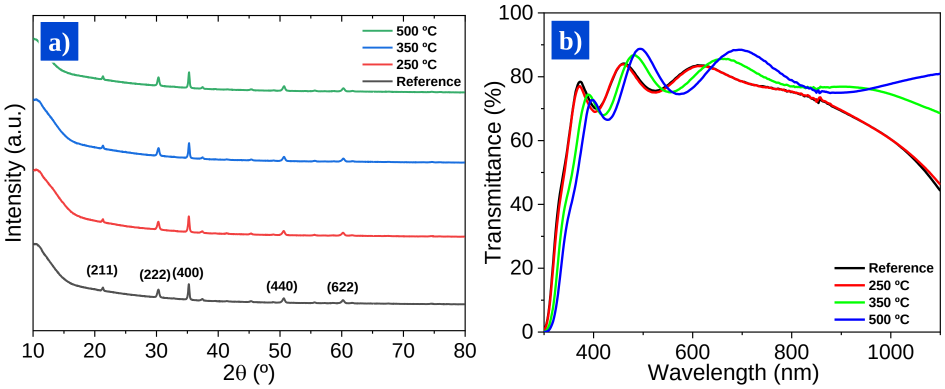

Figure 3.6- a) X-ray diffraction analysis and b) transmittance spectra of bare ITO samples annealed at 250, 350, and 500 ºC.

3.2.3 – Process Optimization- Decreasing ITO's Roughness

The roughness of the substrate greatly affects the NPs obtained from thermal dewetting, as it was explained before. With a decrease in the ITO's roughness, the flattening threshold shifts, allowing thicker films to dewett and form larger and rounder NPs more distant from each other. The objective of this section is to test how the decrease in ITO's roughness impacts the NPs obtained through thermal dewetting.

To decrease its roughness, ITO's surface was etched with two different plasmas, 112 s of C_4F_8, and 112 s of Cl_2, with their respective SEM images in *Figure A.2.6*- a) and b). It was observed that Cl_2 plasma etching did not etch ITO's surface, however, the etching with C_4F_8 plasma reduced the surface roughness. To confirm these visual results, the roughness of these samples was measured with AFM. These measurements are presented in *Table 3.5*, as well as the sample's R_S. It can be concluded that both etch processes reduced ITO's surface roughness by almost 1 nm, but the etch with Cl_2 plasma made the surface more uneven and non-uniform, which is corroborated by a standard deviation of almost 1 nm. There is also the possibility that the processes are also depositing by-products. To test this, cross section SEM images were taken of a reference sample, a sample etched with C_4F_8 plasma, and a sample etched with Cl_2 plasma, and their ITO layer measured 309, 310 and 362 nm, respectively, confirming that there was deposition, probably of a non-conductive Teflon like material. For the Cl_2 plasma, the thickness of this residual layer was considerable, causing the significant increase in R_S. For the C_4F_8 plasma etching sample, the thickness of the ITO layer remained the same and the R_s slightly increased, hinting that there was etching, but also deposition of an ultrathin ASL of a Teflon like material, which can easily be removed. Furthermore, the C_4F_8 plasma etching is the best method to reduce the roughness of ITO's surface.

Table 3.5- Sheet resistance and roughness measurements for ITO samples etched with C_4F_8 and Cl_2 plasma.

Sample	Sheet resistance (Ω/sq)		Roughness (nm)	
	Average	Std. Dev.	Average	Std. Dev.
Reference	3.92	0.02	6.4	0.1
C_4F_8 plasma etch	4.22	0.04	5.4	0.2
Cl_2 plasma etch	8.5	1.0	5.5	0.9

To test how the C_4F_8 plasma etching was affecting ITO's surface chemical properties, and to confirm the deposition during the etching process, the SFE was determined right after the etch process. For the ITO reference sample, it was 74.73 mJ/m^2, and for the ITO sample after the C_4F_8 plasma etch, it was 13.97 mJ/m^2. With the decrease in roughness, it is expected a decrease in the SFE, since the surface area decreases.[139] However, the SFE decrease for the etched sample is very significant, so it cannot be attributed to the decrease in roughness, but instead, it is probably due to the deposition of a thin ASL, as it was theorized before. Only the decrease in roughness is being studied in this section, so, for the upcoming tests with C_4F_8 plasma etched ITO, the thin ASL was removed right after the etching process with a plasma of O_2 and Ar.

To test how the ITO's surface etching with C_4F_8 plasma affects the final properties of the NPs' array, thermal dewetting was made at 350 ºC for 2 h, for d_{Au}= 6 nm. The NPs obtained were analysed and compared with the equivalent non-etched dewetting sample. *Figure 3.7*- a) and b) are SEM images of the unetched and etched samples after thermal dewetting, respectively, and *Table 3.6* shows the results from the ImageJ analysis of the obtained NPs. It can be concluded, by comparing *Figure 3.7*- a) and b), that the C_4F_8 plasma etching of the ITO's surface allows for NPs with a larger *r* and *a*, resulting from the decrease in roughness, which is expected, since this decrease allows the Au film to diffuse more freely and aggregate into larger islands. From Table 3.6, besides the increase in the NPs' average *r* and a, it can also be observed that the NPs become more circular. All in all, the C_4F_8 plasma etching of ITO greatly improved the properties of the obtained NPs and may be a step forward to the optimization of the thermal dewetting process of Au thin films on ITO.

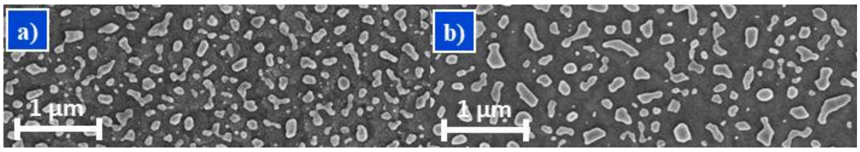

Figure 3.7- SEM images of the NPs obtained after thermal dewetting of a 6 nm Au film, at 350 ºC for 2 h, on a) normal ITO and b) ITO etched with 112 s of C_4F_8 plasma.

Table 3.6- Results from the analysis of the SEM images of the NPs obtained after thermal dewetting at 350 ºC for 2 h, of a 6 nm Au film, on an un-etched ITO sample and an ITO sample etched with 112 s of C_4F_8 plasma. NPs analysed with ImageJ software.

Sample	*r* (nm)		Circularity		*a* (nm)	SC (%)
	Average	Std. dev.	Average	Std. dev.	Average	Average
Unetched	47	27	0.70	0.17	78	23.5
C_4F_8 etching	58	29	0.73	0.16	94	24.1

3.2.4 – Process Optimization- Preventing ITO's Electrical Degradation

The main conclusion from the study from *Section 3.2.2* is that the O_2 diffusion during the thermal annealing process is what is causing the increase in ITO's R_S. Furthermore, a possible solution is to change the annealing atmosphere. Thermal annealing in a N_2 atmosphere was done at 500 ºC for 6 h, which is the maximum *t* studied, for a bare ITO sample and an ITO sample etched with C_4F_8 plasma, to compare their R_S with a bare ITO sample annealed in air. The results are displayed in *Table 3.7*, and it can be concluded that the thermal annealing in a N_2 atmosphere successfully prevented the degradation of ITO's electrical properties.

Table 3.7- Sheet resistance measurements for an ITO sample annealed at 500 ºC for 6 h in air, and for an ITO sample and a C_4F_8 plasma etched ITO sample at 500 ºC for 6 h in an N_2 atmosphere.

Sample	Sheet resistance (Ω/sq)	
	Average	Std. dev.
Reference without annealing	3.87	0.02
Air atmosphere	19.4	0.2
N_2 atmosphere	5.6	0.1
C_4F_8 plasma etched ITO in N_2 atmosphere	5.20	0.08

To test how the different annealing atmosphere influences the obtained NPs, thermal annealing in a N_2 atmosphere was done at 500 ºC for 2 h, for d_{Au}= 4 nm, deposited on ITO and on C_4F_8 plasma etched ITO, and the SEM images of the obtained NPs are displayed in *Figure A.2.7*- a) and b), respectively. For comparison, the same annealing was also done in an air atmosphere for the same d_{Au}, and the SEM image of the obtained NPs are presented in *Figure A.2.7*- c). The analysis of the obtained NPs are displayed in *Table 3.8*. When comparing the SEM images of the NPs obtained from the annealing in air with the ones obtained from the annealing in N_2 atmosphere on un-etched ITO, the NPs from the latter appear to be closer to each other, leading to a higher SC and lower NP's *a*. In addition, the circularity of the NPs obtained in the N_2 atmosphere is also lower. When comparing the two samples annealed in the N_2 atmosphere, it can be observed that the NPs obtained for the C_4F_8 plasma etched ITO are more circular, which is expected considering the previous results from the plasma etched ITO samples.

Table 3.8- Results from the analysis of the SEM images of the NPs obtained after thermal dewetting at 500 ºC for 2 h, of a 4 nm Au film, for an ITO sample in air atmosphere, an ITO sample in N_2 atmosphere, and an ITO sample etched with 112 s of C_4F_8 plasma in N_2 atmosphere. NPs analysed with ImageJ software.

	Sample	*r* (nm)		Circularity		*a* (nm)	SC (%)
		Average	Std. dev.	Average	Std. dev.	Average	Average
Air	Unetched ITO	21	6	0.63	0.15	32	25.2
N_2 atmosphere	Unetched ITO	21	7	0.55	0.17	25	30.7
	C_4F_8 etching	22	5	0.70	0.10	27	29.9

From these results, it can be concluded that even though the thermal annealing in a N_2 atmosphere significantly reduces the degradation of ITO's electrical properties in comparison with annealing in air, the NPs obtained have a lower *a* and are not as circular, which is not ideal. On the other hand, the thermal dewetting in a N_2 atmosphere of the Au film on a C_4F_8 plasma etched ITO, when compared with the non-etched ITO counterpart, resulted in more circular NPs, but the decrease in SC and the increase in the NPs' *r* previously recorded is much less noticeable. Nonetheless, the dewetting in a N_2 atmosphere, generally, results in a higher SC, which is not desirable. All these conclusions reinforce the need for a new calibration study in order to better understand the potential and limitations of the thermal dewetting process in a N_2 atmosphere.

3.3 – Periodic Array of NPs

Through the thermal dewetting process, random arrays of Au NPs were obtained, however, even if the process was fully optimized, it would be impossible to obtain a uniform array of periodic NPs, since variation in their geometrical properties is inherent to the process, meaning that the optical gains would be limited. Therefore, a lithographic process based on NIL that allows the fabrication of a periodic square array of Au NPs was developed and optimized. Initially, the whole process was tested for a larger pattern, with *d*= 400 nm and *p*= 2000 nm, just to have a proof of concept - periodic NPs in a square array. Later, it was changed to the smaller pattern, with *d*= 100 nm and *p*= 600 nm, to further optimize the arrays' geometrical parameters.

The process started with the spin-coating of a 500 nm layer of LOR 5B and a 300 nm layer of TU7, which are the lift-off and patterning resists, respectively, on a Si substrate. The STU-NIL was then performed on the sample, with the *d*= 400 nm and *p*= 2000 nm pattern, and the residual resist layer had to be removed. Different times of O_2 strip were tested- 20, 23, 25 and 27 s- and to be able to visually check the effects of the O_2 strip, a development was made with AZ400K for 7 s. It is important to notice that the O_2 strip process has its own limitations, and at this scale it has some non-uniformity, which will become more apparent for the smaller pattern. In addition, it etches the LOR faster than the TU7, so the control of this step is very important. For the sample with 20 s of O_2 strip, there was no development, meaning that this process time was not enough to remove all the residual layer and reach the LOR. For 23 s of O_2 strip, only some holes were developed, and even then, some holes were more developed than others, which indicates that this process time is still not enough and demonstrates the variability of the process. For 27 s of O_2 strip the LOR was fully developed and the structure fell, indicating that the process etched the residual layer and the LOR underneath. The best O_2 strip time was 25 s, which was enough to reach the LOR and fully open the holes. This is proven by the consistency in the development undercut, seen in the top view and cross section SEM images from *Figure 3.8*-a) and b), respectively. The development can be considered isotropic around the holes, which is desirable. The average hole's size was 464 ± 13 nm, and the average undercut was 446 ± 23 nm. It can be concluded that there was a slight increase in the hole's size, which is probably caused by the O_2 strip, and it is inevitable. In these analyses, the average undercut is considered the average distance between the hole's edge and the development edge. Note that the process to determine the average undercut is done manually, so there is some uncertainty associated. In addition, when taking SEM images, charge can accumulate in the resist and cause it to bend down, slightly increasing holes' area and, consequently, decreasing the measured undercut.

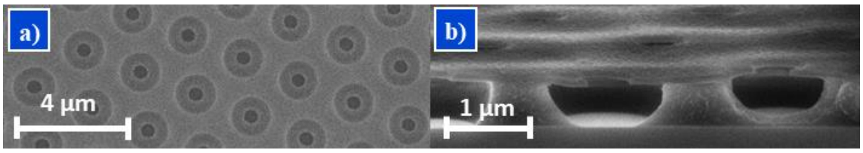

Figure 3.8- a) Top view and b) cross section SEM images of a sample after STU-NIL with a pattern with d= 400 nm and p= 2000 nm, 25 s of O_2 strip, and 7 s development with AZ400K.

Following the 25 s of O_2 strip and the development, 100 nm of Au were deposited by evaporation, and lift-off was made. SEM images were taken of the cross section after the Au deposition, *Figure 3.9*- a), and of the top view of the NDs after the lift-off, *Figure 3.9*- b). From *Figure 3.9*- a), it can be observed that the deposited NDs are not 100 nm thick, but instead approximately half, however, 100 nm are being deposited on top of the TU7. In addition, the average NDs' size was 997 ± 21 nm, which is more than double the average hole's size, meaning that they are depositing below the TU7 and probably on top of the LOR. This is confirmed by *Figure 3.9*- b), where it can be observed that most of the NDs, after lift-off, were either broken, had their edges bent upwards, or were completely removed from the substrate. These NDs are all preferentially bent or broken in one direction, indicating that the Au is not being uniformly deposited around the hole, which is not ideal. Besides this, all the NDs had a hole in the centre, which may be caused by the fact that the stage is rotating during the deposition and is not directly below the source, creating a spot in the middle where less Au is deposited. The hole in the centre of the NDs can favour the formation of more than 1 NP after thermal dewetting, so it is an important issue to tackle.

To test if the deposition setup was what was causing the deposition problems, three samples were prepared using the same methods till the development, and they were placed in three different deposition setups: in the centre and border of the stage with rotation; underneath the Au source without rotation. By varying the placement of the sample during deposition, it was tested if it influences how the Au is being deposited underneath the TU7, and by placing a sample right below the source, it was tested if the angle of deposition was causing the hole in the middle of the NDs. The sample in the centre had unbroken NDs, but only near the edges, and the sample close to the border of the stage had an inconsistent density of NDs, most of them broken in half. The sample below the source had no NDs left. In addition, all the NDs were still hollow in the middle, so this is also a deposition problem that cannot be avoided just by changing the setup. A more detailed analysis of these tests is presented in *Annex A.3*, with the SEM images in *Figure A.3.1*.

It can be concluded that the thermally evaporated Au deposition does not work with the current process parameters. Despite this, as a proof of concept, thermal dewetting was done for the sample placed in the centre of the stage during Au deposition, at 800 ºC for 2 h, and singular periodic NPs were obtained, as seen in *Figure 3.9*- c), however, these NPs are not very uniform nor spherical, so there is room for improvement. Also, some NPs have smaller NPs around them, which may be caused by the discontinuity of some NDs near their edges.

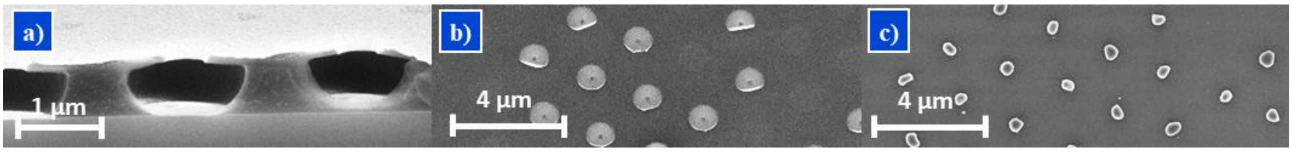

Figure 3.9- a) Cross section SEM image of a sample after depositing 100 nm of Au by evaporation. b) Top view SEM image of a sample after the lift-off. c) SEM image of the NPs obtained after thermal dewetting at 800 ºC for 2 h, for 100 nm of evaporated Au.

To improve the verticality of the Au deposition, the next optimization step was to decrease the LOR's thickness. With a thinner lift-off resist, the Au atoms travel a smaller path to the Si substrate after going through the hole, meaning that there is less room for them to deposit underneath the TU7. LOR 5B has a minimum thickness of around 400 nm when spin-coated, so the lift-off resist was changed to LOR 1A. A calibration was done for this resist, and the chosen thickness was 170 nm, that still allows for the lift-off after the Au deposition. The development of LOR 1A with AZ400K was not uniform between holes within the same sample, so the developer was changed to TMAH 2.2%. The sample fabrication process was done the same as before till the 25 s of O_2 strip, and development tests were conducted for the TMAH 2.2 %, varying the development time- 10, 20, 25, and 30 s- and the undercut was measured. SEM images of the samples developed for 10, 20, and 30 s are presented in *Figure 3.10*- a) to c), respectively. From these images, it can clearly be seen that the increase in development time leads to a larger undercut. In addition, for the 30 s development time, the undercut limits are not as well defined, because there was too much development and the upper structure, TU7, fell, so in these situations, the lift-off is not possible.

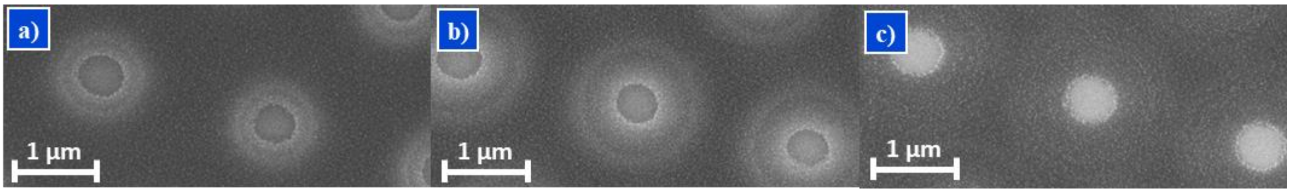

Figure 3.10- SEM images of samples after a) 10, b) 20, and c) 30 s of development with TMAH 2.2 %, for a pattern with d= 400 nm and p= 2000 nm.

The results from the development test are presented in the graph from *Figure 3.11*- a), in which 2 spots were analysed for each sample. For the 30 s of development time, the point diverges from the general tendency because the upper resist structure fell, so it was not considered for the fitting. The chosen development time was 10 s, corresponding to 190 nm of undercut, and reproducibility tests were made for 6 samples, with the results in the graph from *Figure 3.11*- b). In this graph, the average undercut is presented for each sample, with the error bars corresponding to the standard deviation, and the overall average undercut presented as the blue line. For 10 s development time, the average undercut is 173 ± 17 nm for an average hole's diameter of 450 ± 37 nm. Since the LOR's thickness is 170 nm, assuming that the etching is approximately isotropic, there should not be any LOR left on the hole's area. From the reproducibility tests it can be concluded that the whole process is not uniform, with variation in the undercut, however, assuming that the Au deposition will be more vertical, there should not be a considerable variation in the NDs' size.

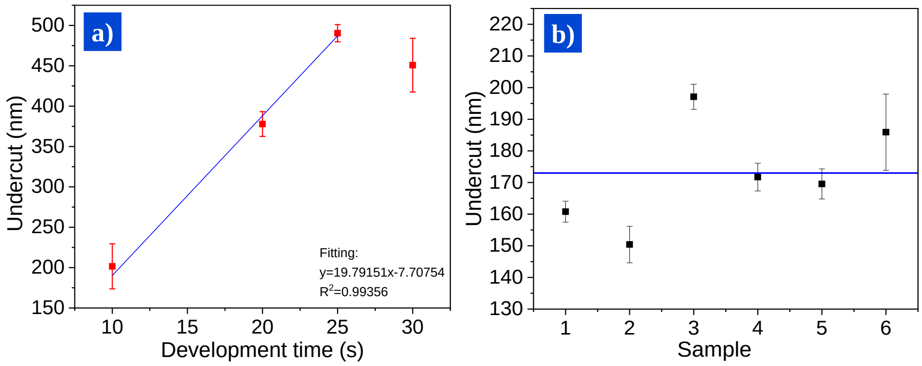

Figure 3.11- a) Graph of undercut vs development time for the development tests with TMAH 2.2 %, for the pattern with d= 400 nm and p= 2000 nm. b) Results from the reproducibility tests for 10 s of development with TMAH 2.2 %, for the same pattern.

Following the 10 s of development with TMAH 2.2%, the Au NDs were deposited. Two deposition methods were tested: PVD by evaporation and by sputtering. The sputtering deposition method was tested to check if it could improve the Au deposition, since deposition by evaporation was not uniform and the deposited NDs had a hole in the middle. For this test, 100 nm of Au were deposited with both deposition methods. Cross-section SEM images of the samples with Au deposited by evaporation and by sputtering are presented in *Figure 3.12*- a) and b), respectively. Top view SEM images for the same samples are presented in *Figure A.3.2*- a) and b), respectively, where it was observed that both Au films deposited have Au grains about the same size, and their visual appearance is similar. For both the deposition methods, the hole in the middle of the NDs that was seen earlier in *Figure 3.9*- b) is not present, which is already an improvement. The cross-section images have clear differences. The decrease in the LOR's thickness significantly improved the deposition of the evaporated Au inside the holes, with the thickness of the NDs now being around 130 nm, instead of 50 nm.

Nonetheless, the deposited NDs have a volcano shape, with its edges deposited on top of the LOR, and with a thickness superior to what was intended, which may be caused by a diffusional physical phenomenon resultant from the Au entering the holes. On the contrary, the Au NDs deposited by sputtering have a pancake shape, with a thickness around 30 nm in the centre that decreases towards the edges. The edges of these NDs are still deposited on top of the LOR, and since they are very thin, they may be broken off during the lift-off process.

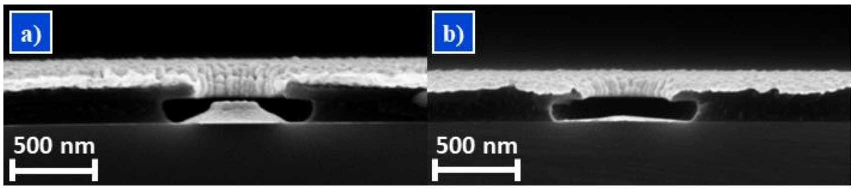

Figure 3.12- Cross section SEM images of samples after deposition of 100 nm of Au by a) evaporation and by b) sputtering.

Lift-off procedure was then done on both samples with sputtered and evaporated Au. The sample with evaporated Au had almost no NDs left after lift-off, confirming that they were deposited on top of the LOR. However, the sample with sputtered Au still had most of the NDs. When the thicker LOR was being used, the NDs deposited by evaporation were being deposited non-uniformly and had a hole in the middle. The thickness of the LOR was decreased and, consequently, the hole in the middle of the NDs disappeared, however, there was too much Au being deposited, leading to NDs with a volcano shape, that is harder to control and may lead to difficult Au NPs’ size calibrations. For these reasons, the Au deposition by evaporation was substituted by the sputtered Au, that deposits NDs with a more uniform shape.

Figure 3.13- a) is a SEM image of the sample with 100 nm of sputtered Au, after the lift-off. It can be observed that almost all NDs deposited by sputtering have their edges broken or slightly bent after lift-off, and are clearly larger than the hole’s size, which is 450 ± 37 nm, meaning that they were deposited underneath the TU7 and on top of the LOR, but despite this, most of them were not removed. This may be caused by the fact that the NDs are thinner and discontinuous near the edges, so instead of bending upwards, breaking, or being completely removed, their discontinuous edges are just torn off or slightly lifted. This phenomenon is almost impossible to avoid, and it will be recurrent throughout the optimization. In contrast with the earlier deposition by evaporation, seen in *Figure 3.9*- b), where only part of the disc was being bent or broken in a preferential direction, indicating an uneven deposition, in the case of the sputtered Au, the NDs are being evenly broken and bent, which indicates that they are being evenly deposited around the centre, which is an improvement.

The next step was to calibrate the size of the obtained NPs after thermal dewetting as a function of the sputtered Au thickness. The deposited Au thicknesses were 10, 15, 20, 25, 50, 75, and 100 nm. After the deposition, lift-off was made for all samples, and they underwent thermal dewetting. The Au NDs, obtained after lift-off, for 10, 25 and 50 nm of sputtered Au are presented in *Figure 3.13*- c) to e), respectively. The SEM images for all the Au thicknesses studied are presented in *Figure A.3.3*. The sample with 50 nm of sputtered Au serves as an example for the samples with 75 nm and 100 nm of sputtered Au, and *Figure 3.13*- b) is a cross section of this sample. It can be observed, from *Figure 3.13*- c) to e), that with the increase in the thickness of the deposited Au, there is a decrease in the discontinuity of the NDs. In addition, the quantity of NDs that are bent also increases, because with an increasing thickness, instead of the edges just breaking during lift-off, they stay attached to the inner part of the ND and bend upwards. The bent edges are more noticeable in the NDs for the 50 nm Au deposition, from *Figure 3.13*- b) and e). It can also be observed that, the discontinuity of the film grows around the centre of the ND, which is caused by its shape, that is thicker in the middle.

The Au NPs, obtained after thermal dewetting, for 10, 25, and 50 nm of sputtered Au are presented in *Figure 3.13*- f) to h), respectively. The SEM images of the NPs for all the studied sputtered Au thicknesses are presented in *Figure A.3.4*. It can be observed that, for the Au thicknesses of 10 to 25 nm, one larger NP forms in the middle and smaller NPs form around it. These smaller NPs are not desirable, because when NPs are too close to each other, their resonance is affected, so even if the middle NP has the desired *r* for the desired resonance, its resonance would not be what was expected. For this reason, the samples that formed more than one NP cannot be used. Nonetheless, it is also observed that, with an increase in the thickness of the deposited Au, from 10 to 25 nm, there was an increase in the r of the middle NP, and the quantity and size of the surrounding NPs decrease. This can be attributed to the decrease of the NDs' discontinuity with the increase in the thickness of the deposited Au. For the Au thickness of 50-100 nm, only one NP was formed, and generally, there is an increase in NPs' r with the increase in the thickness of the deposited Au.

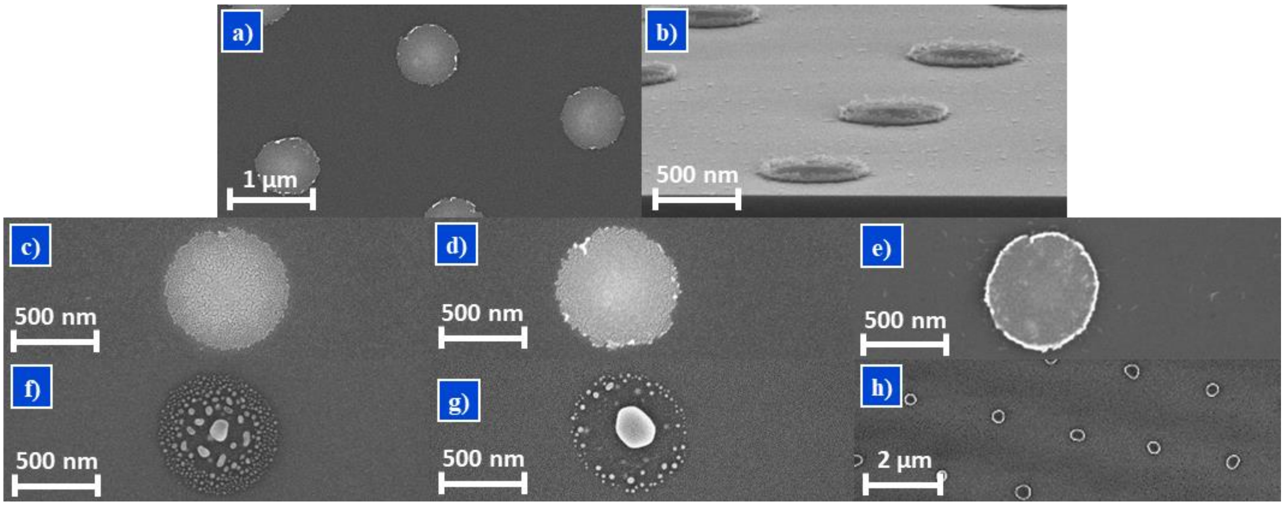

Figure 3.13- Top view SEM images of the Au NDs after lift-off, for a sputtered Au thickness of c) 10, d) 25, e) 50 and a) 100 nm. Top view SEM images of the Au NPs after thermal dewetting at 800 ºC for 2 h, for a sputtered Au thickness of f) 10, g) 25, and h) 50 nm. b) Cross section SEM image of the NDs after lift-off, for a sputtered Au thickness of 50 nm.

The results that correlate the sputtered Au thickness with the final NPs' r, are in the graph from *Figure A.3.5*. It was concluded that the correlation between the deposited Au thickness and the average NPs' r is not linear. From 10 nm to 25 nm of deposited Au, more than one NP is being formed, so the behaviour of the curve in this section is different, and these NPs should not be considered. Between 25 nm and 50 nm of deposited Au thickness, there is a point where only one NP starts to form, but even after this section of the curve, the behaviour is still not close to linear, and the variation of the NPs' r in the same sample is considerable. The development method may be causing a significant variation in this process, mainly because it is done manually, so the time interval that the sample is inside the developer slightly varies from sample to sample. Also, the development time that is being used is only 10 s, meaning that these small variations in the process time have a much larger impact. A variation in the undercut leads to a variation in the NDs' size, that also depends on how much of the ND is deposited on top of the LOR, leading to variation of the obtained NPs. Thus, the next step to improve the reproducibility of this process is to decrease the dilution ratio of the developer, increasing the development time and the control of the process. The average NPs' r for the 50 nm of deposited Au thickness, that is the point where only one NP starts to form, is 153 ± 17 nm, which is still much larger than the intended r, which is 80 nm. Furthermore, a smaller pattern is also needed.

The next optimization steps were to decrease the concentration of the TMAH to 1.5 % V/V, and to change the pattern to a smaller one with a periodic square array with d= 100 nm and p= 600 nm. O_2 strip tests were firstly done, because with the decrease in the size of the pattern, the way that the etching is done on the residual resist layer may vary. Two O_2 strip times were tested- 25 and 27 s- and the 25 s process was not enough to fully open the holes like before, so it was changed to 27 s. The whole sample fabrication process was done exactly the same up until the 27 s O_2 strip, and development tests were made for TMAH 1.5 %, varying the development time- 50, 60, 70, and 80 s- and the results are displayed in the graph from *Figure 3.14*- a), where the development time is correlated with the average undercut, with the error bars showing the standard deviation. The holes' diameter was also measured for all the samples, and the average value is 252 ± 11 nm, which is way larger than the intended diameter, 100 nm. Similar to the larger pattern, the O_2 strip process is enlarging the holes, which is inevitable, but for this smaller pattern, it is much more noticeable. The reason for this is that the residual layer is much more confined, but its thickness is the same as the larger pattern. This means that the O ions that are etching the residual layer are much more likely to also etch the side walls of the holes and widen them. From *Figure 3.14*- a), it can be observed that curve is approximately linear till 70 s of development time and stagnates after that. This can be explained by the fact that, after 70 s of development time, the undercut around the holes is almost joining the four nearby undercuts. In fact, for the 85 s development time, the upper resist, TU7, is almost falling. It is also important to notice that all these analysed samples showed some variation in the undercut, represented by the error bars, which will result in variations in the sputtered NDs and in the final NPs' size. Considering the fitting from *Figure 3.14*- a), and that an undercut of around 130 nm is desirable, the chosen development time was 59 s.

More thorough reproducibility tests were made for 4 samples, for 59 s of development time, and 5 spots were analysed for each sample. The results are displayed in the graph from *Figure 3.14*- b), in which the red dot corresponds to the average undercut for all the analysed holes in each sample, the blue line at 139 ± 13 nm corresponds to the average undercut for all the holes analysed, and the 5 black dots correspond to the average undercut for each analysed spot in the sample. The average undercut for this test is slightly higher than the intended 130 nm, but it is expected because of all the variation in the process. The average holes' size is 276 ± 11 nm, which is also higher than the previously measured value. Between samples, the variation of the average undercut value is relatively small, however, the variation of the average undercut between spots inside the same sample is considerably high. This indicates that, at this scale, the process is starting to lose its reproducibility, with variability in the O_2 strip and development steps, especially within the same sample, which will consequently lead to variability in the NDs' size after the lift-off, and in the final NPs' size.

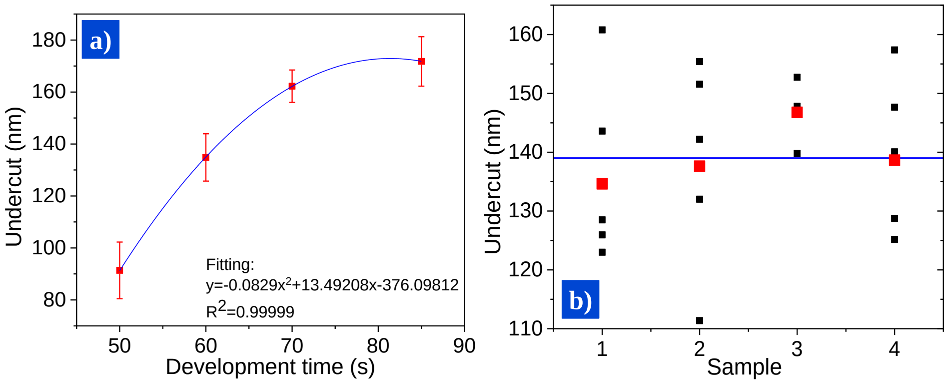

Figure 3.14- a) TMAH 1.5 % development tests and b) reproducibility tests for 59 s, for the pattern with d= 100 nm and p= 600 nm.

Au deposition tests were made for the chosen development time, 59 s, for different sputtered Au thicknesses- 40, 50, 60, 70, 80, and 90 nm- followed by the lift-off. As expected, the variation of the undercut within the same sample lead to a considerable variation in the NDs' size, which can be seen, for example, in *Figure 3.15*- a) and b), that are SEM images of 2 different spots in the same sample, for 70 nm of sputtered Au. In addition, the edges of the NDs are still lifted and bent upwards, and some of them are even broken, which causes even more variability. The reduction in the size of the pattern also caused the NDs to be discontinuous in the middle, again.

The samples were then dewetted at 800 ºC for 2 h, and the obtained NPs were analysed for 5 different spots in each sample, to determine the NPs' *r* and circularity. SEM images of the NPs obtained for 40 and 90 nm of sputtered Au are displayed in *Figure 3.15*- c) and d). SEM images for the remaining sputtered Au thicknesses are presented in Figure A.3.6. The NDs from the samples with 40, Figure 3.15- c), 50 and 60 nm of sputtered Au thickness formed multiple NPs with different sizes, so they were not considered for this analysis. The results for the analysis of the obtained NPs are displayed in *Table 3.9*. The samples with 70 and 80 nm of sputtered Au thickness had some NDs form two NPs in some zones, so only the spots where a single NP was formed were considered. This may be caused by the discontinuity of the ND's centre, promoting the formation of two NPs instead of one. The singular NPs in the sample with 70 nm of sputtered Au thickness had smaller NPs around them that were not measured, but are still affecting the central NP's resonance, and if these smaller NPs had aggregated to the central one during dewetting, it would change the average NPs' *r*. For these reasons, the analysis for this sample is the least accurate of the three, and it was only used to serve as comparison. As a general trend, it can be concluded that, as the sputtered Au thickness increases, so does the average NPs' *r*, as expected, and the corresponding standard deviation. The discontinuity in the centre of the NDs means that the Au is predominantly being deposited around the centre, so a large quantity of Au is deposited on top of the LOR and later broken or bent. With an increase in the thickness of the deposited Au, more Au is being deposited on top of the LOR and broken off, which also depends on the variation of the undercut, and will ultimately cause a higher variation in the final NPs' *r*. This also explains why the increase in the NPs' *r* with the increase in thickness of the deposited Au is so small- part of the additional deposited Au is being broken-off during lift-off. Nonetheless, the circularity of the NPs is uniform between samples, but it is being hindered by the discontinuity of the Au NDs' centre.

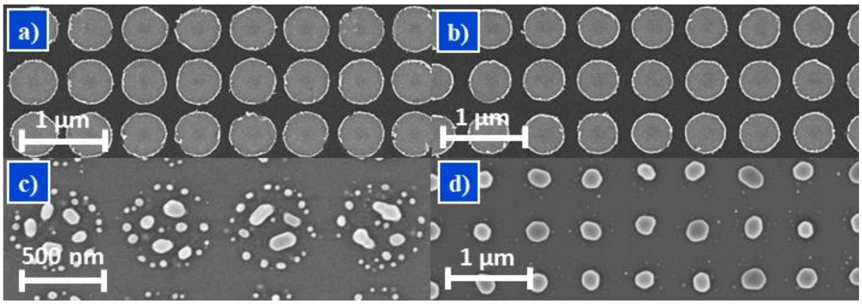

Figure 3.15- a) and b) are SEM images of NDs for two different spots on the same sample after lift-off, for 70 nm of deposited Au. SEM images of the NPs obtained after thermal dewetting at 800 ºC 2h, for the small pattern, for c) 40 and d) 90 nm of deposited Au.

Table 3.9- Results from the analysis of the SEM images for 70, 80 and 90 nm of sputtered Au, for the small pattern with d= 100 nm and p= 600 nm.

Au thickness (nm)	*r* (nm)		Circularity	
	Average	St. deviation	Average	St. deviation
70	109	10	0.89	0.05
80	111	12	0.85	0.04
90	116	15	0.85	0.04

From the FDTD numerical simulations, it was concluded that the optimum NPs array's geometrical properties were *r*= 80 nm, *a*= 150 nm, SC= 20.92 %. The sample that formed singular NPs and that was closer to meet these parameters correspond to a sputtered Au thickness of 80 nm, originating NPs with *r*= 111 nm, *a*= 178 nm, SC= 24.2 %, which are still far from the optimum geometrical parameters' values. To reach the desired NP's *r* and *a*, the process would have to be scaled down even more, and, as it was demonstrated, at this nanometric scale, it loses resolution, affecting reproducibility.

4

CONCLUSIONS AND FUTURE PERSPECTIVES

The objective of this Thesis was to design transparent plasmonic substrates to be implemented in ultrathin CIGS BFSCs, as a rear light management strategy, consisting of periodic Au NPs on ITO encapsulated with a dielectric material that scatter incoming light, increasing the optical path length inside the absorber.

FDTD simulations, for FI and RI, were performed to find the best materials and architecture for the NPs array and passivation layer, that maximize the J_{SC} in ultrathin CIGS BFSCs. The parameters varied were the NPs' r and a, the d_{pass}, and the NPs and passivation materials. For Fi and RI, the NPs' architectures with d_{pass}= 10 nm, generally have a larger maximum J_{SC}, when comparing with architectures with thicker d_{pass} values. Also, when comparing architectures with Au and Ag NPs, for the same encapsulation material and d_{pass}, the Ag NPs architectures originate a larger ΔJ_{SC}. A compromise between FI and RI was made, and the best combinations of materials and parameters were Au NPs with r= 80 nm, a= 150 nm, SC= 20.92 %, d_{pass}= 10 nm of TiO_2, $\Delta J_{SC,Overall}$= 1.87 mA/cm^2, and Ag NPs with the same architecture, with $\Delta J_{SC,Overall}$= 2.24 mA/cm^2. The compromise between FI and RI can be further optimized with a defined application for the solar modules, which allows to determine a more accurate model that better represents the optical phenomena. Further studies with varying angle of light incidence can also improve the optimization of the periodic array of metallic NPs.

Thermal dewetting was studied and optimized to address its feasibility in the fabrication of a random array of Au NPs on ITO substrates with the desired geometrical parameters, by varying the process T, t, and the d_{Au}. It was concluded that, for d_{Au} values above the percolation limit, the Au thin film flattens instead of forming NPs, which is mainly caused by ITO's relatively high roughness. From the dewetting at 500 ºC, t= 2 h, for d_{Au}= 7.5 nm, NPs with r= 66.5 nm, a= 110 nm, SC= 23.4 %, with a circularity of 0.77, were obtained, which are still far from the optimum geometrical parameters. Therefore, ITO's roughness was reduced in approximately 1 nm with a C_4F_8 plasma, resulting in NPs with a higher r, a, and circularity, in comparison to an un-etched sample. It was also observed that ITO's R_s increased with T, which was determined to be caused by O_2 diffusion during annealing, so, the thermal annealing's atmosphere was changed to N_2, which successfully prevented the degradation of ITO's electrical properties. The etching of ITO's surface and the annealing in an N_2 atmosphere may be a step forward to the optimization of the thermal dewetting of Au thin films on ITO.

A lithographic process based on NIL that allows the fabrication of a periodic square array of Au NPs was studied, to obtain a proof of concept. Optimization was done at the different process stages and the final parameters were: pattern with d= 100 nm and p= 400 nm; 170 nm of LOR 1A; 300 nm of TU7; 27 s of O_2 strip after STU-NIL; 59 s of TMAH 1.5 % development. NPs with r= 111 nm, a= 178 nm, SC= 24.2 %, corresponding to d_{Au}= 80 nm, were obtained, which are still far from the optimum geometrical parameters' values. To reach the desired NP's r and a, the process would have to be scaled down even more, and, at this nanometric scale, it starts to lose resolution, affecting reproducibility and leading to a high variation in the NPs size.

Summarizing, an optimized architecture for a periodic square array of metallic NPs to be implemented in an ultrathin CIGS BFSC was determined through optical simulations, and two different approaches were studied to obtain NPs with the desired r. Many optimizations were done throughout the experimental sections of this Thesis to overcome the detected process issues, and a proof of concept was obtained. Nonetheless, there are still improvements that need to be made in order to obtain NPs with the optimum architecture - thermal dewetting on ITO in an N_2 atmosphere needs to be thoroughly studied, and there is also the need for innovative new approaches for the lithographic process, in order to overcome process limits and obtain smaller NPs. The work done in this Thesis shows great potential and it is the first step for the implementation of plasmonic NPs in ultrathin CIGS BFSC, and for this technology to be competitive in the PV market.

BIBLIOGRAPHY

1. M. A. Islam et al., *Energy for Sustainable Development*, 2020, 105-123.
2. A. Qazi et al., *IEEE Access*, 2019, **7**, 63837 – 63851.
3. D. Gielen et al., *Energy Strategy Reviews*, 2019, **24**, 38-50.
4. F. Martins et al., *Energies (Basel)*, 2019, **12**, 964.
5. A. J. N. Oliveira et al., *Adv. Photonics Res.*, 2022, **3**, 2100190.
6. M. Schmid, *Semicond. Sci. Technol.*, 2017, **32**, 043003.
7. T. D. Lee & A. U. Ebong, *Renewable and Sustainable Energy Reviews*, 2017, **70**, 1286–1297.
8. M. Nakamura et al., *IEEE J. Photovolt.*, 2019, **9**, 1863-1867.
9. N. Mufti et al., *Solar Energy*, 2020, **207**, 1146-1157.
10. B. Barman & P. K. Kalita, *Solar Energy*, 2021, **216**, 329-337.
11. L. M. Mansfield et al., *Progress in Photovoltaics*, 2018, **26**, 949-954.
12. M. J. Shin et al., *Appl. Surf. Sci.*, 2021, **535**, 147732.
13. N. Cavallari et al., *Appl. Surf. Sci.*, 2017, **412**, 52-57.
14. M. J. Shin et al., *Nano Energy*, 2021, **82**, 105729.
15. M. Mazzer et al., *Solar Energy Materials and Solar Cells*, 2017, **166**, 247-253.
16. ZSW & HZB, *CIGS White Paper*, 2019.
17. J. Lindahl et al., *IEEE J. Photovolt.*, 2013, **3**, 1100-1105.
18. R. Carron et al., *Sci. Technol. Adv. Mater.*, 2018, **19**, 396-410.
19. J. Ramanujam et al., *Prog. Mater. Sci.*, 2020, **110**, 100619.
20. G. Harper, *Encyclopedia Britannica*, https://www.britannica.com/technology/electrical-and-electronics-engineering, 2016, (accessed 10 September 2023)
21. Y. C. Wang et al., *Mater. Chem. Phys.*, 2019, **234**, 329-344.
22. K. Yoshikawa et al., *Solar Energy Materials and Solar Cells*, 2017, **173**, 37-42.
23. V. Bermudez & A. Perez-Rodriguez, *Nat. Energy*, 2018, **3**, 466-475.
24. A. Chirilã et al., *Nat. Mater.*, 2011, **10**, 857-861.
25. K. Decock et al., *Energy Procedia*, 2010, **2**, 49-54.
26. B. Misic et al., *IEEE J. Photovolt.*, 2015, **5**, 1179-1187.
27. Z. A. Wang et al., *Solid State Electron*, 2009, **53**, 1149-1153.
28. W. Shockley & H. J. Queisser, *J. Appl. Phys.*, 2004, **32**, 510–519.
29. J. Ramanujam & U. P. Singh, *Energy Environ. Sci.*, 2017, **10**, 1306–1319.
30. E. Ribeiro, Development of nanofabrication processes for light management strategies in ultrathin CIGS solar cells, Masters Dissertation, Universidade de Aveiro, 2023.
31. J. Goffard et al., *IEEE J. Photovolt.*, 2017, **7**, 1433–1441.
32. J. Krc et al., *Thin Solid Films*, 2017, **633**, 193–201.
33. A. J. N. Oliveira et al., *Physics, Simulation, and Photonic Engineering of Photovoltaic Devices X*, 2021, **11681**, 1168108.
34. Y. Li et al., *ACS Appl. Energy. Mater.*, 2022, **5**, 7, 7956–7964.
35. F. J. Haug & C. Ballif, *Energy Environ. Sci.*, 2015, **8**, 824–837.
36. J. Liu et al., *J. Mater. Chem. C Mater.*, 2019, **7**, 3121–3145.
37. I. Massiot et al., *Nat. Energy*, 2020, **5**, 959–972.
38. C. Chen et al., *Chem. Soc. Rev.*, 2021, **50**, 7250–7329.
39. R. Alexandre, Development of Nanoimprint Lithography Processes for State-of-the-art Light Management Strategies to be Integrated in CIGS Solar Cells, Masters Dissertation, Nova School of Science and Technology, 2022.
40. M. J. Shin et al., *Nano Energy*, 2022, **92**, 106711.
41. Y. Li et al., *Solar Energy Materials and Solar Cells*, 2022, **234**, 111431.
42. D. Kim et al., *Adv. Funct. Mater.*, 2020, **30**, 2001775.
43. S. C. Yang et al., *Nat. Energy*, 2023, **8**, 40–51.
44. P. Jackson et al., *physica status solidi (RRL) – Rapid Research Letters*, 2016, **10**, 583–586.
45. P. M. P. Salomé et al., *Solar Energy Materials and Solar Cells*, 2014, **123**, 166–170.
46. D. Fraga et al., *Int. J. Appl. Ceram. Technol.*, 2015, **12**, 728–737.
47. K. H. Ong et al., *International Journal of Photoenergy*, 2018, **2018**, 1–14.
48. G. Yin et al., *Solar Energy Materials and Solar Cells*, 2019, **195**, 318–322.
49. J. K. Larsen et al., *Appl. Phys. Lett.*, 2014, **104**, 033901.
50. L. Gouillart et al., *Thin Solid Films*, 2019, **672**, 1–6.
51. S. C. Yang et al., *Solar RRL*, 2021, **5**, 2100108.
52. L. Gouillart et al., *Progress in Photovoltaics: Research and Applications*, 2021, **29**, 212–221.
53. F. Mollica et al., *Thin Solid Films*, 2017, **633**, 202–207.
54. G. Yin et al., *Solar Energy Materials and Solar Cells*, 2016, **153**, 124–130.
55. P. M. P. Salomé et al., *Adv. Mater. Interfaces*, 2018, **5**, 1701101.
56. V. Amendola et al., *Journal of Physics: Condensed Matter*, 2017, **29**, 203002.
57. M. A. Garcia, *J. Phys. D Appl. Phys.*, 2011, **44**, 283001.
58. H. A. Atwater & A. Polman, *Nat Mater*, 2010, **9**, 205–213.
59. S. Morawiec et al., *Opt. Express*, 2014, **22**, A1059.
60. M. J. Mendes et al., *Nanoscale*, 2014, **6**, 4796–4805.
61. A. J. N. Oliveira et al., *Solar RRL*, 2020, **4**, 2000310.
62. G. Yin et al., *Appl. Surf. Sci.*, 2015, **355**, 800–804.
63. T. S. Lopes et al., *IEEE J. Photovolt*, 2019, **9**, 1421–1427.
64. S. M. S. Hasheminassab et al., *Plasmonics*, 2021, **16**, 273–282.
65. Y. C. Lin & X. C. Wei et al., *Chinese Journal of Physics*, 2017, **55**, 1219–1224.
66. M. J. Jeng et al., *Materials*, 2015, **8**, 6761–6771.
67. C. Cherqui et al., *Acc. Chem. Res.*, 2019, **52**, 2548–2558 (2019).
68. K. Okamoto et al., *Journal of Photochemistry and Photobiology C: Photochemistry Reviews*, 2017, **32**, 58–77.
69. N. J. Ray et al., *ACS Appl. Nano Mater.*, 2021, **4**, 2733–2742.
70. F. Leroy et al., *Surf. Sci. Rep.*, 2016, **71**, 391–409.

71. N. J. Ray et al., *ACS Appl. Nano Mater.*, 2019, **2**, 4395–4401.
72. F. Ruffino & M. G. Grimaldi, *physica status solidi (a)*, 2015, **212**, 1662–1684.
73. A. L. Giermann & C. V. Thompson, *Appl. Phys. Lett.*, 2005, **86**, 121903.
74. M. Topič et al., *Solar Energy Materials and Solar Cells*, 2015, **135**, 57–66.
75. S. Royanian et al., *Plasmonics*, 2020, **15**, 1173–1182.
76. P. Zarerasouli et al., *Opt. Mater. (Amst.)*, 2022, **131**, 112729.
77. D. Ramos, Development and optimization of a replicable process to produce light trapping substrates for ultrathin CIGS solar cells, Masters Dissertation, Nova School of Science and Technology, 2021.
78. A. Jangjoy & S. Matloub, *Solar Energy*, 2022, **242**, 10–19.
79. D. Zheng et al., *Nano Energy*, 2022, **94**, 106934.
80. S. Shahin et al., *Appl. Phys. Lett.*, 2012, **101**, 053109.
81. J. Wang et al., *The Journal of Physical Chemistry C*, 2013, **117**, 85–91.
82. S. K. Agnihotri et al., *Opt. Mater. (Amst.)*, 2022, **134**, 113129.
83. E. A. Dawi et al., *Nanoscale Res. Lett.*, 2021, **16**, 149.
84. M. J. Mendes et al., *Nano Energy*, 2016, **26**, 286–296.
85. Ansys Lumerical FDTD, https://www.ansys.com/products/photonics/fdtd (accessed 15 September 2023).
86. M. Rubin, *Solar Energy Materials*, 1985, **12**, 275–288.
87. H. Fujiwara & M. Kondo, *Phys. Rev. B*, 2005, **71**, 75109.
88. T. Hara et al., *Phys. Rev. Appl.*, 2014, **2**, 34012.
89. G. Birant et al., *Applied Sciences*, 2019, **9**, 677.
90. S. Choi et al., *Thin Solid Films*, 2018, **665**, 91–95.
91. S. Bose et al., *Thin Solid Films*, 2019, **671**, 77–84.
92. G. Birant et al., *EPJ Photovoltaics*, 2020, **11**, 10.
93. S. Bose et al., *Solar RRL*, 2018, **2**, 1800212.
94. G. S. Park et al., *Adv. Energy Mater.*, 2023, **13**, 2203183.
95. P. B. Johnson & R. W. Christy, *Phys. Rev. B*, 1972, **6**, 4370–4379.
96. Refractive Index of TiO2, Filmetrics, https://www.filmetrics.com/refractive-index-database/TiO2+-+Amorphous/Titanium-Dioxide, (accessed 15 September 2023).
97. A. Julien et al., *Opt. Express*, 2020, **28**, 37487.
98. U. A. Yusufoglu et al., *Energy Procedia*, 2014, **55**, 389–395.
99. C. E. Valdivia et al., *2017 IEEE 44th Photovoltaic Specialist Conference (PVSC)*, 2017, 1094–1099.
100. Mie scattering (FDTD), Ansys, https://optics.ansys.com/hc/en-us/articles/360042703433, (accessed 10 September 2023)
101. MSE PRO 1.1 mm 3~5 Ohm/Sq ITO Coated Glass Substrate, *MSE Supplies*, https://www.msesupplies.com/products/mse-pro-1-1-mm-3-5-ohm-sq-ito-coated-glass-substrate?variant=33749136463, (accessed 10 September 2023)
102. D. K. Owens & R. C. Wendt, *J. Appl. Polym. Sci.*, 1969, **13**, 1741–1747.
103. D. H. Kaelble, *J. Adhes.*, 1970, **2**, 66–81.
104. SSS-NCH, NANOSENSORS, https://www.nanosensors.com/supersharpsilicon-non-contact-tapping-mode-high-resonance-frequency-afm-tip-SSS-NCH, (accessed 10 September 2023)
105. M. A. Alkhalayfeh et al., *Renewable and Sustainable Energy Reviews*, 2021, **141**, 110726.
106. M. Lismont & L. Dreesen, *Materials Science and Engineering: C*, 2012, **32**, 1437–1442.
107. Q. Han et al., *Sens. Actuators. B Chem.*, 2016, **231**, 609–614.
108. S. A. Maier, *Plasmonics: Fundamentals and Applications*, 2007.
109. U. Kreibig & M. Vollmer, *Optical Properties of Metal Clusters*, 1995, **25**.
110. L. Cheng et al., *Mater. Res. Express*, 2020, **7**, 125009.
111. C. F. Bohren & D. R. Huffman, *Absorption and Scattering of Light by Small Particles*, 1998.
112. P. K. Jain et al., *J. Phys. Chem. B*, 2006, **110**, 7238–7248.
113. K. Khurana & N. Jaggi, *Plasmonics*, 2021, **16**, 981–999.
114. P. N. Njoki et al., *The Journal of Physical Chemistry C*, 2007, **111**, 14664–14669.
115. G. Y. Yao et al., *Catalysts*, 2018, **8**, 236.
116. A. R. Shafiqa et al., *J. Phys. Conf. Ser.*, 2018, **1083**, 012040.
117. A. O. Govorov et al., *Nanoscale Res. Lett.*, 2006, **1**, 84.
118. A. Poletti et al., *Nanoscale*, 2015, **7**, 13702–13714.
119. A. O. Govorov & H. H. Richardson, *Nano Today*, 2007, **2**, 30–38.
120. S. K. Ghosh & T. Pal, *Chem. Rev.*, 2007, **107**, 4797–4862.
121. N. Zohar et al., *Journal of Photochemistry and Photobiology C: Photochemistry Reviews*, 2014, **21**, 26–39.
122. M. A. García et al., *Chem. Phys. Lett.*, 1999, **315**, 313–320.
123. M. Quinten & U. Kreibig, *Surf. Sci.*, 1986, **172**, 557–577.
124. S. L. Westcott et al., *Chem. Phys. Lett.*, 1999, **300**, 651–655.
125. X. Huang et al., *Chem. Soc. Rev.*, 2013, **42**, 173–201.
126. M. Alexandre et al., *ACS Appl. Energy. Mater.*, 2019, **2**, 2930–2938.
127. F. J. Ostos et al., *Polymers (Basel)*, 2020, **12**, 2898.
128. A. Sharipova et al., *Acta. Mater.*, 2022, **231**, 117919.
129. P. D. Nsimama et al., *Appl. Surf. Sci.*, 2016, **388**, 475–482.
130. A. L. Giermann & C. V. Thompson, *J. Appl. Phys.*, 2011, **109**, 083520.
131. Y. N. Kim et al., *J. Mater. Res.*, 2005, **20**, 1574–1579.
132. J, Xu et al., *Mater. Sci. Semicond. Process.*, 2014, **21**, 104–110.
133. M. Bender et al., *Thin Solid Films*, 1998, **326**, 72–77.
134. M. Marikkannan et al., *AIP Adv.*, 2015, **5**, 017128.
135. N. Vieira et al., *Materials Research*, 2013, **16**, 1156–1160.
136. H. Kim et al., *J. Appl. Phys.*, 1999, **86**, 6451–6461.
137. N. M. Ahmed et al., *Results Phys.*, 2019, **13**, 102159.
138. N. G. Elfadill et al., *Journal of Materials Science: Materials in Electronics*, 2014, **25**, 262–266.
139. Y. Gao et al., *Transp. Res. Rec.*, 2023, OnlineFirst.

A

APPENDIX

A.1 FDTD Optical Simulations- Parameter sweeps

Figure A.1.1 is a representation of the scattering effect of metallic NPs implemented at the Mo/CIGS interface of a conventional ultrathin CIGS solar cell. Figure A.1.2 is the FDTD optical simulations setup for the resonance study on a NP in a periodic array. The simulated ΔJ_{SC} colour maps for FI and RI, as a function of NPs' radius and interdistance, for all the studied material combinations, and for 10, 15 and 20 nm of passivation thickness, are presented: Figure A.1.3 corresponds to the ΔJ_{SC} colour maps for Au NPs encapsulated with Al_2O_3; Figure A.1.4 to Au NPs encapsulated with HfO_2; Figure A.1.5 to Au NPs encapsulated with TiO_2 for RI; Figure A.1.6 to Ag NPs encapsulated with SiO_2; Figure A.1.7 to Ag NPs encapsulated with Al_2O_3; Figure A.1.8 to Ag NPs encapsulated with HfO_2; Figure A.1.9 to Ag NPs encapsulated with TiO_2. The best geometrical parameters for all the studied material combinations, for 10, 15 and 20 nm of passivation thickness, are presented in Table A.1.10 for FI and RI, and in Table A.1.11 for a compromise between both illuminations, using the established FoM. In Figure A.1.12, the simulated and theoretical Mie scattering and absorption efficiency spectra for 1 Au NP with r= 80 nm, in a medium with n= 1, for a mesh size of 0.4 and 1.5 nm, are displayed.

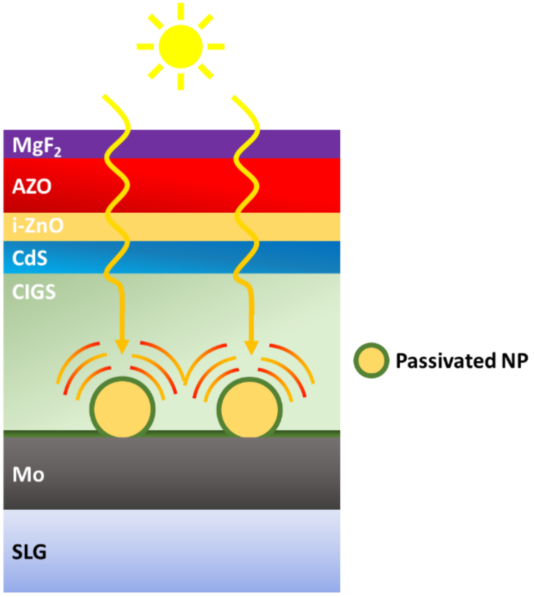

Figure A.1.1- Representation of the scattering effect of metallic NPs implemented at the Mo/CIGS interface of a conventional ultrathin CIGS solar cell.

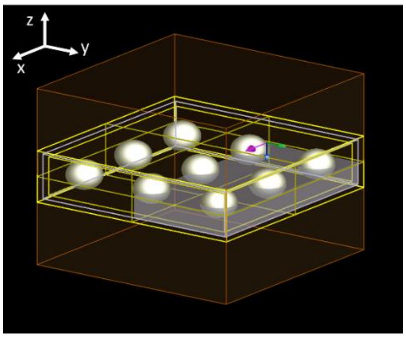

Figure A.1.2- FDTD optical simulations setup for the resonance study of a NP in a periodic square array.

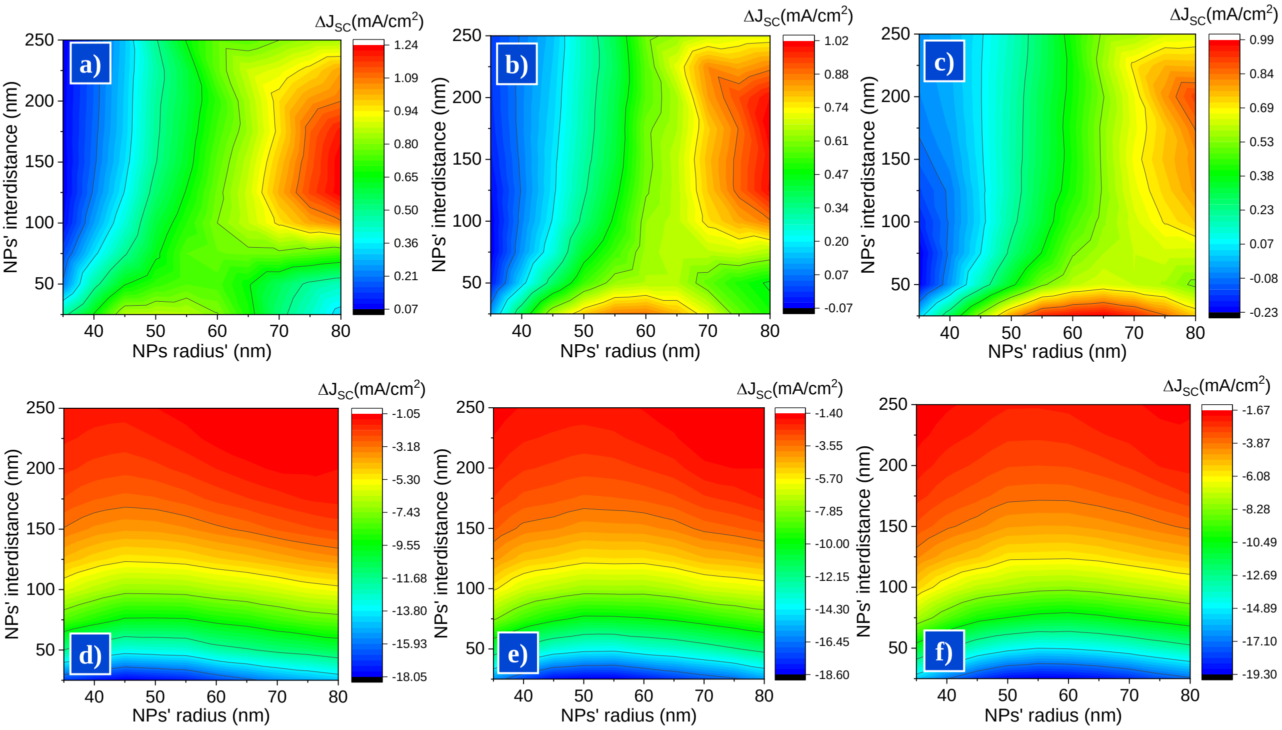

Figure A.1.3- Simulated ΔJ_{SC} colour maps for Au NPs passivated with Al_2O_3 integrated in an ultrathin CIGS BFSC: for a) 10, b) 15, and c) 20 nm of passivation thickness for FI; for d) 10, e) 15, and f) 20 nm of passivation thickness for RI. Note that the scale is different for each map.

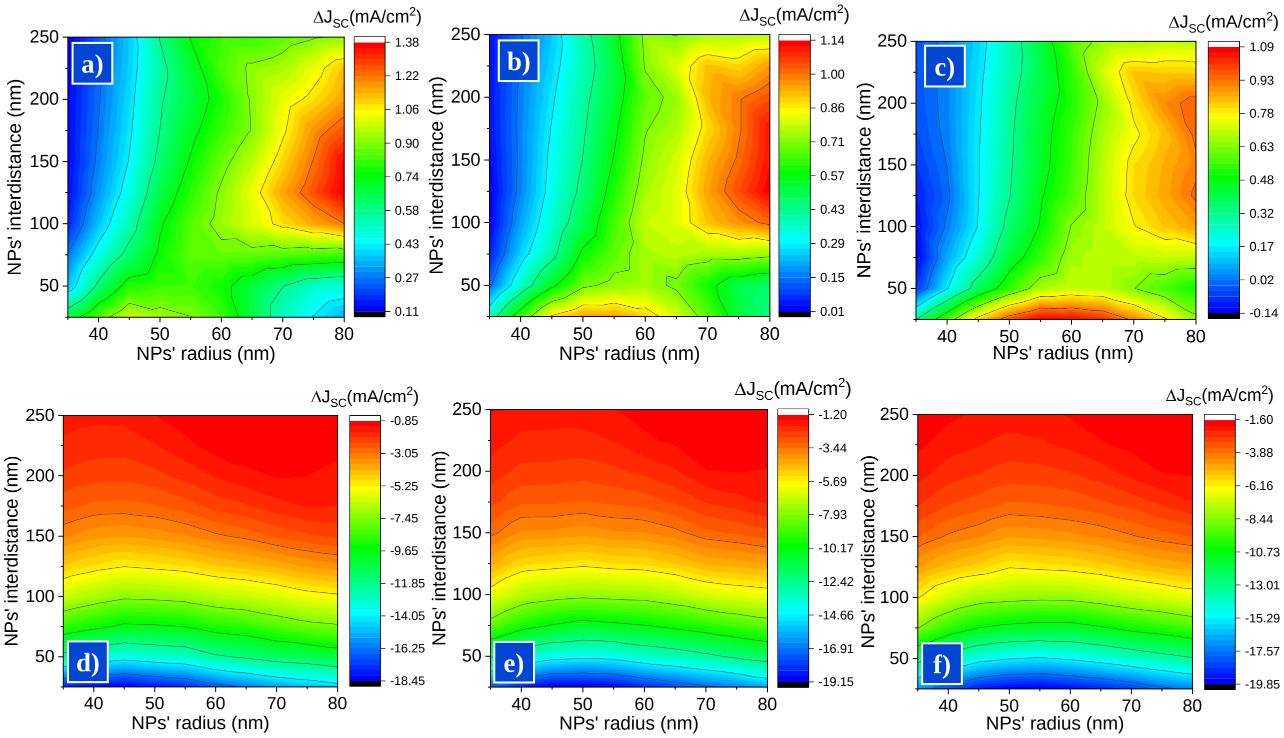

Figure A.1.4- Simulated ΔJ_{SC} colour maps for Au NPs passivated with HfO_2 integrated in an ultrathin CIGS BFSC: for a) 10, b) 15, and c) 20 nm of passivation thickness for FI; for d) 10, e) 15, and f) 20 nm of passivation thickness for RI. Note that the scale is different for each map.

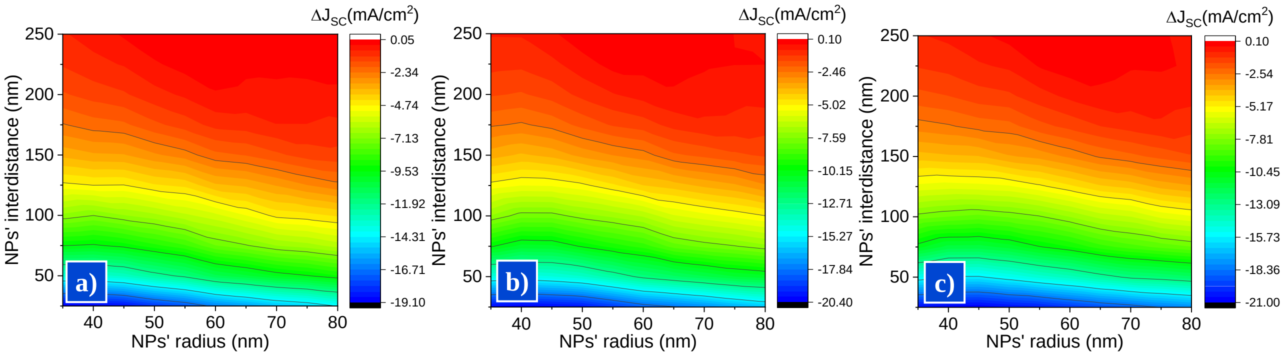

Figure A.1.5- Simulated ΔJ_{SC} colour maps for Au NPs passivated with TiO_2 integrated in an ultrathin CIGS BFSC: for a) 10, b) 15, and c) 20 nm of passivation thickness for RI. Note that the scale is different for each map.

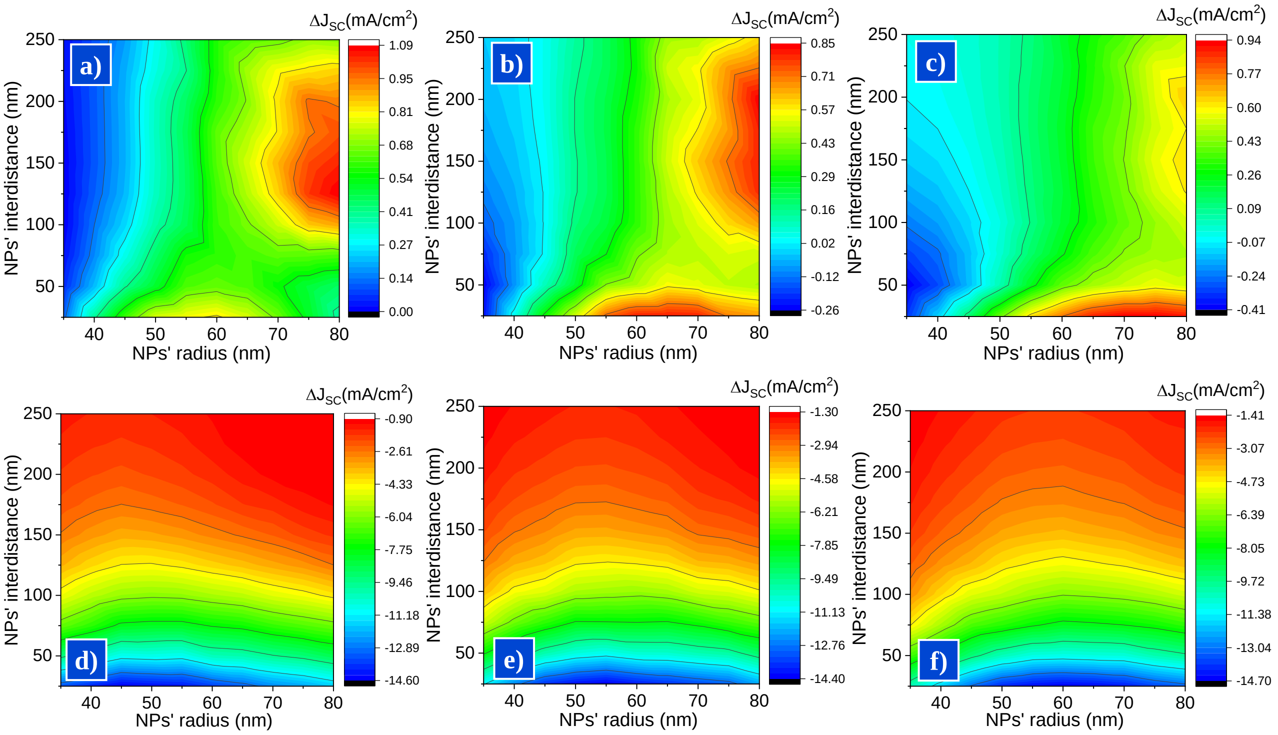

Figure A.1.6- Simulated ΔJ_{SC} colour maps for Ag NPs passivated with SiO_2 integrated in an ultrathin CIGS BFSC: for a) 10, b) 15, and c) 20 nm of passivation thickness for FI; for d) 10, e) 15, and f) 20 nm of passivation thickness for RI. Note that the scale is different for each map.

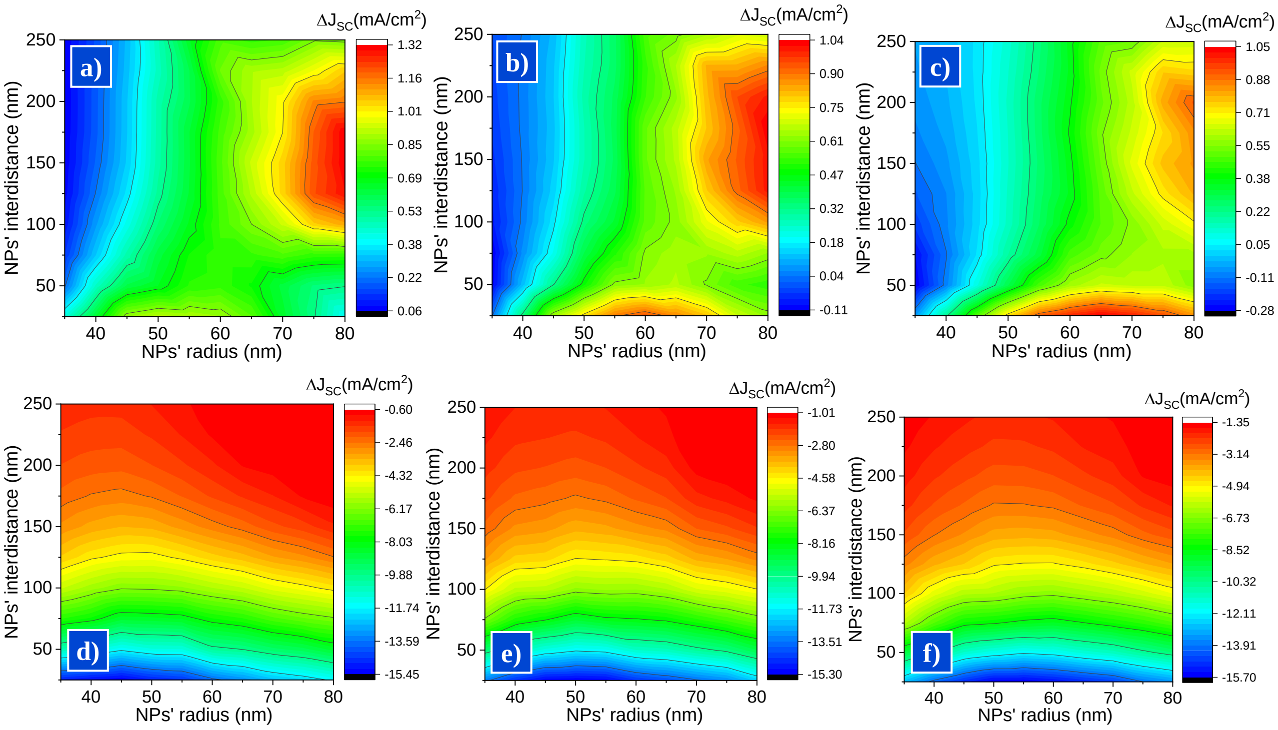

Figure A.1.7- Simulated ΔJ_{SC} colour maps for Ag NPs passivated with Al_2O_3 integrated in an ultrathin CIGS BFSC: for a) 10, b) 15, and c) 20 nm of passivation thickness for FI; for d) 10, e) 15, and f) 20 nm of passivation thickness for RI. Note that the scale is different for each map.

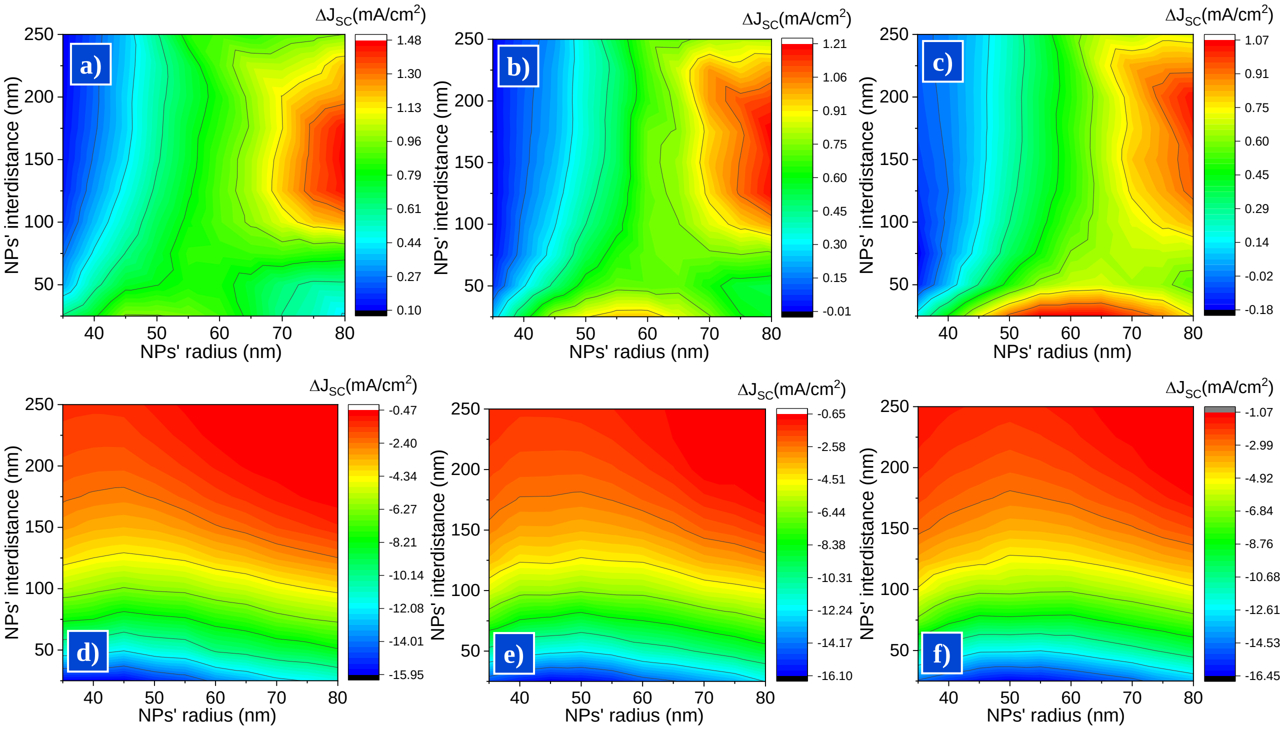

Figure A.1.8- Simulated ΔJ$_{SC}$ colour maps for Ag NPs passivated with HfO$_2$ integrated in an ultrathin CIGS BFSC: for a) 10, b) 15, and c) 20 nm of passivation thickness for FI; for d) 10, e) 15, and f) 20 nm of passivation thickness for RI. Note that the scale is different for each map.

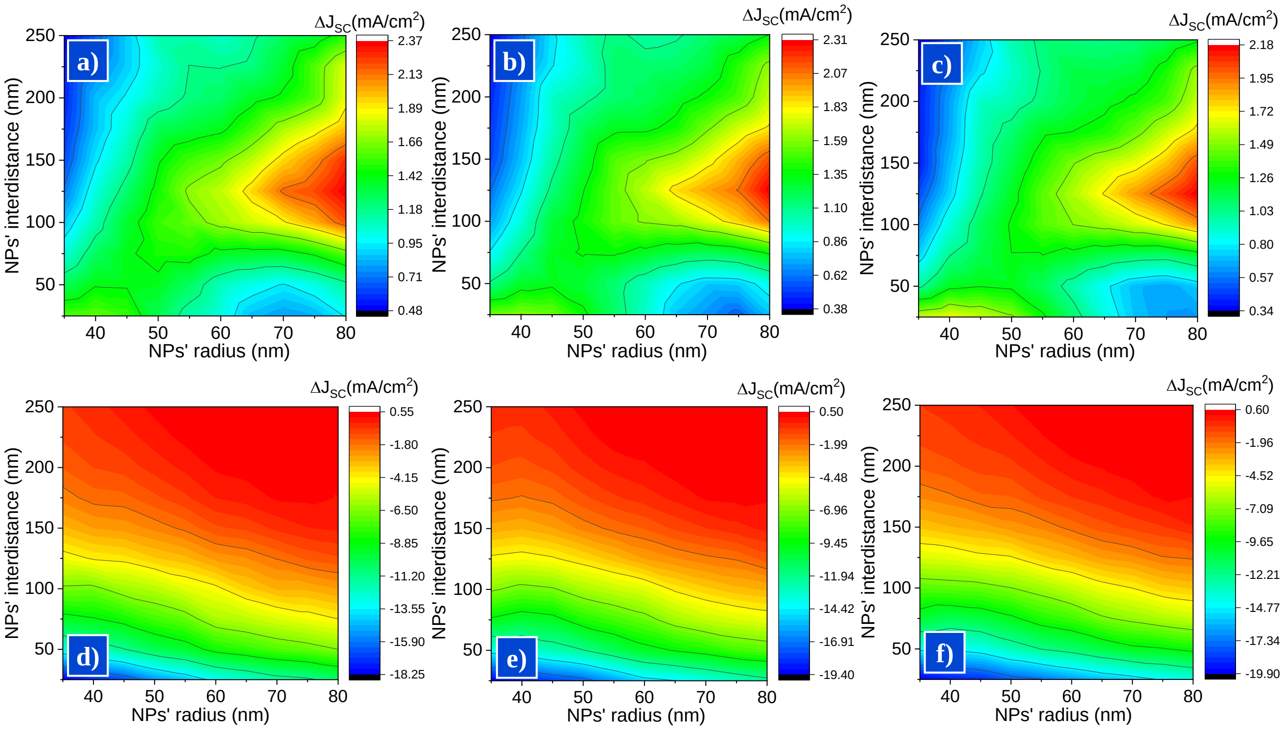

Figure A.1.9- Simulated ΔJ$_{SC}$ colour maps for Ag NPs passivated with TiO$_2$ integrated in an ultrathin CIGS BFSC: for a) 10, b) 15, and c) 20 nm of passivation thickness for FI; for d) 10, e) 15, and f) 20 nm of passivation thickness for RI. Note that the scale is different for each map.

Table A.1.10- Best geometrical parameters for all the studied material combinations, for FI and RI, for 10, 15 and 20 nm of passivation thickness, with the corresponding J_{SC}. The J_{SC} of an ultrathin CIGS solar cell is 26.56 mA/cm^2 for FI, and 24.35 mA/cm^2 for RI.

	Combination (NP/Passivation)	d_{pass} = 10 nm			d_{pass} = 15 nm			d_{pass} = 20 nm		
		Best *r* (nm)	Best *a* (nm)	J_{SC} (mA/cm^2)	Best *r* (nm)	Best *a* (nm)	J_{SC} (mA/cm^2)	Best *r* (nm)	Best *a* (nm)	J_{SC} (mA/cm^2)
FI	Au/SiO_2	80	150	27.60	80	200	27.39	70	25	27.46
	Au/Al_2O_3	80	150	27.79	80	175	27.57	65	25	27.55
	Au/HfO_2	80	125	27.93	80	125	27.70	55	25	27.64
	Au/TiO_2	80	125	28.70	80	125	28.63	80	125	28.51
	Ag/SiO_2	80	125	27.65	80	200	27.41	70	25	27.49
	Ag/Al_2O_3	80	175	27.88	80	175	27.60	65	25	27.60
	Ag/HfO_2	80	150	28.03	80	175	27.77	60	25	27.62
	Ag/TiO_2	80	125	28.92	80	125	28.87	80	125	28.74
RI	Au/SiO_2	65	250	23.11	35	250	22.90	35	250	22.77
	Au/Al_2O_3	65	250	23.33	70	250	22.96	35	250	22.48
	Au/HfO_2	60	250	23.48	70	250	23.16	35	250	22.82
	Au/TiO_2	60	250	24.35	55	250	24.37	55	250	24.35
	Ag/SiO_2	80	225	23.45	35	250	23.10	35	250	23.02
	Ag/Al_2O_3	75	200	23.73	70	250	23.38	75	250	23.03
	Ag/HfO_2	75	225	23.86	70	225	23.69	80	225	23.30
	Ag/TiO_2	80	225	24.79	65	250	24.75	60	250	24.81

Table A.1.11- Best overall geometrical parameters for all the studied material combinations, for 10, 15, and 20 nm of passivation thickness, with the corresponding ΔJ_{SC}.

	Combination (NP/Passivation)	d_{pass} = 10 nm			d_{pass} = 15 nm			d_{pass} = 20 nm		
		Best *r* (nm)	Best *a* (nm)	$\Delta J_{SC,Overall}$ (mA/cm^2)	Best *r* (nm)	Best *a* (nm)	$\Delta J_{SC,Overall}$ (mA/cm^2)	Best *r* (nm)	Best *a* (nm)	$\Delta J_{SC,Overall}$ (mA/cm^2)
FI + RI	Au/SiO_2	10	7	0.776	10	8	0.518	10	8	0.269
	Au/Al_2O_3	10	7	0.955	10	8	0.730	10	8	0.565
	Au/HfO_2	10	7	1.026	10	7	0.829	10	8	0.665
	Au/TiO_2	10	6	1.873	10	6	1.728	10	6	1.611
	Ag/SiO_2	9	8	0.815	10	8	0.629	10	8	0.328
	Ag/Al_2O_3	10	7	1.217	10	7	0.850	10	8	0.691
	Ag/HfO_2	10	7	1.366	10	7	1.075	10	8	0.877
	Ag/TiO_2	10	6	2.244	10	6	2.113	10	6	1.978

The validation of the simulations model for the resonance study could not be done with 9 NPs because of memory limitations. Furthermore, a singular NP was used for the validation, and the smaller mesh size that could be used without exceeding the memory limitations was 0.4 nm. The simulated Mie scattering and absorption efficiency spectra obtained for this setup, in a medium with *n*= 1, are presented in Figure A.1.12- a) and b), respectively, with the corresponding spectrum from the Mie theory. It can be observed that the simulated spectra practically overlap with the spectra from the Mie theory, validating this simulations' setup. However, a 0.4 nm mesh size could not be used in the setup with 9 NPs used for the resonance study without exceeding the memory limits, so it had to be increased to 1.5 nm. The Mie scattering and absorption efficiency spectra obtained for a single NP, with a mesh size of 1.5 nm, in a medium with *n*= 1, are presented in Figure A.1.12- c) and d), respectively. It can be observed that the simulated spectra lost accuracy with the increase in the mesh size, as expected, especially in the absorption efficiency spectrum. However, this difference between the simulated and theoretical curves is minimal at the resonance peak wavelength values and should not affect the conclusions taken when comparing the resonance of the different NPs.

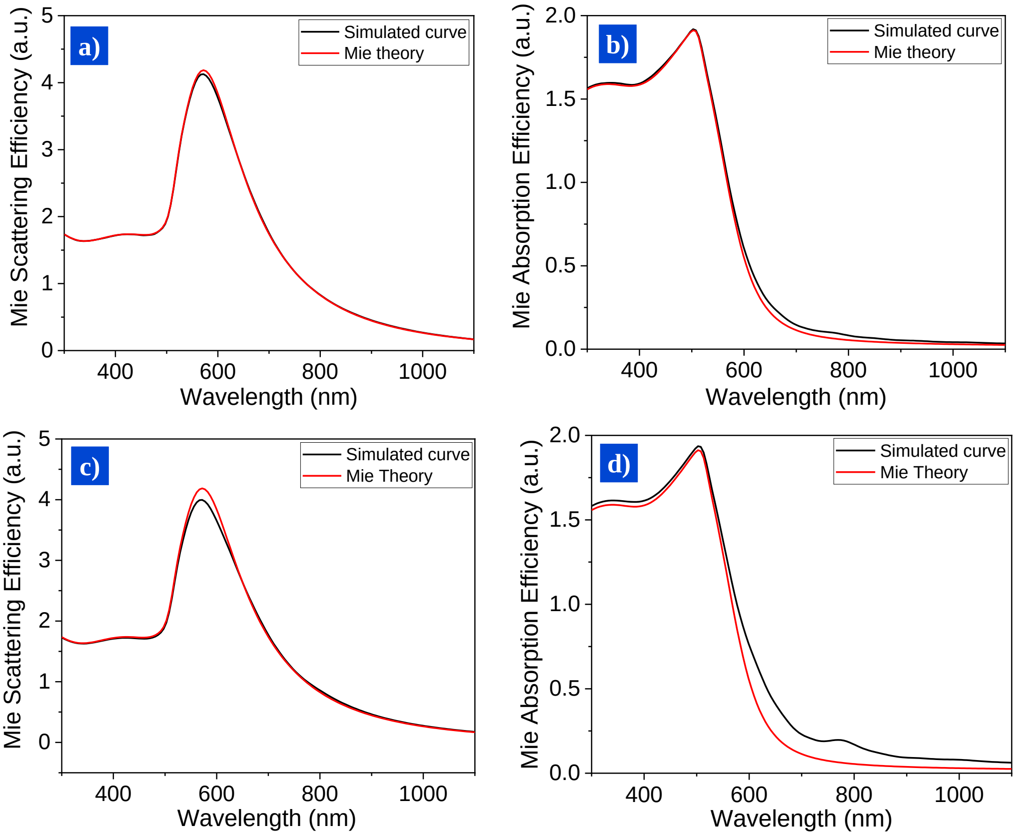

Figure A.1.12- Simulated and theoretical Mie a) scattering and b) absorption efficiency spectra for 1 Au NP with r= 80 nm, in a medium with n= 1, with a mesh size of 0.4 nm. Simulated and theoretical Mie c) scattering and d) absorption efficiency spectra for the same setup, but with a mesh size of 1.5 nm.

A.2 Random Array of NPs

SEM images of Au NPs on ITO, obtained for thermal dewetting at 500 ºC, for t= 2, 4 and 6 h, and for d_{Au}= 2.5, 5, 7.5, 10 and 12.5 nm, are presented here: Figure A.2.1- a), b), and c) correspond to d_{Au}= 2.5 nm, for t= 2, 4, and 6 h, respectively; Figure A.2.1- d), e), and f) correspond to d_{Au}= 5 nm, for t= 2, 4, and 6 h, respectively; Figure A.2.1- g), h), and i) correspond to d_{Au}= 7.5 nm, for t= 2, 4 and 6 h, respectively; Figure A.2.1- j), k), and l) correspond to d_{Au}= 10 nm, for t= 2, 4 and 6 h, respectively; Figure A.2.1- m), n), and o) correspond to d_{Au}= 12.5 nm, for t= 2, 4 and 6 h, respectively. SEM images of Au NPs on ITO, obtained for thermal dewetting at 350 ºC, for t= 2, 4 and 6 h, and for d_{Au}= 2.5, 5, 7.5, 10 and 12.5 nm, are also presented here: Figure A.2.2- a), b), and c) correspond to d_{Au}= 2.5 nm, for t= 2, 4, and 6 h, respectively; Figure A.2.2- d), e), and f) correspond to d_{Au}= 3 nm, for t= 2, 4, and 6 h, respectively; Figure A.2.2- g), h), and i) correspond to d_{Au}= 4 nm, for t= 2, 4, and 6 h, respectively; Figure A.2.2- j), k), and l) correspond to d_{Au}= 5 nm, for t= 2, 4, and 6 h, respectively; Figure A.2.2- m), n), and o) correspond to d_{Au}= 7.5 nm, for t= 2, 4, and 6 h, respectively. Figure A.2.3 are SEM images of a) bare ITO and ITO with d_{Au}= b) 5 and c) 10 nm. Table A.2.4 presents the analysis of the SEM images of the NPs obtained after thermal dewetting, for 350 and 500 ºC and for t= 2, 4 and 6 h, for the studied d_{Au} values. The calculated surface free energy for the ITO reference sample annealed at 350 and 500 ºC, for t= 2, 4, and 6 h, are displayed in Table A.2.5. Figure A.2.6 are SEM images of ITO after 112 s of a) C_4F_8 and b) Cl_2 plasma etching. Figure A.2.7 are SEM images of the NPs obtained after thermal dewetting of a 4 nm Au film, at 500 ºC for 2 h, for: a) ITO in N_2 atmosphere; b) ITO etched with 112 s of C_4F_8 plasma in N_2 atmosphere; c) ITO in air.

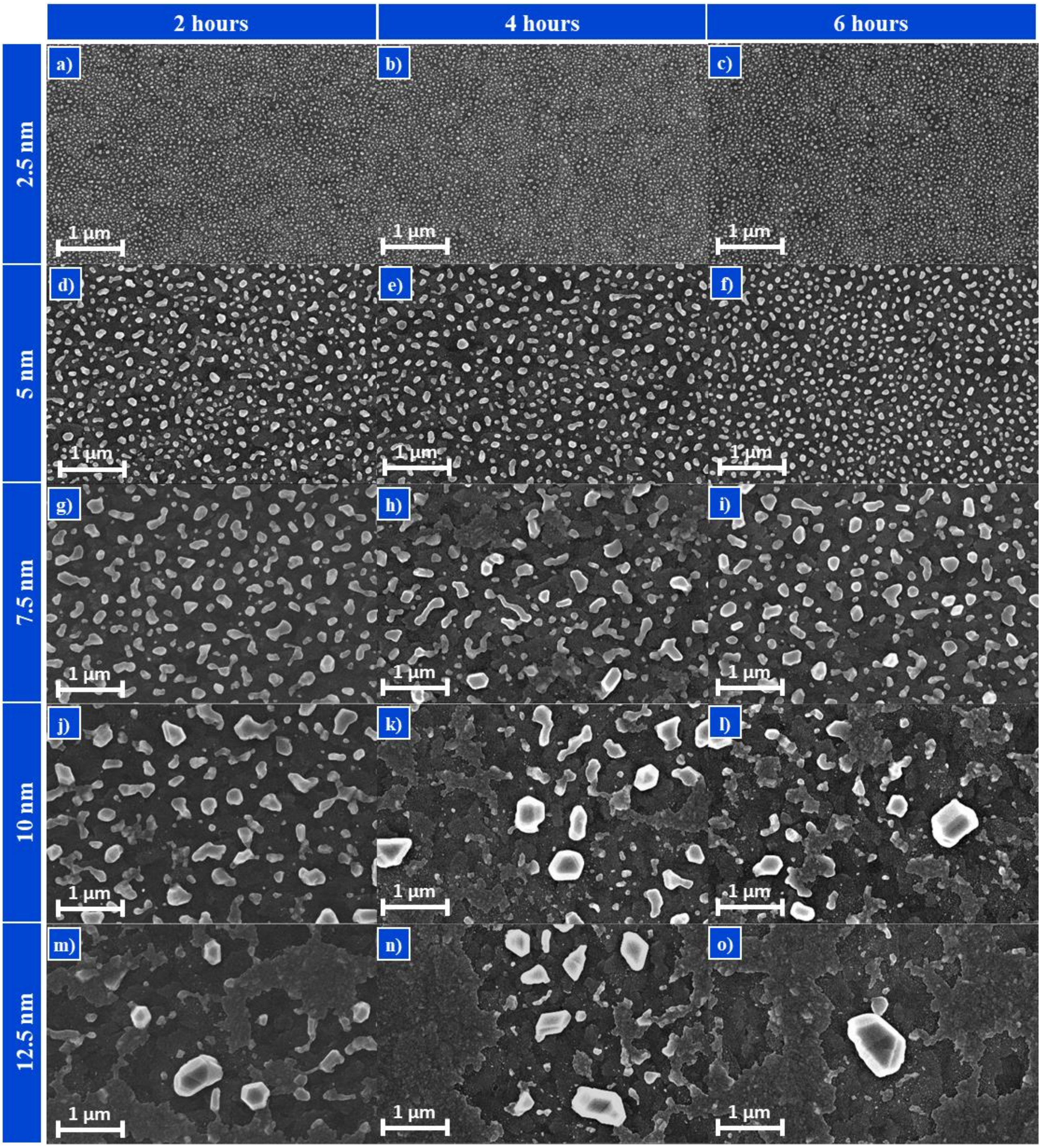

Figure A.2.1- SEM images of Au NPs on ITO, obtained after thermal dewetting at 500 ºC: for d_{Au}= 2.5 nm, for t= a) 2, b) 4 and c) 6 h; for d_{Au}= 5 nm, for t= d) 2, e) 4, and f) 6 h; for d_{Au}= 7.5 nm, for t= g) 2, h) 4, and i) 6 h; for d_{Au}= 10 nm, for t= j) 2, k) 4, and l) 6 h; for d_{Au}= 12.5 nm, for t= m) 2, n) 4, and o) 6 h.

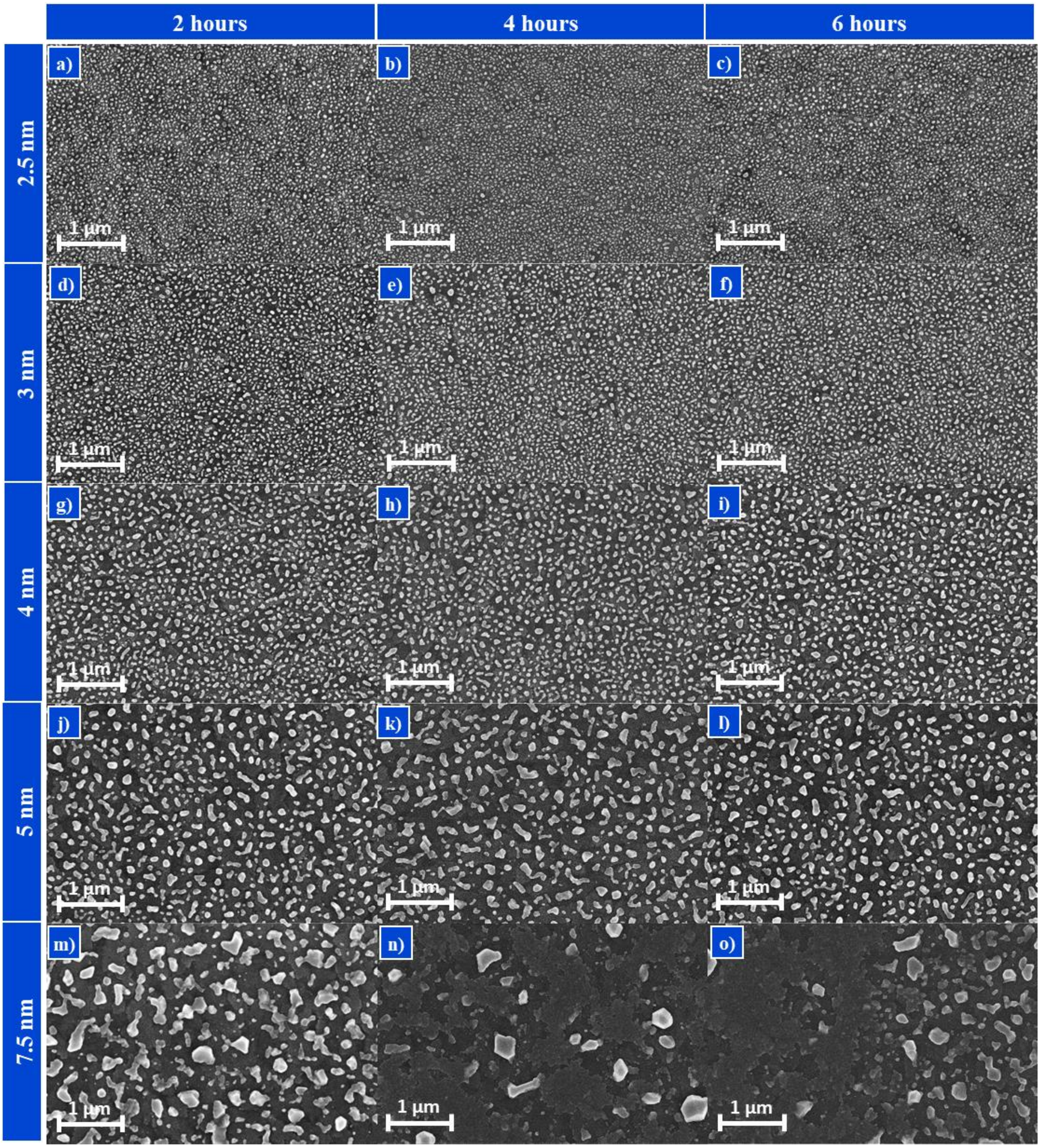

Figure A.2.2- SEM images of Au NPs on ITO, obtained after thermal dewetting at 350 ºC: for d_{Au}= 2.5 nm, for t= a) 2, b) 4 and c) 6 h.; for d_{Au}= 3 nm, for t= d) 2, e) 4, and f) 6 h; for d_{Au}= 4 nm, for t= g) 2, h) 4, and i) 6 h; for d_{Au}= 5 nm, for t= j) 2, k) 4, and l) 6 h; for d_{Au}= 7.5 nm, for t= m) 2, n) 4, and o) 6 h.

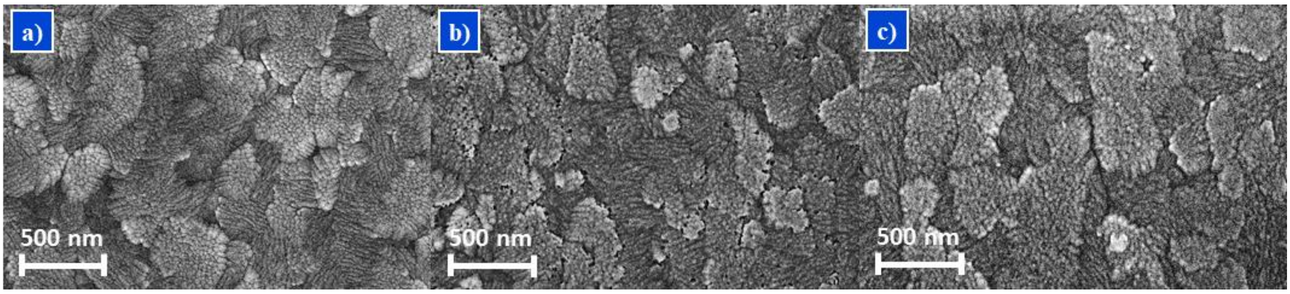

Figure A.2.3- SEM images of a) bare ITO, and ITO with d_{Au}= b) 5 and c) 10 nm.

Table A.2.4- Results from the analysis of the SEM images of the NPs obtained after thermal dewetting, for 350 and 500 ºC and for t= 2, 4 and 6 h, for different d_{Au} values. ImageJ software was used to analyse the NPs.

T (°C)	t (h)	d_{Au} (nm)	NPs' r (nm)		Circularity		NP's a (nm)	Surface Coverage (%)
			Average	Std. Dev.	Average	Std. Dev.	Average	Average
500	2	2.5	17	4	0.72	0.13	27	25.1
		5	41	19	0.72	0.18	65	24.6
		7.5	66	39	0.77	0.20	110	23.4
	4	2.5	17	4	0.75	0.11	26	24.8
		5	43	17	0.77	0.13	78	21.7
		7.5	58	44	0.60	0.22	109	21.0
	6	2.5	16	4	0.70	0.11	27	23.2
		5	39	15	0.81	0.12	66	23.1
		7.5	54	41	0.72	0.17	95	22.1
350	2	2.5	18	5	0.55	0.13	26	27.0
		3	21	6	0.69	0.14	32	26.0
		4	29	11	0.67	0.15	45	25.4
		5	44	20	0.68	0.16	67	25.6
	4	2.5	18	5	0.71	0.13	24	28.6
		3	23	7	0.70	0.13	32	27.3
		4	32	12	0.75	0.17	50	25.0
		5	51	26	0.67	0.21	79	24.9
	6	2.5	18	5	0.52	0.13	24	28.5
		3	23	7	0.72	0.13	33	26.9
		4	32	13	0.76	0.17	51	24.6
		5	44	20	0.72	0.18	71	24.1

Table A.2.5- Calculated surface free energy for bare ITO samples annealed at 350 and 500 ºC, for 2, 4, and 6 h.

	Surface Free Energy (mJ/m^2)			
Annealing Temperature (°C)/ Time (h)	2	4	6	Reference
350	74.3	74.4	75.2	74.7
500	74.6	74.5	74.9	

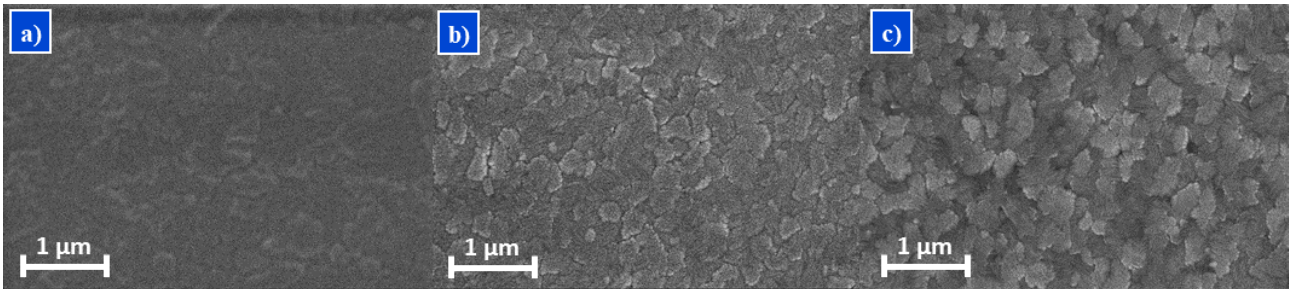

Figure A.2.6- SEM images of ITO after 112 s of a) C_4F_8 and b) Cl_2 plasma etching. C) SEM image of bare ITO.

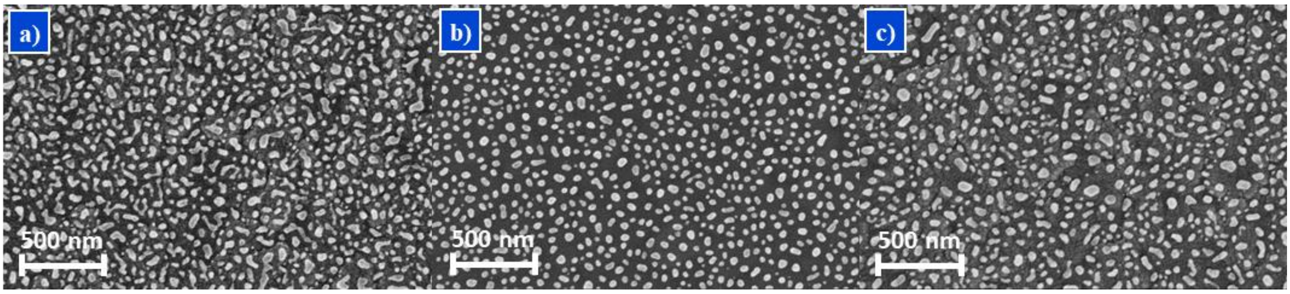

Figure A.2.7- SEM images of the NPs obtained after thermal dewetting of a 4 nm Au film, at 500 ºC for 2 hours, for: a) ITO in N_2 atmosphere; b) ITO etched with 112 s of C_4F_8 plasma in N_2 atmosphere; ITO in air.

A.3 Periodic Array of NPs

The fabrication procedure of both master stamps is the same, and it starts by cleaning a Si substrate with a standard procedure acetone, IPA and deionized water, defined above. Then, a 150 nm SiO_2 layer was deposited by PECVD (30 W, 13.56 MHz plasma with 1420 sccm N_2O, 10 sccm SiH_4, and 392 sccm N_2 flow, performed at 200 ºC on a SPTS MPX CVD system) and primed with HMDS at 150 ºC for 300 s in the Vapour Prime YES-310TA oven. Then, it was coated with 200 nm of ARN 7250.18 diluted in AR 300-12, in 1:1 weight ratio, at 2750 rpm, and baked at 85 °C for 60 s. Electron Beam Lithography was then performed on the resist, using the Vistec EBPG 5200 system, with a dose of 11565 $\mu C/cm^2$, to create a square array of holes with the desired geometrical dimensions. The exposed resist was then baked at 85 ºC for 120 s, followed by development with TMAH for 60 s, revealing the pattern. The exposed SiO_2 was lastly etched with RIE (2000 W, 13.56 MHz plasma with 50 sccm C_4F_8 and 30 sccm H_2 flow, performed at 0 ºC 5 mTorr in a SPTS APS system) for 30 s. The remaining resist was stripped with an O_2 plasma ashing (500 W 2.45 GHz plasma with 600 sccm O_2 and 50 sccm Ar flow, performed on the PVA Tepla Gigabatch 360M system), obtaining the patterned SiO_2, that will serve as the master stamp.

In the initial Au deposition tests by evaporation, the NDs were non-homogenous, broken in a preferencial direction, and had a hole in the middle. To test if the deposition setup was what was causing these/// deposition problems, three samples were prepared using the same methods till the development, and they were placed in three different deposition setups: sample A was placed in the centre of the stage and sample B was placed on the edge of the stage, both with the stage rotating during deposition; sample C was placed as much as possible underneath the resistive boat, and the stage was not rotating during deposition. By varying the placement of the sample during deposition, it was tested if it influences how the Au is being deposited underneath the TU7, and by placing a sample right below the source, it was tested if the angle of deposition was causing the hole in the middle of the NDs. SEM images of samples A, B and C are presented in Figure A.3.1-a), b) and c), respectively. Sample A appears to have a high density of discs, but it only had discs near the borders, with the centre being depleted. However, these discs appear to not have their edges bent or to be broken. Most NDs from sample B were broken in half, indicating that only part of the discs was being deposited on top of the LOR. In addition, the density of NDs was inconsistent throughout the sample, meaning that in some zones, instead of the NDs being broken in half, they were just completely removed. Besides this, there is a clear side preference for deposition, which is the side where more Au was being deposited on top of the LOR and it was broken off. Sample C had practically no NDs, with some random large patches of resist and Au that were not removed during the lift-off, most probably because the Au was completely filling the hole and the developer could not get in. All the samples still had the hole in the middle, so this is also a deposition problem that cannot be avoided just by changing the setup.

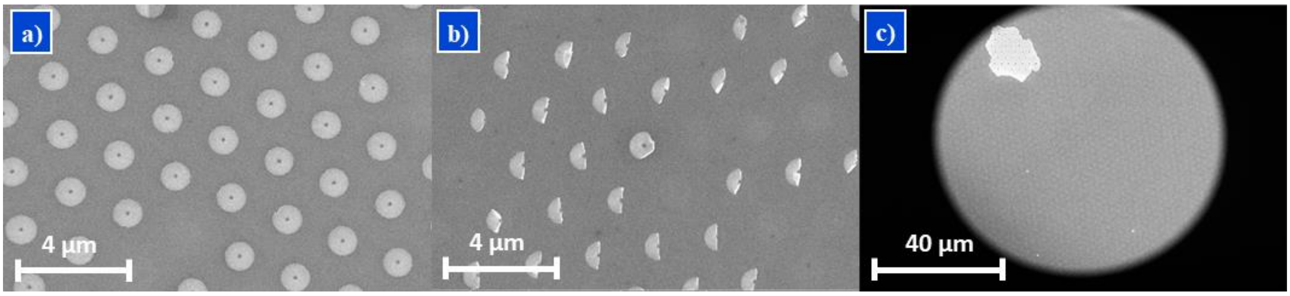

Figure A.3.1- SEM images of samples after lift-off, for 100 nm of deposited Au by evaporation, with three different setups: a) sample in the centre with stage rotating; b) sample near the edge with the stage rotating; c) sample below the source without stage rotation.

Figure A.3.2- a) and b) are top-view SEM images of 100 nm of evaporated and sputtered Au respectively, for the larger pattern with d= 400 nm and p=2000 nm, LOR1A with 170 nm thickness as the lift-off resist, and TMAH 2.2% as the developer. Figure A.3.3- a), b), c), d), e), f) and g) are SEM images of Au NDs, obtained after lift-off, for 10, 15, 20, 25, 50, 75 and 100 nm of sputtered Au, respectively, for the same setup. Figure A.3.4- a), b), c), d), e), f) and g) are SEM images of Au NPs, obtained after thermal dewetting at 800 ºC for 2 h, for 10, 15, 20, 25, 50, 75 and 100 nm of sputtered Au, respectively, for the same setup, and Figure A.3.5 corresponds to the correlation between the thickness of the deposited Au with the NPs' radius. Figure A.3.6- a), b, c), d), e), and f), are SEM images of the Au NPs obtained after thermal dewetting at 800 ºC for 2 h, for a sputtered Au thickness of 40, 50, 60, 70, 80, and 90 nm, respectively, for the smaller pattern with d= 100 nm and p=600 nm, LOR1A with 170 nm thickness as the lift-off resist, and TMAH 1.5 % as the developer.

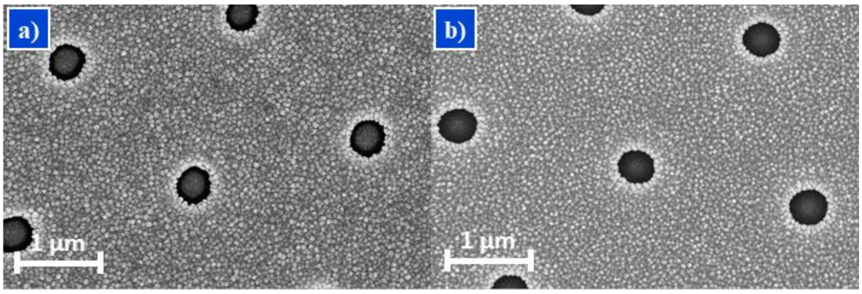

Figure A.3.2- Top view SEM images of samples after deposition of 100 nm of Au by a) evaporation and by b) sputtering, for the pattern with d= 400 nm and p=2000 nm.

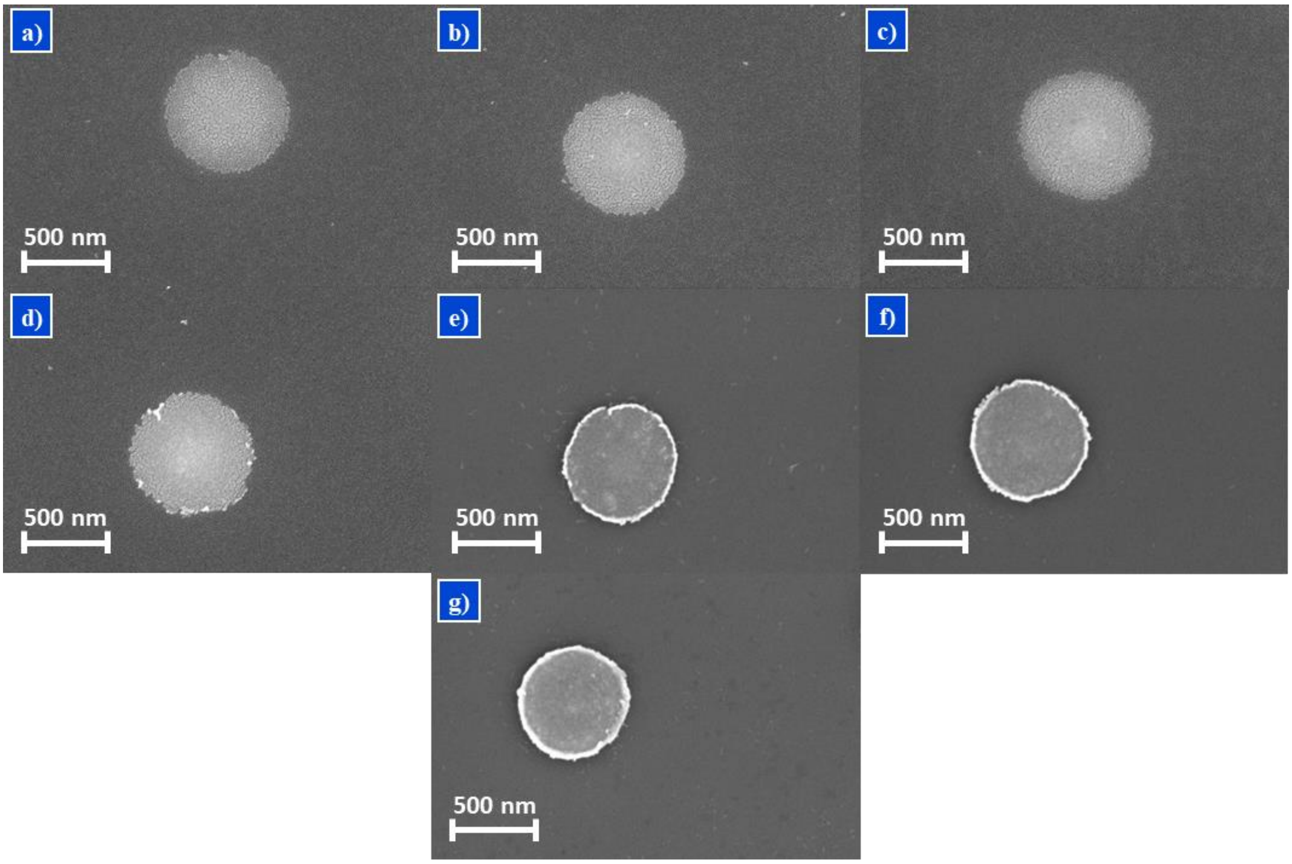

Figure A.3.3- SEM images of the Au NDs, obtained after lift-off, for a) 10, b) 15, c) 20, d) 25, e) 50, f) 75 and g) 100 nm of sputtered Au, for the pattern with d= 400 nm and p=2000 nm.

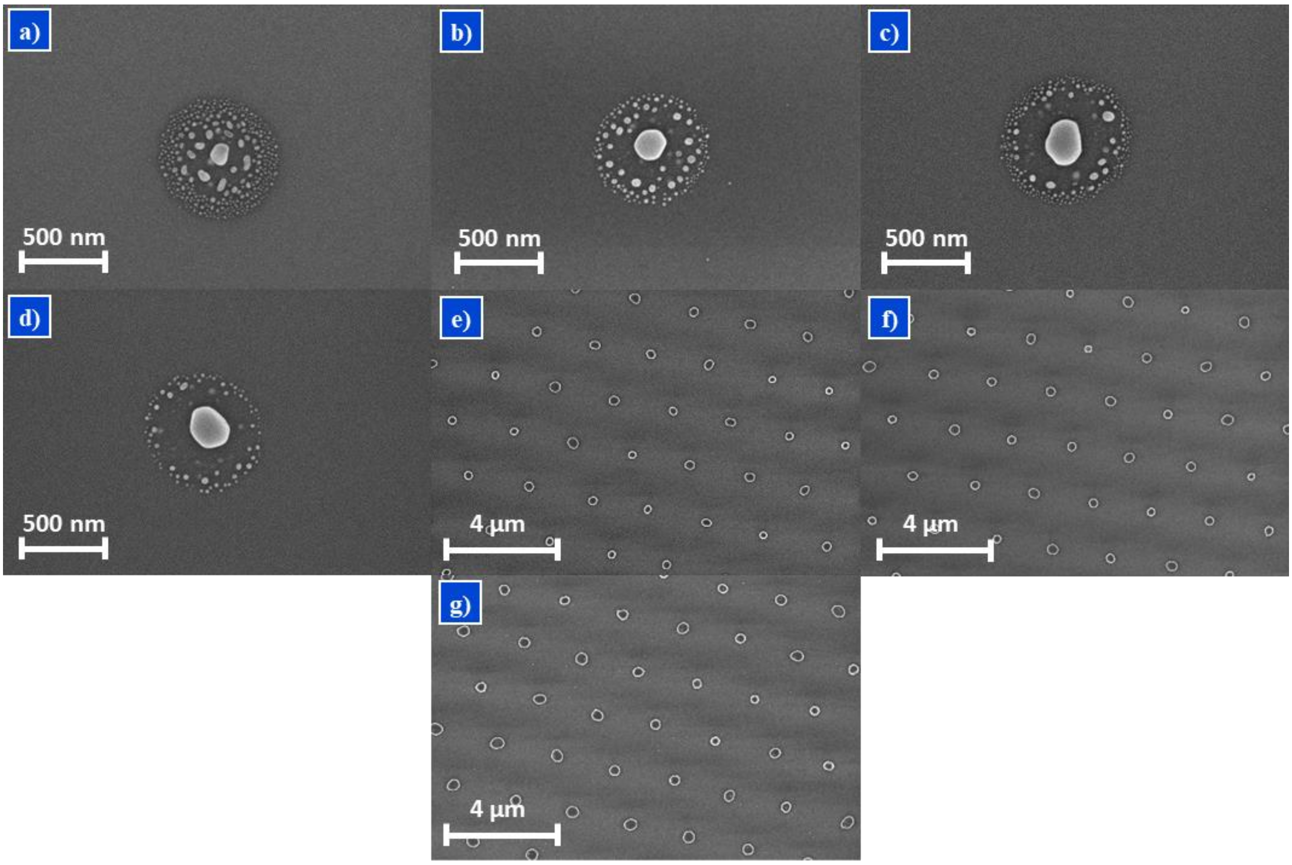

Figure A.3.4- SEM images of the Au NDs, obtained after thermal dewetting at 800 ºC for 2 h, for a) 10, b) 15, c) 20, d) 25, e) 50, f) 75 and g) 100 nm of sputtered Au, for the pattern with d= 400 nm and p=2000 nm.

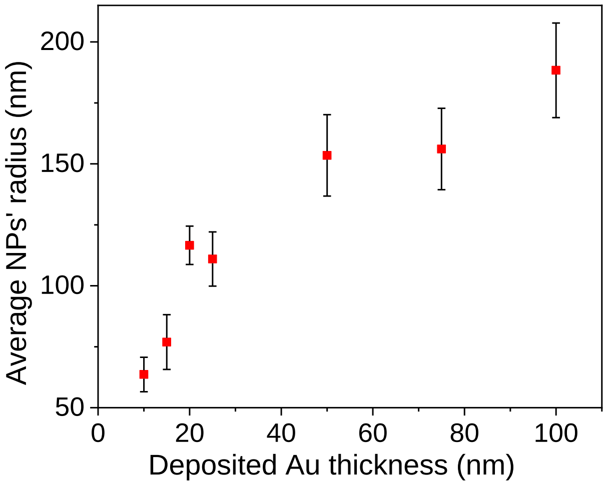

Figure A.3.5- Correlation between initial Au film thickness and final NPs' average *r*, for the pattern with d= 400 nm and p=2000 nm.

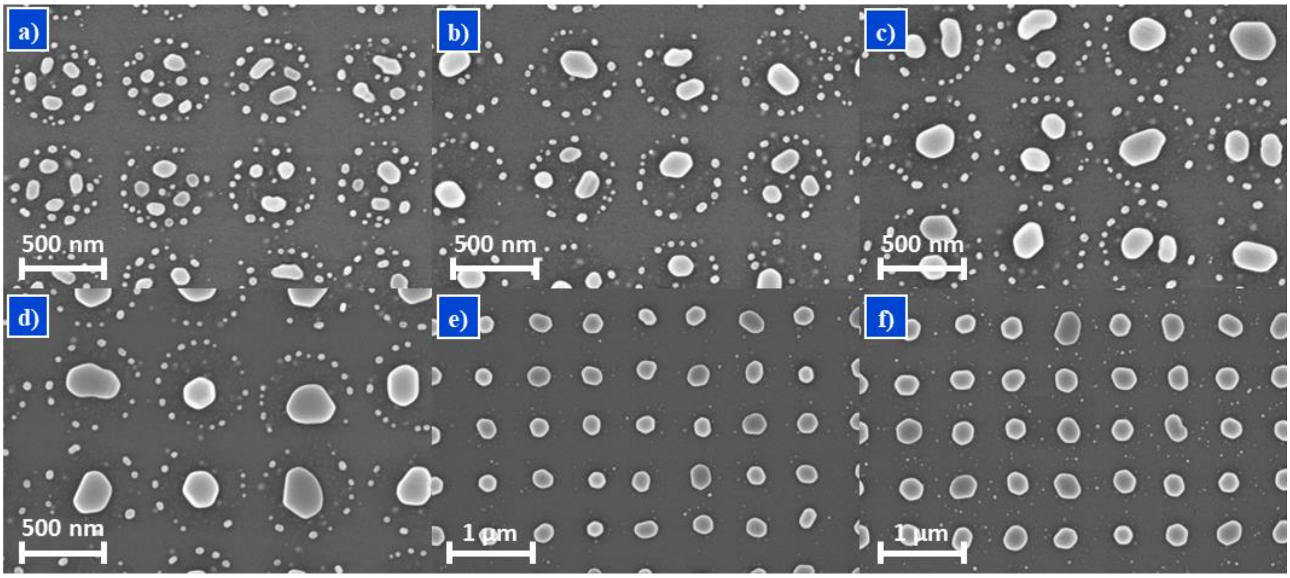

Figure A.3.6- SEM images of the Au NPs obtained after thermal dewetting at 800 ºC for 2 h, for a sputtered Au thickness of a) 40, b) 50, c) 60, d) 70, e) 80, and f) 90 nm, for the pattern with d= 100 nm and p=600 nm

A.4 Dissemination

Poster Presentations at Conferences and Workshops

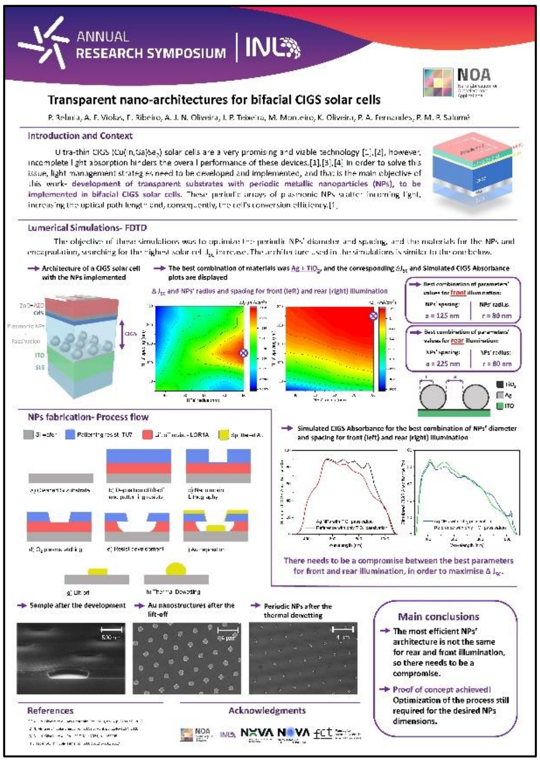

Transparent nano-architectures for bifacial CIGS solar cells

P. Rebola, A. F. Violas, E. Ribeiro, A. J. N. Oliveira, J. P. Teixeira, M. Monteiro, K. Oliveira, P. A. Fernandes, P. M. P. Salomé

Introduction and Context

Ultra-thin CIGS (Cu(In,Ga)Se$_2$) solar cells are a very promising and viable technology [1],[2], however, incomplete light absorption hinders the overall performance of these devices.[1],[3],[4] In order to solve this issue, light management strategies need to be developed and implemented, and that is the main objective of this work- **development of transparent substrates with periodic metallic nanoparticles (NPs), to be implemented in bifacial CIGS solar cells.** These periodic arrays of plasmonic NPs scatter incoming light, increasing the optical path length and, consequently, the cell's conversion efficiency.[1]

Lumerical Simulations- FDTD

The objective of these simulations was to optimize the periodic NPs' diameter and spacing, and the materials for the NPs and encapsulation, searching for the highest solar cell J_{SC} increase. The architecture used in the simulations is similar to the one below.

- Architecture of a CIGS solar cell with the NPs implemented
- The best combination of materials was Ag + TiO$_2$, and the corresponding ΔJ_{SC} and Simulated CIGS Absorbance plots are displayed

ΔJ_{SC} and NPs' radius and spacing for front (left) and rear (right) illumination

- Best combination of parameters' values for front illumination:

NPs' spacing:	NPs' radius:
a = 125 nm	r = 80 nm

- Best combination of parameters' values for rear illumination:

NPs' spacing:	NPs' radius:
a = 225 nm	r = 80 nm

NPs fabrication- Process flow

- Simulated CIGS Absorbance for the best combination of NPs' diameter and spacing for front (left) and rear (right) illumination

There needs to be a compromise between the best parameters for front and rear illumination, in order to maximise ΔJ_{SC}.

- Sample after the development
- Au nanostructures after the lift-off
- Periodic NPs after the thermal dewetting

Main conclusions

- The most efficient NPs' architecture is not the same for rear and front illumination, so there needs to be a compromise.
- Proof of concept achieved! Optimization of the process still required for the desired NPs dimensions.

References

Acknowledgments

P. Rebola, A. F. Violas, E. Ribeiro, A. J. N. Oliveira, J. P. Teixeira, M. Monteiro, K. Oliveira, P. A. Fernandes, P. M. P. Salomé, "Transparent nano-architectures for bifacial CIGS solar cells", INL Annual Research Symposium, 19-21 de abril 2023.

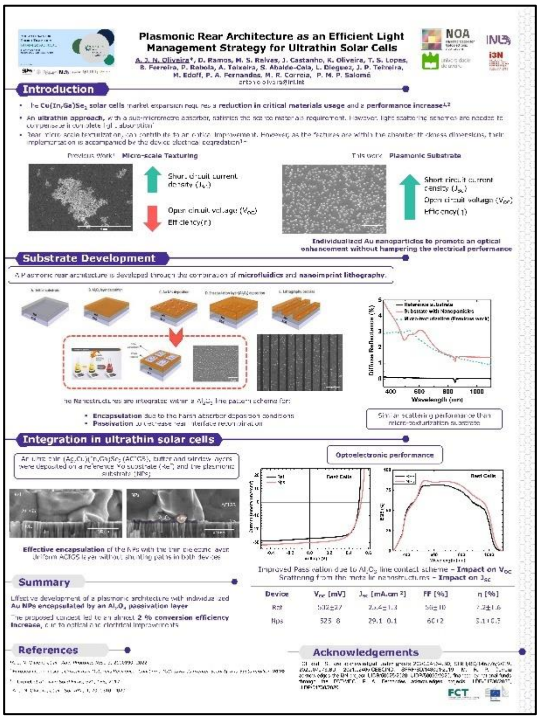

Plasmonic Rear Architecture as an Efficient Light Management Strategy for Ultrathin Solar Cells

A. J. N. Oliveira*, D. Ramos, M. S. Relvas, J. Castanho, K. Oliveira, T. S. Lopes, B. Ferreira, P. Rebola, A. Teixeira, S. Abalde-Cela, L. Dieguez, J. P. Teixeira, M. Edoff, P. A. Fernandes, M. R. Correia, P. M. P. Salomé

Introduction

Substrate Development

Integration in ultrathin solar cells

Optoelectronic performance

Summary

References

Acknowledgements

A. J. N. Oliveira*, D. Ramos, M. S. Relvas, J. Castanho, K. Oliveira, T. S. Lopes, B. Ferreira, **P. Rebola**, A. Teixeira, S. Abalde-Cela, L. Dieguez, J. P. Teixeira, M. Edoff, P. A. Fernandes, M. R. Correia, P. M. P. Salomé, “Plasmonic Rear Architecture as an Efficient Light Management Strategy for Ultrathin Solar Cells”, 2nd Materials for Energy Transition Summer School, 6-8 setembro 2023, Ordem dos Engenheiros, Porto.

Oral Presentations at Conferences and Workshops

A. J. N. Oliveira, J. P. Teixeira, A. Violas, E. J. Ribeiro, **P. Rebola**, B. Du, W. N. Shafarman, P. A. Fernandes, M. R. P. Correia, P. M. P. Salomé, “Light Management and Passivation Strategies in Chalcogenide Thin Film Technologies”, Research Summit, Universidade de Aveiro, 12-14 de julho 2023.

A. F. Violas, E. J. Ribeiro, **P. Rebola**, A. J. N. Oliveira, J. P. Teixeira, P. A. Fernandes, P. M. P. Salomé, “High Performance Transparent Substrates to Disrupt Thin Film Photovoltaics”, Research Summit, Universidade de Aveiro, 12-14 de julho 2023.

A. F. Violas, E. J. Ribeiro, **P. Rebola**, A. J. N. Oliveira, R. F. Alexandre, J. P. Teixeira, P. A. Fernandes, P. M. P. Salomé, “The Impact of High-Performance Transparent Substrates on Bifacial Solar Cells Performance”, INL Workshop Vácuo, 2023.

2023

Pedro Miguel Vilela
Pereira Valentim Rebola

OPTIMIZATION OF A SCATTERING METALLIC NANOPARTICLES ARRAY TO BE IMPLEMENTED IN ULTRATHIN CIGS BIFACIAL SOLAR CELLS

NOVA SCHOOL OF
SCIENCE & TECHNOLOGY